Plasma-surface interactions in all-metal-wall tokamaks

<small>INAUGURALDISSERTATION</small>

zur

Erlangung der Würde eines Doktors der Philosophie

vorgelegt der

Philosophisch-Naturwissenschaftlichen Fakultät

der Universität Basel

von

Marwa Ben Yaala

aus Tunesien

Basel, 2021

Genehmigt von der Philosophisch-Naturwissenschaftlichen Fakultät
auf Antrag von:

Dr. Laurent Marot
Prof. Dr. Thomas Jung
Prof. Dr. Ernst Meyer

Basel, 25. June 2019

Prof. Dr. Martin Spiess, Dekan

"I am among those who think that science has great beauty. A scientist in his laboratory is not only a technician: he is also a child placed before natural phenomenon which impresses him like a fairy tale. "

Marie Curie

To my daughter Mira whose beautiful smile gave me the strength to move forward.

Contents

Contents

Introduction and thesis outline

I‍T has been well known for many years that the standard of living is directly proportional to energy consumption i.e. a good quality of life requires substantial energy supply. Consequently, the worldwide demand for energy is growing very fast and it is expected that the energy consumption will at the very least be double of the present world consumption by the year 2100. In particular, the global demand for electricity is expected to increase up to 45 % by 2040 due to the expected growth of the world's population from 7.7 to 9 billion. Currently, most of the world's energy including electricity is derived from fossil fuels which are exhaustible finite sources and produce greenhouse gases with a negative impact on the environment. The imperative need for a safe, carbon-free and abundant energy source is growing stronger during the last decade. One promising candidate, which has been researched since the early 1950s, is fusion energy.

Unlike nuclear fission that involves the splitting of heavy nuclei, fusion is a form of nuclear energy that involves the merging (i.e., the fusing) of light elements like hydrogen isotopes deuterium (D) and tritium (T). Fusion has a significant advantage compared to fission that it cannot undergo a runaway energy release. In fact, the fuels are constantly fed into the reactor in quantities enough to keep the reaction going for just a few seconds. A second safety consideration is the radioactive waste. The fusion fuel cycle itself produces no radioactive waste products. The waste product is helium gas, which is neither toxic nor radioactive. The walls of the plasma vessel get activated upon the impact of high energetic neutrons from the fusion reaction. The most radioactive parts will need to be protected for less than 100 years before they can be recycled or reused. The raw materials necessary for the fusion fuel, lithium and water, are completely non-radioactive. The produced tritium fuel itself is radioactive, but it decays relatively quickly (the half-life is 12.3 years) and it will be recycled quickly and burned in the power plant.

Another advantage of fusion is related to the fuels which are cheap, abundant and uniformly distributed on earth. Seawater contains deuterium in practically inexhaustible quantities and tritium will be produced in the fusion power plant from lithium, which

is likewise abundantly available. Last but not least, fusion is a very attractive energy source with respect to its environmental impact. Fusion reactions produce no CO_2, no greenhouse gases and no other harmful chemicals into the atmosphere. The two by-products of the fusion reactions are an inert non-polluting helium gas and neutrons entirely captured in the fusion blanket.

The conclusion from these advantages is that fusion energy is a very attractive new energy source from the point of view of fuel reserves, environmental impact, and safety. However several technical and scientific challenges still exist.

One of these challenges concerns a particular component in the fusion reactor; the divertor, which withstands the highest heat load. Seeding nitrogen is considered as a solution in tokamaks to help dissipating the heat and reduce the power load onto the divertor target plates. However, nitrogen molecules are chemically reactive with hydrogen and its isotopes to form stable tritiated ammonia. The last studies and observations show that with a 5% conversion into ammonia, 0.2 g of associated tritium could be trapped per pulse in the future ITER D-T operation [1, 2]. The formation of large quantities of tritiated NH_3 has consequences for several aspects of the ITER operation and maintenance. In particular, cryopump would need more frequent regeneration that would limit ITER operational cycle. Since NH_3 is a polar molecule, it can be easily adsorbed on metallic surfaces [3, 4] and in particular on ITER first-wall material beryllium (Be), divertor material tungsten (W) and on the vacuum vessel and pipework made of stainless steel (SS). The in-vessel T inventory in ITER is limited to 1 kg [5] for safety reasons and the formation and sticking of large quantities of tritiated ammonia could contribute to the overall inventory while the recovery of T from ND_2T is still an open issue.

Having said that, this thesis seeks to develop a fundamental understanding of the ammonia formation process, to explore possible ways to decrease it and to investigate the formed ammonia interaction with materials inside the tokamak. This study will, therefore, address the following questions:

1- Where and how does the ammonia formation occur i.e: in the plasma and/or on the surface and how does it depend on the surface material?

2- What is the impact of specific parameters from the fusion reactor environment, in particular temperature and presence of other gases, on the ammonia formation and is there possible ways to decrease the formed quantity?

3- How much of the ammonia produced quantity can stick on fusion device relevant materials (tungsten, stainless steel, beryllium and boron) and is ammonia adsorbed as a molecule or does it undergo dissociative adsorption?

According to these objectives, the three chapters following the theory chapter 1 dealing with the basics of nuclear fusion will be the following:

Chapter 2 begins by laying out the theoretical dimensions of plasma-assisted catalysis and dominant reactions pathways for ammonia synthesis. The experimental part includes a detailed description of a newly built setup and the experimental procedure developed for the ammonia production study. The effect of the presence of tungsten and stainless steel surfaces on ammonia production for different nitrogen-hydrogen plasma composition will then be presented. The last part of this chapter gives fundamental information about the nature of the reactive processes occurring during RF

plasma-assisted ammonia synthesis will be presented based on RGA results and surface chemistry analysis carried out using X-ray photoelectron spectroscopy (XPS).

Chapter 3 is concerned with the effect of two parameters on the ammonia production from nitrogen-hydrogen plasma including the sample surface temperature and He or Ar addition. The results will be shown for temperature values ranging from room temperature (RT) to 1270 K, a value that the ITER tungsten divertor can reach in the active areas where the plasma impact occurs. On the other hand, the main drive of the noble gas admixture effect is to determine a process that reduces the ammonia production in the nuclear device without modifying the positive effects of nitrogen seeding on plasma performance. While He will be present as an intrinsic plasma impurity in ITER, Ar gas was identified as the best candidate for the simultaneous enhancement of core and divertor radiation in the case where elevated main chamber radiation is desired as well.

In the chapter 4, ammonia sticking on different fusion-relevant materials will be presented. In particular, the interaction of NH_3 molecules with W, SS and Be surfaces using QMB and XPS techniques will be shown. In addition to these materials used for the tokamak components, boron and gold surfaces will also be investigated as well. The former element is largely used in tokamaks to decrease the oxygen (O) content (by boronization) while the latter can be used as a reference for the QMB technique. NH_3 adsorption/desorption study will be presented by examining the effect of both pressure and surface material on sticking along with an XPS study to analyze the residual NH_3 molecules sticking on the surface.

The last two chapters of this dissertation include further material related topics for the fusion research namely metallic first mirror plasma cleaning and tokamak wall reflection measurements and simulation.

The reliability of optical diagnostic systems is a key element for successful ITER operations. Particular attention has to be given to first mirrors, involved in almost 40 diagnostics, and whose reflectivity might change due to erosion and deposition from the first wall. Mirror surface recovery techniques will be required and in situ plasma cleaning is considered as the most promising solution. Chapter 5 presents the findings on the removal of relevant ITER contaminants namely beryllium deposits with deuterium gas. The use of deuterium is of crucial interest for ITER and the fusion community as it possesses a unique set of advantage in regard to cleaning: (i) effective on beryllium, (ii) harmless for the mirror material and (iii) fully compatible with other ITER systems (Neutral Beam Injection, cryo-pumping . . .). Mirrors with a Be deposited films, as well as mirrors exposed in JET-ILW heavily contaminated with beryllium, are employed in this study and two sputtering regimes, at low and high deuterium energy are studied.

The performances of next step fusion facilities, such as ITER, will strongly depend on the ability to monitor and protect the vessel walls from excessive heat loads coming from the plasma power deposition. Infra-red (IR) thermography systems are commonly used in tokamaks to fulfill such requirements by providing thermal images of the plasma facing components (PFCs) under plasma exposure. However, with the introduction of all-metal walls in fusion devices, the significant contribution of reflected flux in the collected flux by the cameras will affect the interpretation of IR measurements, leading to

inaccurate PFC temperature estimation. This could lead to excessive interruptions of the plasma shots and limitations on scenario development towards high performances. The development of a photonic simulation taking into account the contribution of the reflected flux in the collected flux for surface temperature evaluation is, therefore, essential to discriminate the parasitic light-reflection to other thermal events with a real risk for the machine protection. Furthermore, in order to get accurate results, this simulation will certainly have to be based on experimental data set for different PFC materials. Chapter 6 start by describing a photonic simulation carried out using the ray tracing software SPEOS taking into account the multiple inter-reflections of the ray in the vacuum vessel. In the following experimental section, a new redesigned Basel University Laboratory Goniometer (BULGO) will be presented with a description of the apparatus, the measurement and calibration procedure, and the assessment of the accuracy of the device. Directional and total emissivity are also deduced by indirect measurements. The results are presented for tunsgten samples at different roughness. Tungsten is the material chosen for the most critical component in tokamak (divertor) and which is exposed to highest heat loads and for which the roughness can be changed during experimental campaign (erosion/deposition phenomenon). The relation between reflectance/emittance and roughness will also be discussed in this chapter. Experimental results are then used as input of photonic simulation and the resulting IR synthetic image is compared with the experimental image of WEST tokamak.

In the conclusion, a brief summary of the findings and areas for further research will be presented.

1

Nuclear fusion basics and challenges

NUCLEAR fusion has been actively pursued as a potentially clean and cheap energy source in reactors on earth for over 50 years. This chapter provides a general introduction to nuclear fusion starting with the basic reactions and their cross sections continuing with the conditions for which these reactions occur.

The main elements of a fusion power plant and in particular of a fusion reactor called Tokamak defined as a toroidal chamber carrying a strong toroidal magnetic field to trap a high temperature plasma will then be shown.

The next section will be focusing on one particular component of the tokamak, the divertor that withstands the highest surface heat loads of the fusion machine. The choice of nitrogen as a seeding gas to reduce the power load onto the divertor target plates will be justified based on its radiative properties.

Finally, the formation of ammonia in different tokamaks from a reaction of the seeding nitrogen and the hydrogen isotopes present in the plasma will be discussed followed by a section where the thesis context and outline will be presented.

1.1 Thermonuclear fusion: an overview

1.1.1 Nuclear fusion principles

Nuclear fusion is an energy source which could provide electricity on a large scale. The technology is safe, CO_2 free and does not produce long-lived radioactive waste.

Nuclear fusion copies the process that occurs at the core of the sun and stars in which two light atoms are fused together generating a heavier atom and energy. The energy production comes from the fact that the mass of the products of the reactions is slightly lower than that of the fuels that enter into the reactions. This mass defect is released in a form of energy according to Einstein's mass–energy relationship E=mc^2. Possible reactions that can occur on earth in a fusion reactor in the purpose to produce energy are the following:
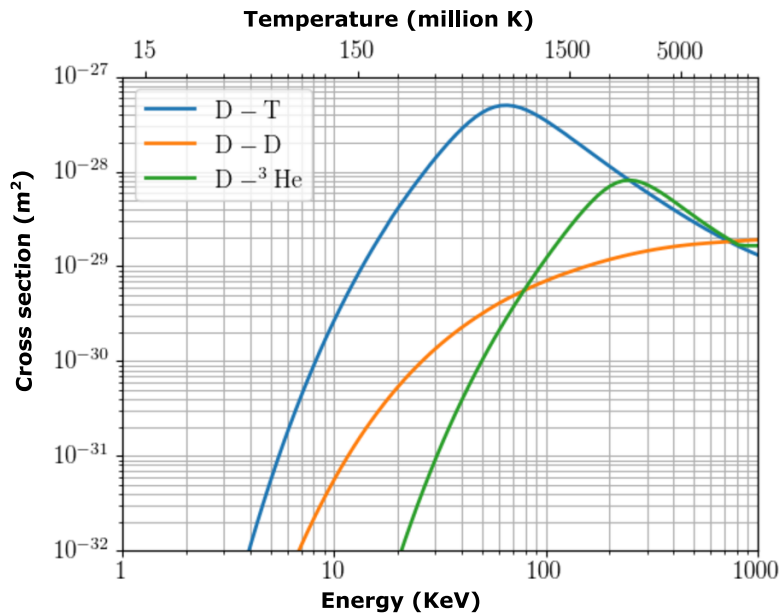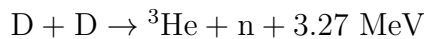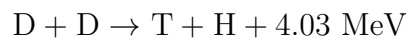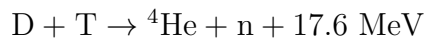
Figure 1.1: *The cross section versus particle energy for D-T, D-D and D-He fusion reactions (from [6])*
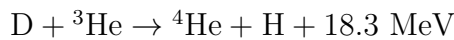
$$D + {}^3He \rightarrow {}^4He + H + 18.3 \text{ MeV}$$
$$D + T \rightarrow {}^4He + n + 17.6 \text{ MeV}$$
$$D + D \rightarrow T + H + 4.03 \text{ MeV}$$
$$D + D \rightarrow {}^3He + n + 3.27 \text{ MeV}$$
where n and p refers to neutron and proton.

For deciding which nuclei should be the "fuel" in a nuclear fusion reactor, the released energy is not the only criteria. A most important quantity is the cross section, which measures the probability per pair of particles for the occurrence of the reaction. Figure 1.1 shows the cross section of the previously mentioned nuclear reactions as a function of the kinetic energy of the reactant particles. Note that the two deuterium-deuterium fusion reactions that have different products shown in the third and fourth previously shown isotopes reactions are approximately equal in their probability of occurring. Therefore, only one curve (orange line) is shown for both reactions in Figure 1.1. One can notice immediately in this plot that the most probable reaction to achieve for the lowest energy required is the one that has the largest cross-section which is the D-T reaction with a broad maximum at about 65 keV; 100 times larger than the two other reactions. That's why the current fusion research is focusing on deuterium and tritium fuels for the fusion reaction. Deuterium is available in sufficient quantity in the oceans of the world; a quantity which is enough to supply the World's energy needs for millions of years. Tritium, on the other hand, is an unstable isotope of hydrogen in the form of a radioactive gas with a half-life of 12.3 years and is not found naturally but can be "bred" from the lithium element (which is also available in abundance) by means of the neutrons generated during the fusion process.
The high temperature values (hundreds of millions of Kelvin in the upper scale) for

which the DT fusion occurs is required to overcome the Coulomb barrier resulting from the electrostatic repulsion of the two positively charged deuterium and tritium nuclei. Note that in this range of temperature no ordinary matter can exist in the form of either solid or liquid or even gas and fusion is only possible in the plasma state of matter. This involves, from a technical point of view, to confine the plasma at very high temperatures inside a reactor, and at the same time isolating it from the walls to prevent impurities.

1.1.2 Fusion power plant and magnetic fusion reactor

Now that we have looked at the basics of nuclear fusion, we will present in this section the main components of a fusion power plant and in particular of a fusion reactor.

Figure 1.2 shows an example of a nuclear fusion power plant based on DT fusion
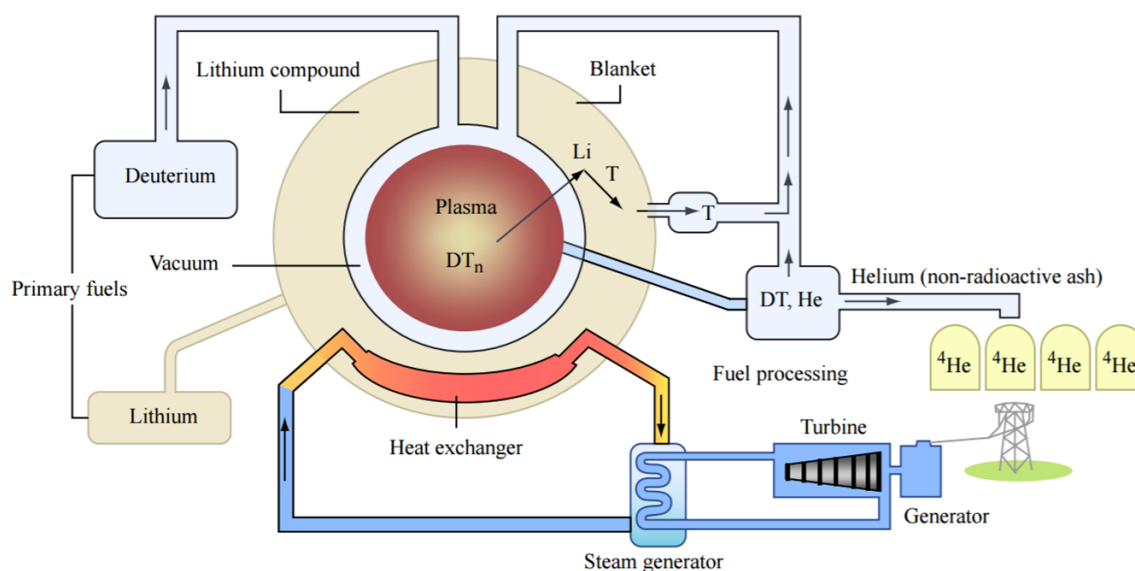
Figure 1.2: *Schematic diagram of a fusion power plant (from [7])*

reactor. Deuterium fuel is injected directly in the reactor while lithium is injected in the blanket surrounding the reactor in order to generate tritium. Tritium is therefore produced by the fusion plant itself as an essential part of the neutron capture system which extracts the heat generated by the fusion reaction. The bombardment of lithium with neutrons splits the lithium into helium and tritium and since neutrons are produced in abundance by the D-T fusion reaction, the reactor can provide its own tritium source. Helium is collected in the exhaust of the plant while both D and T are re-injected again in the reactor where the fusion reaction takes place. The heat energy released by the fusion should be enough to maintain the fusion reaction and to provide a surplus which can be used to generate electricity. The surplus heat from the fusion and the neutron capture by the lithium is used to raise steam in a heat exchanger and the steam is used to drive a conventional turbine generator.

Owing to its very high temperature shown in section 1.1.1, a fusion plasma cannot be confined directly in any material vessels. This problem is solved by confining the plasma and insulating it in a reactor that uses magnetic fields called Tokamak (Russian acronym for toroidal'naya kamera s magnitnymi katushkami (Toroidal Chamber with Magnetic Coils)).

A tokamak is a toroidal chamber which uses a strong toroidal magnetic field to contain a high temperature plasma within the torus. This toroidal field is produced by external electric currents flowing in coils wound around the torus, as shown in Figure 1.3. Superimposed on the toroidal field is a much weaker poloidal field (moving in circles around the plasma), generated by an electric current flowing in the plasma around the torus.
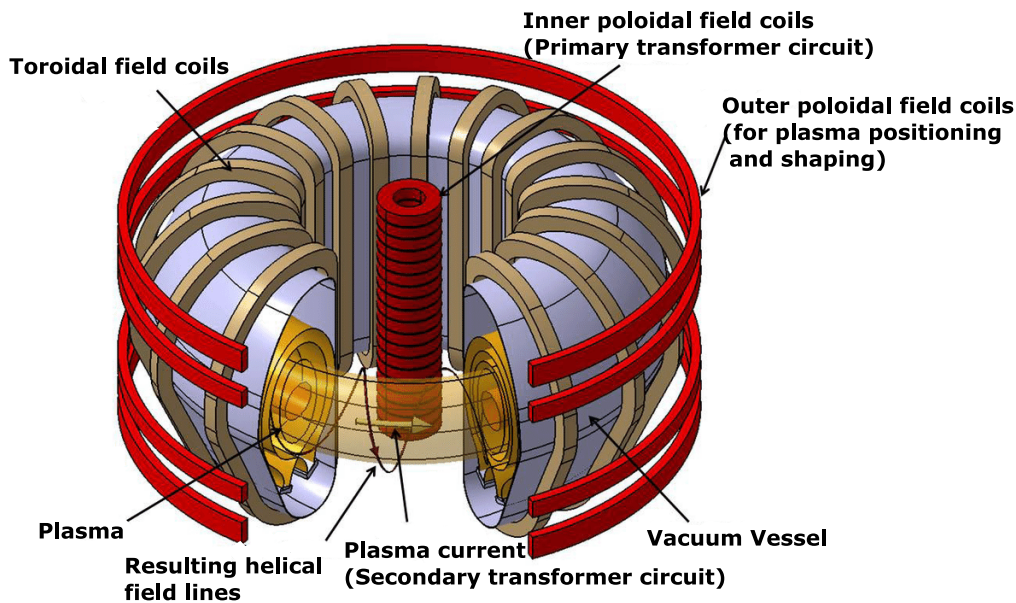
Figure 1.3: *Schematic view of a tokamak fusion reactor [8]*

This plasma current is induced by transformer action where the primary and the secondary coils of the transformer are the inner poloidal coils and the plasma itself, respectively. The combination of the toroidal field from the external coils and the poloidal field from the plasma current produces a helical magnetic field. The outer poloidal field coils are used to control the confined plasma position and shape. It is worth to mention here that the plasma current supplies only up to one third of the temperature required for the fusion reaction (know as ohmic heating) and an additional plasma heating is provided by neutral beam injection and radio frequency heating. In the neutral beam injection process, neutral atoms are injected at high speed into the plasma, ionized and trapped by the magnetic field. As they are slowed down, they transfer their energy to the plasma and heat it. On the other hand, the RF heating enables to transfer large amounts of power to the plasma via high-frequency oscillating currents induced in the plasma by external coils or waveguides.

An example schematic of a tokamak in shown in Figure 1.4. The ITER reactor is

an international tokamak under construction designed to demonstrate the potential for commercial fusion energy by producing a ten-fold return on energy (Q=10), or 500 MW of fusion power from 50 MW of input heating power.

Figure 1.4: *ITER cross-section showing its main components and the materials for plasma facing components (adapted and modified from [9])*

In this figure, the main components of the tokamak are presented. The stainless steel vacuum vessel, maintained by external pumping system, is essential to create th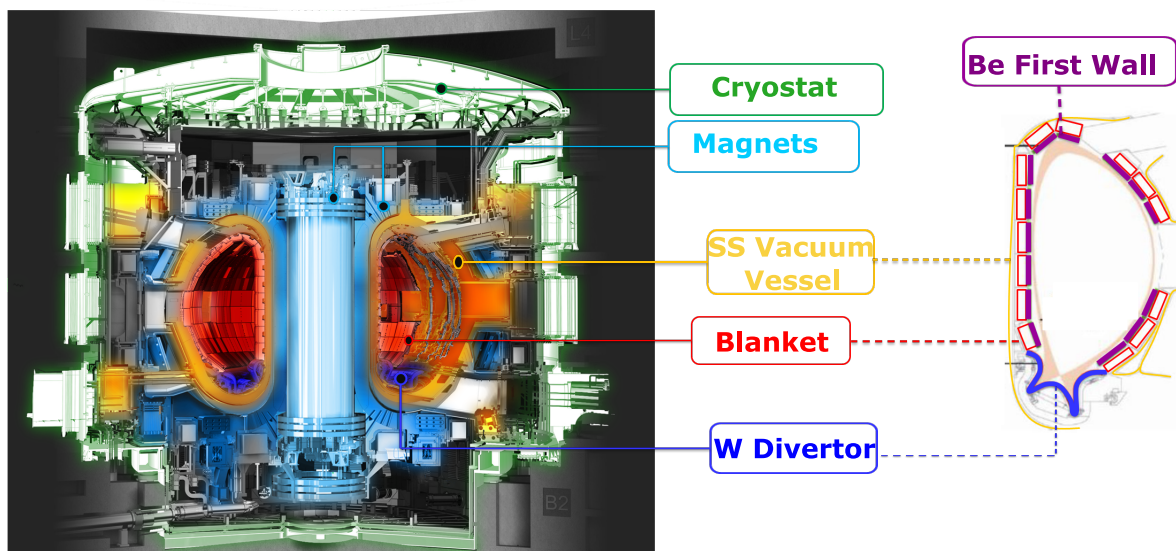e vacuum condition for the D-T plasma and to prevent any atmospheric contamination. The superconducting magnets that confine, shape and contain the plasma using magnetic fields are cooled down by the cryostat. The major functions of the blanket region are to efficiently capture the energy produced by the fusion reactions and transfer the heat to a coolant for electricity generation and to create and extract fresh tritium fuel to enable continuous operation of the fusion energy system. The last major component positioned at the bottom of the vacuum vessel is the tungsten divertor which role is to extract heat and ash produced by the fusion reaction, minimizes plasma contamination, and protects the surrounding walls from thermal and neutronic loads. The choice of the tungsten, a high-Z material, for this component is based on its properties including low tritium retention, low sputtering yield and high melting temperature of 3410 °C to withstand the highest heat loads on the surface (more details in the following section). On the other hand, the first wall region (shown on the right side of Figure 1.4) is the low-Z material beryllium. Due to its affinity to oxygen, Be is an excellent getter material which guarantees plasma discharges with low impurity levels (compared to the carbon used in previous tokamaks). It also exhibits better erosion resistance and hence, a reduced material transport during plasma operation of the fusion device. In addition, Be is characterized by a rather good thermal conductivity to remove the surface heat flux and to avoid overheating of the wall structures.

1.2 Heat loads on W divertor

Several issues related to materials for future fusion reactors, including ITER, need still to be tackled. Among those are the issues related to the divertor surface and in particular to its power handling capabilities.

The ITER divertor is composed of 54 stainless steel cassettes (shown in Figure 1.5) bearing vertical targets, themselves constituted of a series of plasma-facing units made up of chains of W monoblocks bonded to a CuCrZr cooling tube. This divertor will need to withstand steady-state heat fluxes of up to 10 MW.m^{-2}. Much more critical are the transient loads (20 MW.m^{-2}) during which considerable fraction of the plasma energy is deposited on a localized surface area of the divertor in a short period of time (few seconds). These loads that can deposit energy densities of several ten MJm^{-2} are caused by plasma instabilities, like disruptions or Edge Localized Modes (ELMs) defined as disruptive instability occurring in the edge region of the plasma. Transient loads lead to enhanced erosion, possible excess loads (melting) or fatigue effects on thermo-mechanical properties.
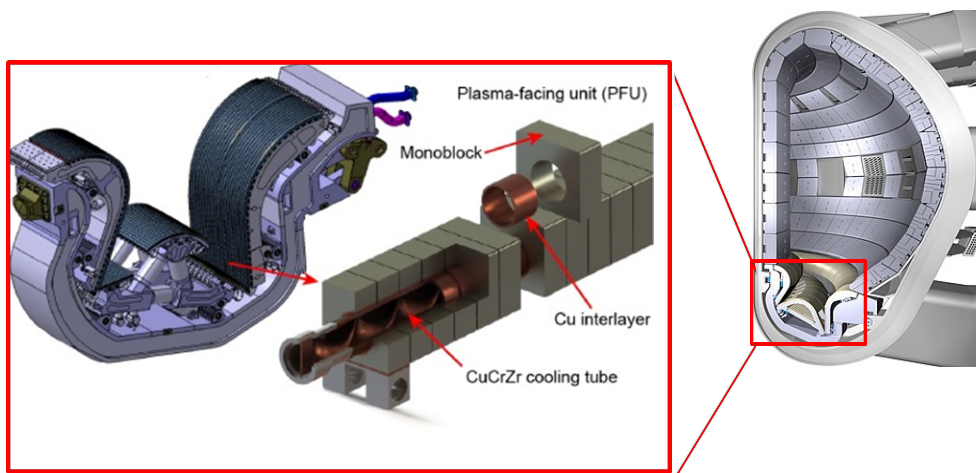
Figure 1.5: *The ITER tungsten divertor cassette [10]*

As shown in Figure 1.5, one solution based on actively cooled tungsten components has been developed for the divertor where the cooling medium will be water. However, this solution would not be enough to withstand the excessive heat loads on the divertor. An additional method consists in injecting radiative impurity gases. A significant fraction of the radiation cooling could be provided by electromagnetic radiation from excited impurity species in the plasma. In particular, for ITER, impurities will be seeded into the edge plasma to radiate 60% of the incoming power and reduce heat loads onto the divertor plates to values compatible with the divertor power handling capabilities [11]. Seeding gases that are currently under investigation in divertor tokamaks like JET (Joint European Torus), ASDEX Upgrade (Axially Symmetric Divertor Experiment) and foreseen for ITER are nitrogen (N$_2$), argon (Ar) and neon (Ne) or a mix of them. Ar gas was identified as the best candidate for the simultaneous enhancement of core and divertor radiation [12] in the case where an elevated main chamber

radiation is desired as well. As shown in Figure 1.6, the total power loss calculated as the sum of line radiation, recombination-induced radiation and bremsstrahlung indicates that the Ar radiates both a low and high temperatures which makes it a good core and divertor radiator while nitrogen radiates at lower temperature (than Ne and Ar), therefore, closer to the divertor plates without degrading the confined plasma.
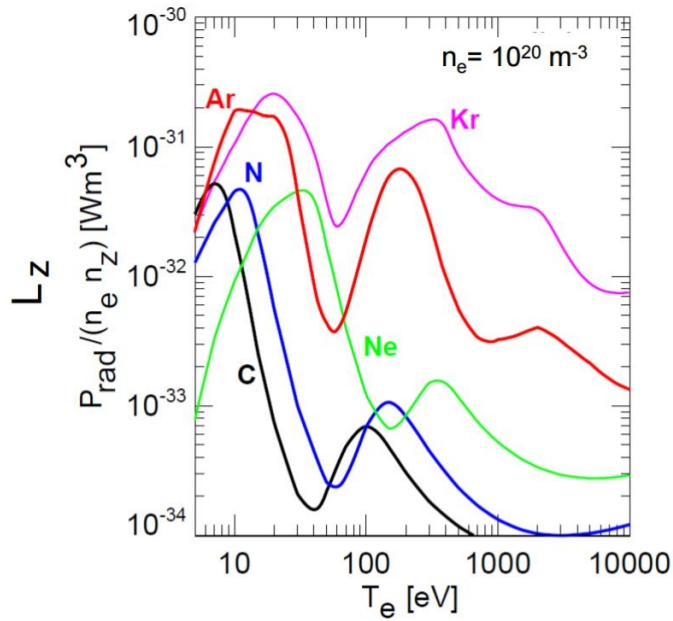
Figure 1.6: *Radiative loss parameter Lz for seed impurities as the sum of line radiation, recombination induced radiation and bremsstrahlung. (from [12])*

In particular for ITER, nitrogen is the preferred seeding species considering the fact that strong core radiation will not be permitted due to the proximity of the ITER heating power (150 MW = 50 MW of external heating plus 100 MW generated by the alpha particles from the fusion reaction) to the low-to-high confinement transition (L-H) threshold power (around 70 MW). Moreover, nitrogen seeding was shown to lead to improved confinement (and hence performance) in full-metal tokamaks such as JET-ILW (JET ITER-Like Wall) and ASDEX Upgrade [13,14].

1.3 Formation of ammonia under fusion-relevant conditions

When nitrogen is used as a seeding gas in the tokamak, the dissociated N atoms chemically react with H and its isotopes (D/T) to form ammonia (NH_3) isotopologues.

The formation of ammonia during nitrogen-seeded discharges has been investigated in detail in ASDEX-Upgrade [15–20] by analyzing the exhaust gases using mass spectrometers. An initial experiment was performed by injecting directly hydrogenated ammonia into the empty vessel in order to calibrate the mass spectrometer sensitivity

and determine the ammonia cracking pattern. Interestingly, up to 85% of the injected NH_3 was not recovered and was therefore retained by the vessel walls. The formed NH_3 in three consecutive N_2 seeded discharges was then quantified by a gas balance equation between injected, recovered and missing deuterium and nitrogen atoms. The interpretation of such results was challenging due to the additional presence of water and methane and due to isotope exchange reactions of deuterated ammonia with H in the pump ducts that lead to the spectrometers. In the first discharge, it was found that 30 % of the injected N_2 molecules were missing in the balance, i.e. they were not pumped by the cryo and turbo-molecular pumps and only about 3 % of the injected nitrogen was recovered as ammonia. After three similar discharges the amount of pumped N_2 was roughly equal the amount of injected N_2, thus closing the balance. In this third discharge, around 8 % of the injected nitrogen was recovered as ammonia. However, these data should be treated carefully as they were obtained following other experiments where the wall loading was not controlled and identified at the start of the series and the RGA did not reach its optimal performance [16]. Besides, the presence of methane in AUG has a direct effect on both the formation and the destruction of the produced ammonia through the reactions [21]:

$$NH_3 + CH_3 \longrightarrow HCN + 2H_2 + H$$

$$NH_2 + CH_4 \longrightarrow HCN + 2H_2 + H$$
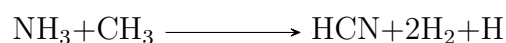
The formation of ammonia in the current world's largest operational tokamak JET-ILW (tungsten divertor, beryllium first wall) was also reported [17, 18, 22, 23]. The liquid helium and the liquid nitrogen (LN) cryopanel of JET cryopumps regeneration was performed. The cooled panels were warmed and the exhaust gases were analyzed by RGA. About 0.4 % of the injected nitrogen during the experimental campaign was converted to ammonia molecules. Furthermore, by performing global gas balance, it was found that about 52 % of the total injected nitrogen amount was not recovered from which 15 % get transformed into ammonia built up on all inner surfaces and in the pump ducts [17].

Experiments with nitrogen deuterium plasmas were also performed in linear plasma devices which produce a high density and low temperature plasmas resembling that expected in the ITER divertor. In GyM (acronym for Gyrotron Machine) linear device, liquid ion chromatography of the collected exhaust in LN trap results show a nitrogen to ammonia conversion in the range of 12 to 26 % depending on the total pressure and plasma electron temperature (varied by RF power applied) for a fixed nitrogen-deuterium partial pressure ratio [24]. In the Pilot-PSI [25, 26] linear plasma device, the conversion rate of injected nitrogen to ammonia was measured to be 16 %.

2

Plasma-activated catalytic formation of ammonia from N$_2$/H$_2$

Plasma catalysis, sometimes described as plasma-assisted catalysis, plasma enhanced catalysis, plasma-driven catalysis or plasma–catalysis coupling is defined as a combination of a catalytic process on a material surface with a gaseous discharge (plasma). In this process, the plasma plays the role of generating reactive species that react on the catalyst to form the desired product. As a result, the performance achieved by hybridization of the highly reactive plasma and the highly selective catalyst is higher than the summation of plasma-alone and catalysis-alone. This effect is referred to as the synergistic effect of plasma catalysis.

In the fusion device, ammonia is formed as a result of this synergistic effect between the species from the fusion plasma and the plasma facing components acting as a catalyst. The main questions addressed in this chapter are therefore related to the formation mechanism of ammonia under these conditions.

Chapter 2 begins by laying out the theoretical background of surface catalysis and low temperature plasmas as well as the resulting interactions taking place when combining them together. Besides, a summary of the dominant reaction pathways for ammonia synthesis from hydrogen-nitrogen plasma on a catalytic surface will be presented. In the following part, a detailed description of a newly built setup, with the specificity of being a quartz vacuum chamber (no metal), as well as the experimental procedure developed for the ammonia production study will be presented. Two fusion relevant materials playing the role of catalysts for the ammonia production were investigated: tungsten and stainless steel. While the W constitutes the divertor surface material in ITER, the SS is used for the vacuum vessel, the divertor cassettes, the shield block and the Port Plug front surface. Fundamental information about the nature of the reactive processes occurring during RF plasma-assisted ammonia synthesis will be demonstrated based on the results of the surface chemical analyses performed by XPS.

2.1 Theoretical background

2.1.1 What is heterogeneous catalysis

Heterogeneous catalysis plays a key role in a wide range of industrial production techniques of various chemicals. Currently, 85 to 90% of the products of chemical industry are made by catalytic processes [27]. As a definition, heterogeneous catalysis represents an interaction between two different phases (in most cases a solid and a gas) where the rate of a resulting reaction is increased without modifying the overall standard Gibbs energy change in the reaction. As shown in Figure 2.1, a catalytic reaction can be described as a cycle where molecules A and B diffuse to the surface to forms chemical bonds (adsorption) and then react into the final product P that gets detached from the catalyst. The catalytic surface recovers therefore its initial state for the following catalytic cycle.
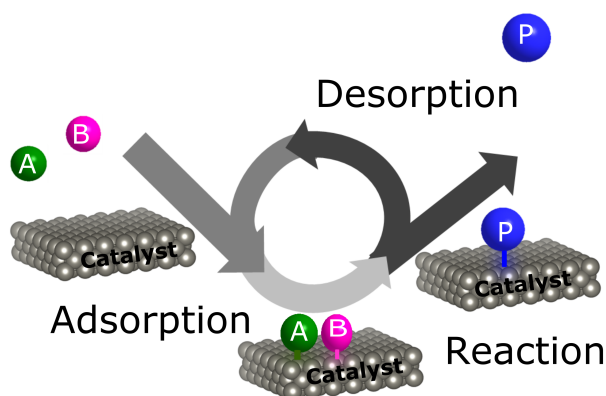
Figure 2.1: *Heterogeneous catalytic cycle (Adapted and modified from [28])*

The catalyst acts by lowering the energy of the transition states thus lowering the activation energy defined as the energy required to overcome the reaction barrier. The potential energy diagram for uncatalyzed and catalyzed reactions as well as a schematic of the reactions taking place on the catalyst surface are presented in Figure 2.3. Compared to a catalyzed reaction, the activation energy of non catalyzed reaction is high. In order to lower this barrier and increase as a consequence the reaction rate, the catalyst offers an alternative path for the reaction through elementary steps with lower activation energies.

One particular example of heterogeneous catalysis is the synthesis of ammonia (NH$_3$) from its elements (N$_2$ and H$_2$) considered as one of the most important discoveries in the history of the science of catalysis, in large part because of its industrial application in the production of synthetic fertilizers which contributed enormously to the sustainment of mankind's population [29]. It is often referred to as the "most important invention of the 20th century" [30]. Developed in 1913 by BASF, ammonia was formed in the

first Haber-Bosch process from a reaction between N_2 and H_2 using an Fe_3O_4 catalyst. The energy diagram of the formation reaction of ammonia from nitrogen and hydrogen is shown in Figure 2.2. The elementary steps of the reactions have been identified by G. Ertl [31] and can be written as:

$H_2 \; + \; * \xrightarrow{\hspace{2cm}} 2H(s)$

$N_2 \; + \; * \xrightarrow{\hspace{2cm}} 2N(s)$

$N(s) \; + \; H(s) \xrightarrow{\hspace{2cm}} NH(s)$

$NH(s) \; + \; H(s) \xrightarrow{\hspace{2cm}} NH_2(s)$

$NH_2(s) \; + \; H(s) \xrightarrow{\hspace{2cm}} NH_3(s)$
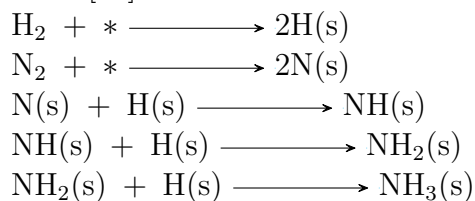
Where $*$ denotes schematically an adsorption site on the surface.
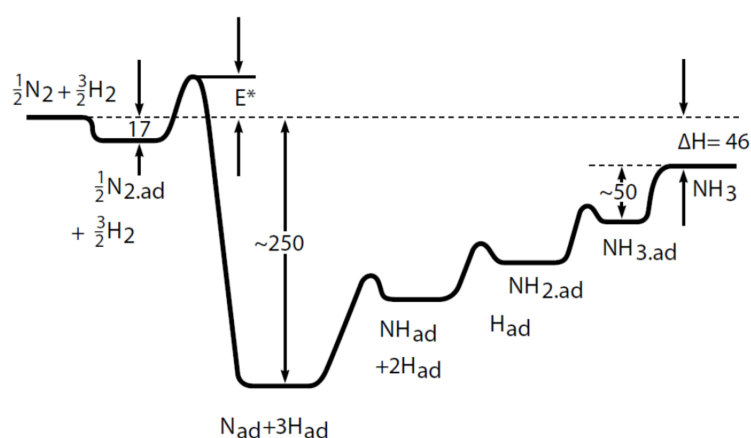
Figure 2.2: *Energy diagram of the formation reaction of ammonia from nitrogen and hydrogen. Energies are given in kJ.mol-1 (from [29])*

The process takes place at a temperature of around 773 K and a pressure of 300 bar. The requirement for such high temperature (and as a consequence high pressure to make the equilibrium favor the reaction via Le Chatelier principle), as well as catalytic material, is justified by the high activation energy of N_2 dissociation due to the strength of the triple bond in the nitrogen molecule. This hints at the possibility of efficient formation of ammonia in an environment where the reactants are already dissociated i.e via plasma catalysis.

2.1.2 Low temperature plasmas

Plasmas represent the fourth state of matter composed of neutral atoms and molecules, radicals, excited states, ions and electrons. In particular low temperature plasmas (LTPs) have characteristic electron energies of a few eV to 10 eV (equivalent temperature range 10^5 to 10^6 K) with ionization degrees that are typically small. Depending on how the power is coupled into the plasma, a variety of different LTPs can be generated, including microwave discharges, direct current (dc), capacitively coupled radio

frequency (RF), and inductively coupled RF sources, dielectric barrier discharges, gliding arcs, plasma jets and plasma torches.

The reactivity of species present in LTPs, as well as their relatively low temperature, enables them to be used in combination with heterogeneous catalysis by increasing the reactivity at surfaces in contact with the plasma. This plasma surface interaction will be detailed in the next section and we will now give an overview about the excitation mode of species that are present in the plasma and would react on the surface for catalyzing a reaction.

Electron-impact reactions with molecules inside the plasma can generate dissociated, ionized, electronic excited molecules or ground state excited molecules (vibrational and rotational). The typical threshold energies required to generate these species are summarized in table 2.1 in an increasing energy order.

Rotational excitation	0.01 to 0.1 eV
Vibrational excitation	0.1 to 1 eV
Electronic excitations	1 to 10 eV
Dissociation and ionization	5 to 20 eV

Table 2.1: *Molecular excitation modes with the threshold energies to generate them by electron impact*

Except for rotational excitation, all other electron-impact reactions have threshold energies close to or higher than the activation energy of heterogeneous catalytic reactions [32]. Therefore, the active species generated in the plasma would contribute to the surface catalytic process by providing some of the energy required for overcoming elementary steps activation barrier.

2.1.3 Plasma surface interaction in plasma catalysis

Now that we have looked at the basics of surface catalysis and some properties of low temperature plasma separately, we will consider in this section how they may be combined and what may be the interactions that result from this hybridization i.e in plasma catalysis processes.

In a plasma catalytic setup, the catalyst may be combined with the plasma in two ways: either as a one stage catalytic system also called in plasma catalyst (IPC) or as a two stage plasma catalytic system referred to as post plasma catalyst (PPC) [33]. In the first, the catalytic material is placed directly into the discharge zone of the plasma while for the PPC system the catalyst is placed in spatially different areas from the plasma, usually upstream or downstream of the discharge zone. Unlike IPC system, for a PPC system the plasma role is limited to modifying the gas composition prior to interaction with the catalyst before reaching the surface and only long-lived species can reach the surface excluding species that could contribute in the catalytic process like high reactive radicals, ions, electrons and photons. Therefore, the experiments performed which results will be shown in this chapter will be focusing on IPC processes.

The key difference between plasma catalysis and thermal catalysis is the existence of abundant active species (excited species, radicals, and positive/negative ions) in the gas discharge as well as the presence of a voltage potential and a current flow across the catalyst. The active species generated in plasma changes the status of gas-phase reactants for surface catalysis while the other two phenomena affect the physical and chemical properties of the catalyst.

Change of the reactants   As explained in 2.1.2, electron impact reactions in LTP generate radicals, ions, electronically, vibrationally and rotationally excited molecules. The possible impact of these species on the catalytic reaction was reported by different studies [32, 34–37] and can be summarized as follow:
(i) species in the rotational state have no sufficient internal energy to induce further reaction.
(ii) ions and electronically excited species would get de-excited before they reach the catalyst surface.
(iii) only radicals and vibrationally excited species can be considered for plasma catalysis.
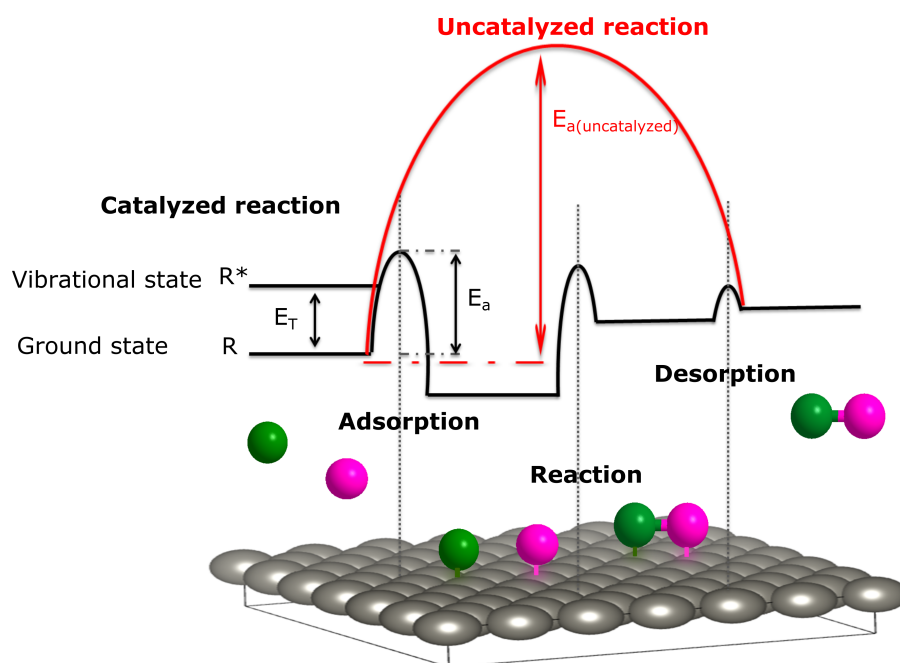
Figure 2.3: *Potential energy diagram of uncatalyzed and catalyzed reactions illustrating how catalysis accelerate chemical reactions and in particular how the vibrationally excited species in plasma catalysis accelerate the catalytic reaction. R and R* represent gas-phase reactants in ground state and in vibrational state, respectively. E_a is the activation barrier of chemisorption for R and E_T is the threshold energy for the formation of R* through electron-impact reaction. $E_{a(uncatalyzed)}$ is the total activation energy for an uncatalyzed reaction (Adapted and modified from [36])*

17

Radicals contribute in the catalytic reaction by assisting the adsorption step described as the primary process enabling molecules to be transformed at the surface. Depending on the nature of adsorbate-reactant interaction, this process may proceed either through physisorption of chemisorption (see chapter 4). Most of the chemisorption reactions of molecules are dissociative. Radicals and dissociated atoms from the plasma increase, therefore, the chemisorption process by providing already dissociated species, very often considered as the rate limiting factor of the adsorption reaction. This is the case in particular for the ammonia catalytic formation from hydrogen and nitrogen where the dissociative adsorption of nitrogen is the rate limiting step of the process. Furthermore, radical where shown to have a high sticking coefficient [32, 36], enhancing therefore the adsorption step of the catalytic cycle.

Vibrationally excited molecules may also enhance the catalytic reaction by lowering the effective activation barrier required for chemical adsorption. As illustrated in Figure 2.3, the vibrational energy increases the energy level of the reactant. Relative to the barrier with respect to the vibrational ground state, the effective barrier is thus lowered from E_a to E_a-E_T where E_a is the activation barrier of chemisorption and ET is the threshold energy for the formation of and excited molecule/atom through electron-impact reaction. Some previous research [38–42] have in particular demonstrated how of the vibrationally excited states promote the dissociative adsorption of N$_2$, the rate limiting step for ammonia formation.

Change of the surface   Upon surface impact of energetic species accelerated by the potential difference between the plasma (V$_P$) and the floating surface (V$_F$), three processes can take place that can change the surface morphology and properties: physical sputtering, chemical etching and implantation.
Implantation occurs when energetic ions penetrate the catalyst surface and become implanted in the bulk. At LTP implantation, is very unlikely to play a role due to the small penetration depth to the relatively low energy ions impacting the surface (in the order of 10 eV). For instance, the penetration depth of nitrogen and hydrogen ions with 10 eV energy in the W surface is 0.3 nm and 0.7 nm respectively (obtained from SRIM Software [43] simulations).
Physical sputtering can be also expected to be of minor importance in plasma catalysis. Depending on the type of surface, the impacting particles, their angle of incidence and their kinetic energy as well as the mass ratio between sputtering ions and the surface atoms, physical sputtering usually requires energies equal to or larger than 10 eV [37, 44] where the yield at this threshold energy is very low. Chemical etching, finally, requires the formation of a volatile compound through a chemical reaction between the impinging species and the surface species. On metallic surfaces in particular, the formation of these volatile compounds is very unlikely and the chemical etching does not take place.

On the other hand, the presence of the plasma can affect the catalytic process through surface heating or surface charging. Possible heating of the catalyst can occur via the radiation emitted by the plasma or by energy transfer from the active species upon impact on the surface. The increase in the substrate temperature influences the

surface catalytic activity as well as the elementary processes such as adsorption, diffusion, chemical surface reactions and desorption of surface species. Moreover, when the catalytic surface is in contact with the plasma, it usually acquires a negative charge due to the much higher mobility of the electrons compared to the ions from the discharge. It was also reported that the presence of the plasma and specifically the presence of a voltage and a current (or charge accumulation) on the catalyst surface resulting from the plasma induces a change in work function of the catalyst [36, 45] defined as the energy required for an electron to be removed from the catalyst. Based on the established understanding of a catalytic reaction and in particular of the chemisorption as the donation and acceptance of an electron between the adsorbate and surface atoms, the electric surface properties change by the plasma would have a direct influence of the catalytic reaction [36, 46].

2.1.4 General overview of ammonia formation mechanisms

The heterogeneous catalytic reactions are generally classified into two mechanisms: Eley-Rideal (E-R) and Langmuir-Hinshelwood (L-H) (see Figure 2.4). E–R reaction stands for a reaction between one chemically adsorbed reactant and one incoming reactant directly from the gas phase, without being accommodated at the surface. The resulting product molecule subsequently desorbs from the surface. In L-H mechanism, both reactants first adsorb onto the surface before a reaction takes place. Surface diffusion facilitates interaction between adsorbed molecules and the final reaction product gets desorbed.

For ammonia synthesis from hydrogen and nitrogen, as illustrated in Figure 2.4, L-H mechanism consists of a recombination of chemisorbed atomic nitrogen and hydrogen to NH_3 at the surface of the catalyst with NH and NH_2 as reaction steps. However, for the E-R two chemical pathways are possible: either the hydrogen or the nitrogen adsorbs on the catalyst and react with the second species from the gas phase.

In the literature, few researchers have addressed the question of ammonia formation mechanism from low pressure hydrogen-nitrogen plasma. Based on a chemical kinetics model, Shah et al [47] calculations reveal that the Langmuir-Hinshelwood mechanism predominantly contributes to the formation of $NH_2(s)$ and NH_3, while the Eley-Rideal mechanism contribution is negligible. On the other hand, Carrasco et al [48] focused on the ion and neutral chemistry in N_2/H_2 mixtures, with experiment and modeling work in a low-pressure hollow cathode discharge. They showed that both E-R and L-H surface interactions were found to be important in the ammonia production mechanism. Furthermore, a model developed by Body et al [49] demonstrated that the dominant ammonia production mechanism is found to be the Langmuir-Hinshelwood reaction between adsorbed atomic hydrogen and $NH_2(s)$ above 25 % hydrogen concentration and Eley-Rideal reaction between free atomic hydrogen and $NH_2(s)$ for lower hydrogen proportions. Accordingly, investigating the ammonia formation in low temperature plasma catalysis represents one of our objectives in this chapter and the results will be presented in section 2.3.
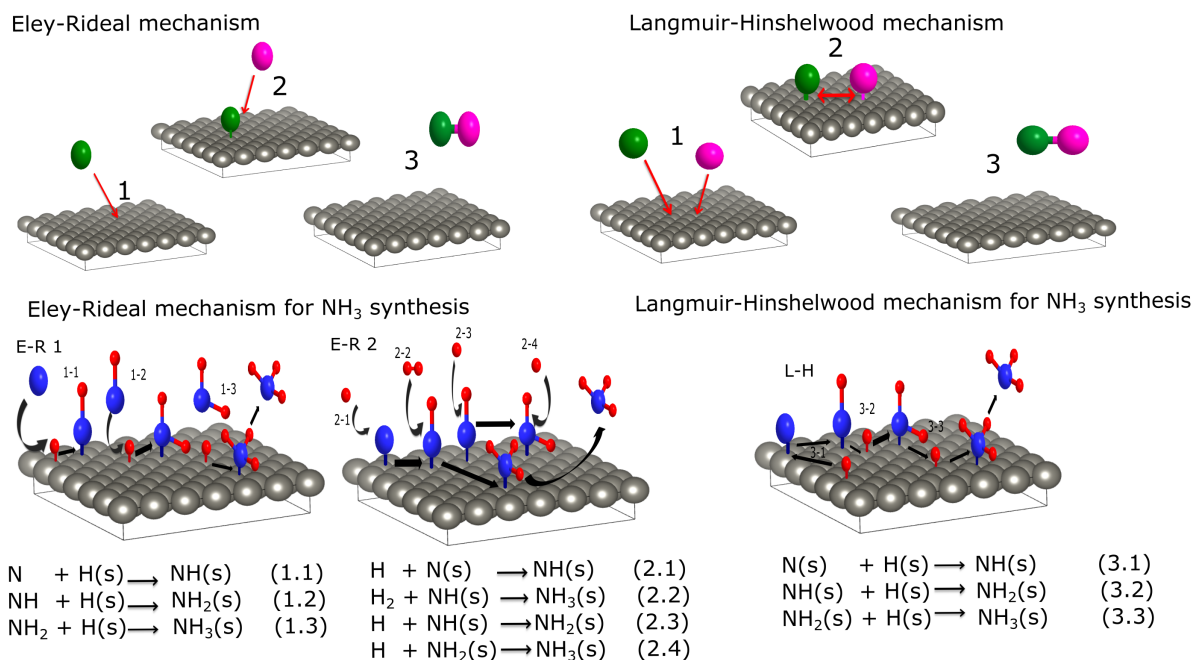
Eley-Rideal mechanism

Langmuir-Hinshelwood mechanism

Eley-Rideal mechanism for NH$_3$ synthesis

Langmuir-Hinshelwood mechanism for NH$_3$ synthesis

E-R 1

$$N + H(s) \longrightarrow NH(s) \quad (1.1)$$
$$NH + H(s) \longrightarrow NH_2(s) \quad (1.2)$$
$$NH_2 + H(s) \longrightarrow NH_3(s) \quad (1.3)$$

E-R 2

$$H + N(s) \longrightarrow NH(s) \quad (2.1)$$
$$H_2 + NH(s) \longrightarrow NH_3(s) \quad (2.2)$$
$$H + NH(s) \longrightarrow NH_2(s) \quad (2.3)$$
$$H + NH_2(s) \longrightarrow NH_3(s) \quad (2.4)$$

L-H

$$N(s) + H(s) \longrightarrow NH(s) \quad (3.1)$$
$$NH(s) + H(s) \longrightarrow NH_2(s) \quad (3.2)$$
$$NH_2(s) + H(s) \longrightarrow NH_3(s) \quad (3.3)$$

Figure 2.4: *Schematics and equations of ammonia formation surface reactions via E-R interaction (left) and L-H interaction (right)*

2.2 Experimental section

2.2.1 Plasma exposure systems

2.2.1.1 Metal-free UHV chamber

As shown in chapter 4, ammonia molecules have a high sticking probability on metal surfaces and, in particular, on SS surface. Measuring the production of ammonia in a standard stainless steel vacuum system would, as a consequence, affect the measurement itself. Therefore, a new in-house built plasma reactor (Figure 2.5) was used to perform experiments of NH$_3$ synthesis from H$_2$/N$_2$ plasma.

This setup consists of a cylindrical quartz tube of 35 (31) mm outer (inner) diameter and 1405 mm length connected to a waveguide surfatron plasma source (350 mm length). The plasma is created in the tube through a matching network by a 13.56 MHz RF generator at a typical power of 120 W. Processing gases are introduced to the reaction chamber via the surfatron by mass flow controllers. The pressure is monitored by an MKS baratron capacitance manometer. Inside the tube, a 50×10 cm^2 rolled foil of the catalytic surface of choice (tungsten with a purity of 99.97 % or stainless steep with a mass percent composition shown in Table 2.2) is placed and can be heated with a furnace up to a maximum temperature of 1000 °C. The ratio of the catalyst foil to the entire quartz surface is 1/3. The temperature is measured by a thermocouple placed in the outer wall of the quartz tube inside the furnace region. The sample was at the floating potential and we verified experimentally by connecting the sample to the ground that the ammonia production is not depending on the sample potential.
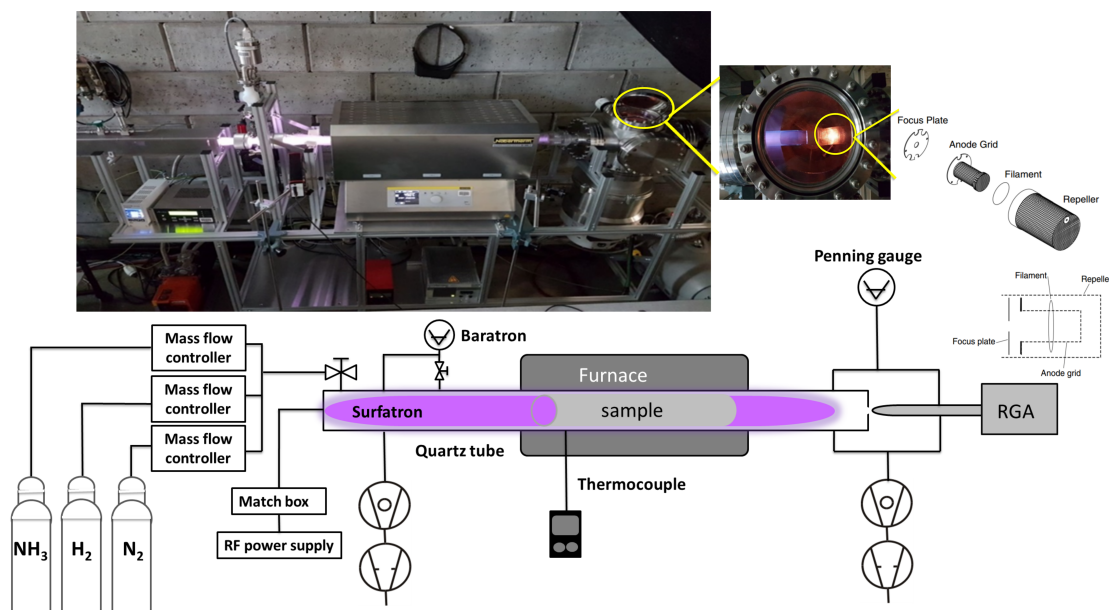
Figure 2.5: *Schematic and real picture (on top) of the RF plasma reactor and surrounding equipment for gas inlet and outlet*

Element	Fe	Cr	Ni	Mo	Mn	Si	N	P	C	S
%	69.52	16.9	10.1	2.08	1.74	0.46	0.048	0.032	0.019	0.001

Table 2.2: *Chemical composition of the stainless steel foil*

On the other side of the quartz tube, a quadrupole mass spectrometer (SRS Residual Gas Analyzer RG A200) is connected through a 2 mm diameter PEEK pinhole. The residual gas analyzers is used for both qualitative and quantitative analyses of gas species resulting from the plasma. It ionizes, separates components of the gas to create various ions, and then detects and determines the mass-to-charge ratios. After passing the PEEK pinhole, gas molecules get accelerated to the ionizer of the RGA where positive ions are produced by electron-impact ionization. The main parts of the ionizer are: the repeller, the anode grid, the filament and the focus plate. In order to fully pump the NH_3 from the RGA head between each experiment, the repeller, the anode grid and the focus plate (shown in Figure 2.5) are coated with gold. The choice of the gold coating is based on the XPS results shown in chapter 4 showing a full desorption from a Au surface after pumping. In order to get a good background pressure of around 8×10^{-9} mbar in the RGA chamber (measured by a Penning gauge), the system is pumped from two sides through a turbo and a primary pump. However, during the plasma process (typical pressure value of 5×10^{-6} mbar), gases are pumped only through the RGA chamber in order to detect all gas species.

2.2.1.2 Conventional stainless steel UHV chamber

For identifying intermediate surface species formed during the ammonia synthesis process, chemical analyses were performed using XPS after tungsten deposition and

hydrogen-nitrogen plasma. The experiments were carried out in an UHV deposition and analysis system, which is shown schematically in Figure 2.6.

It consists of a sputtering chamber connected by a transfer chamber to a load-lock chamber (where the sample is introduced) and a photoemission chamber. The background pressure of each separate chamber was achieved by an individual conventional pumping system. The sputtering chamber is equipped with rotatable biasable and heatable sample holders and one quartz crystal microbalance, allowing the calculation of the deposition rates. A water cooled magnetron and a plasma source are also mounted on the deposition chamber. Various process gases can be introduced directly to the chamber for the deposition of the surface material by magnetron sputtering or through the plasma source for exposure the deposited surface to the gas discharge.

Following the deposition and plasma exposure of the surface, the sample can be transferred without breaking the vacuum to the analysis photoemission chamber for XPS measurements. The electron spectrometer is equipped with a hemispherical analyzer (Leybold EA10/100 MCD) and a non-monochromatized MgK X-ray source (hν = 1253.6 eV) was used for core level spectroscopy. The binding energy (BE) scale was calibrated using the Au 4f$_{7/2}$ line of a cleaned gold sample at 84.0 eV.
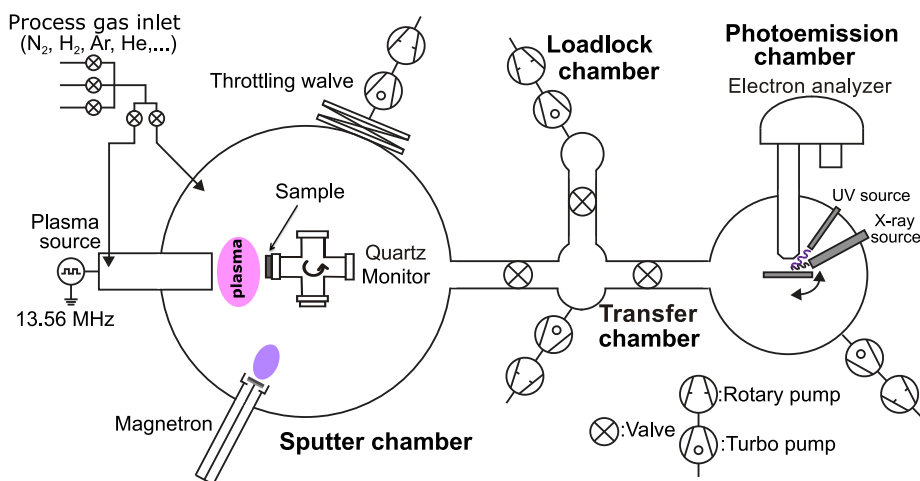

Figure 2.6: *Schematic of the plasma exposure facility with in-situ photo-electron spectrometer.*

2.2.2 Characterization techniques

2.2.2.1 Residual gas analysis

A Residual Gas Analyzer (RGA) is mass spectrometer of small physical dimensions that analyzes gases by ionizing some of the gas molecules, separating the resulting ions according to their respective masses and measuring the ion currents at each mass. The RGA consists basically of a quadrupole probe, and an electronics control unit connected to the probe and contains all the electronics necessary to operate the instrument. As shown in Figure 2.7, the RGA probe is composed of three parts: the ionizer, the quadrupole mass filter and the ion detector. In the Ionizer, the neutral gas atoms or

molecules are converted into positive ions by getting bombarded with electrons derived from a heated filament and accelerated towards the anode grid (which is positively charged with reference to the filament and ground). The repeller, which completely encloses the ionizer, is biased negative relative to the filament and prevents the loss of electrons from the ion source. The formed ions within the anode grid volume are then extracted from the ionizer by the electric field produced by the difference in voltage bias between the anode grid and the focus plate.
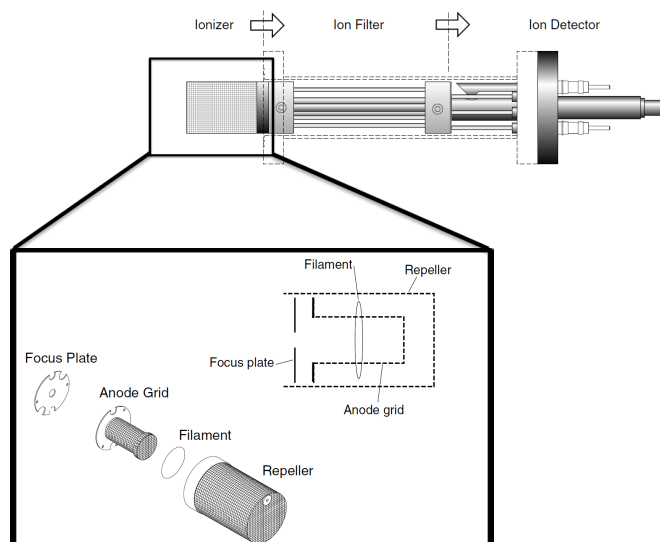

Figure 2.7: *Schematic of the probe and ionizer components of the residual gas analyzer (Adapted from [50]*

The accelerated and focused positive ions are then sorted out according to their respective masses by employing electric and/or magnetic fields in the ion filter. The ions that pass through the filter are focused toward the ion detector and the ion current is either directly measured with a Faraday cup or using an optional electron multiplier detector.

2.2.2.2 X-ray photoelectron spectroscopy

X-ray photoelectron spectroscopy is a quantitative technique that measures the elemental composition of a material surface (with an average probing depth of 5 nm) as well as the chemical states and the electronic states of its elements. As illustrated in Figure 2.8, the sample is irradiated with an X-ray source (either monochromatic of unfiltered Al Kα or Mg Kα) with an energy value of hν. Electrons from the core energy level that are attached to the atomic nuclei with the binding energy E_B get ejected and escape for the material to the vacuum with a kinetic energy E_{kin}. The ejected photoelectrons travel through the electron optical system to the electron energy analyzer which will disperse the emitted photoelectrons according to their respective kinetic energy. On the end of the analyzer, the electrons hit the detector and their kinetic energy is measured. The measured kinetic energy along with the known X-ray

photon energy and the material work function (Φ) are used to determine the electron binding energy through the formula E_B = hν - E_{kin} - Φ.
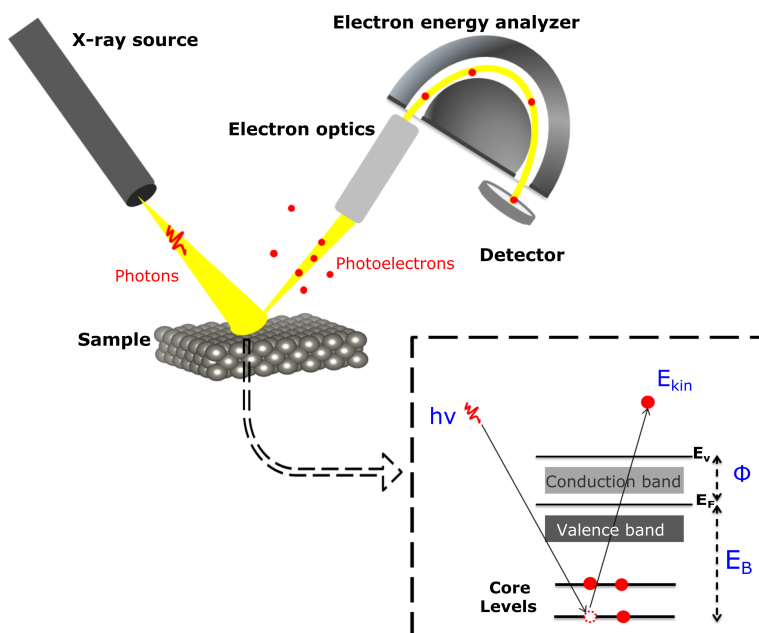

Figure 2.8: *Schematic of the X-ray photoelectron spectrometer and its working principle*

2.2.3 Experimental procedure

2.2.3.1 Gas phase study

System memory effect   The study of ammonia formation from nitrogen-hydrogen plasma was performed in the newly built setup described in section 2.2.1.1 with the purpose of avoiding the memory effect of conventional SS UHV chambers where the ammonia molecules are trapped on the walls. For that, investigating this memory effect of the new system (i.e. its storage over the time for NH$_3$) was the first measure carried out via two sets of experiments. NH$_3$ gas was first introduced in the system at a fixed pressure of 5×10^{-3} mbar (a pressure that will be shown later to correspond to the highest ammonia produced in the system). The gas was then fully pumped and RGA spectra were recorded during the full process. Figure 2.9a shows the RGA current intensity variation for the major ammonia peak at 17 amu. As can be seen, the full pumping of NH$_3$ from the gas phase takes a few seconds. However, this does not indicate a complete removal of ammonia from the vacuum chamber but only in the gas phase as long as a possible residual part of ammonia can be sticking to the walls. Therefore, a second experiment was performed consisting of degassing the ammonia by an Ar plasma. Figure 2.9b shows the start of the ammonia degassing process by the impact of Ar atoms from the gas phase already before starting the plasma. When the Ar plasma was then ignited, an ammonia peak reaches its highest values at 1.4×10^{-11} Amps, a value that represents 3 % from the initially introduced ammonia.

The peak was then continuously decreasing and the NH_3 was almost fully removed in less than 10 min indicating therefore that the system storage is very low and the degassing of the residual ammonia can be performed through an argon plasma.
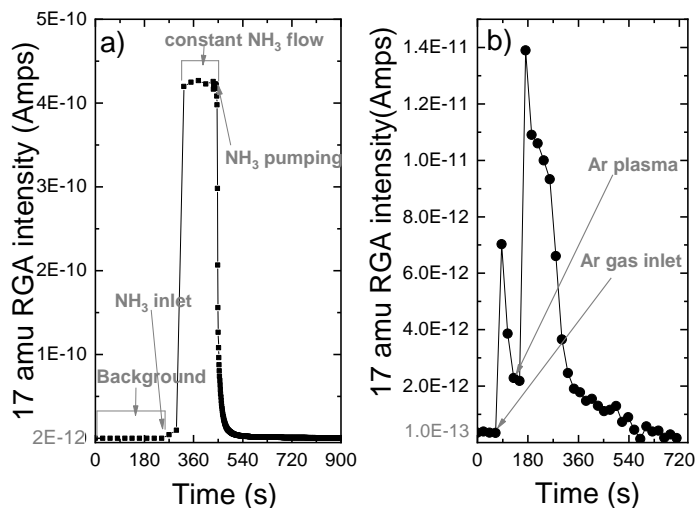

Figure 2.9: *Time evolution of the major ammonia peak at 17 amu following a) NH_3 inlet and pumping b) Ar gas inlet and plasma ignition*

Conditioning procedure A wall conditioning step was carried out before each experiment consisting of cleaning of the quartz tube wall as well as the sample surface with pure Ar RF plasma at 120 W and 5×10^{-3} mbar for two hours. Inert Ar gas has in fact the advantage of cleaning organic contamination from the surface without causing a chemical reaction or oxidation. As the sample is floating its potential is set by the plasma potential (V_P). The floating potential (V_F) is defined by V_P-V_F = 5 kTe so that ions are accelerated with 15 eV on the samples (with measured kTe=3 eV [51]).

Figure 2.10 shows the RGA spectra recorded at the beginning and the end of the Ar plasma cleaning procedure. As can be seen, the two hours Ar plasma completely removes hydrocarbons and carbon dioxide contaminants. Besides, more than 80 % of the initial water intensity was removed. Although during the process the water intensity represents less than 2 % of the total gas mixture, the peak will be taken into account during the deconvolution of the RGA measurements.

Note that the contaminants and specifically water molecules were removed from the surface not only by Ar atoms sputtering but also by thermal effect i.e. after 2 hours the measured temperature of the outer tube was around 90 degree promoting, therefore, the desorption of impurities from the surface.

An additional precaution to avoid the sample surface contamination consists of placing an alumina tube inside the surfatron plasma source to prevent the SiO_2 (from the tube wall) etching and redeposition on the W (an effect that we have observed for a long exposure to hydrogen plasma). The alumina tube was therefore used in this purpose to bypass the plasma-silica surface interaction in the most energetic place of the discharge. This inserted Al_2O_3 surface was verified to not affect the ammonia pro-

duction results by performing an NH$_3$ formation experiment with and without adding the tube. Furthermore, all the W samples were analyzed by XPS after the experiments to confirm the absence of silicon on the surface.
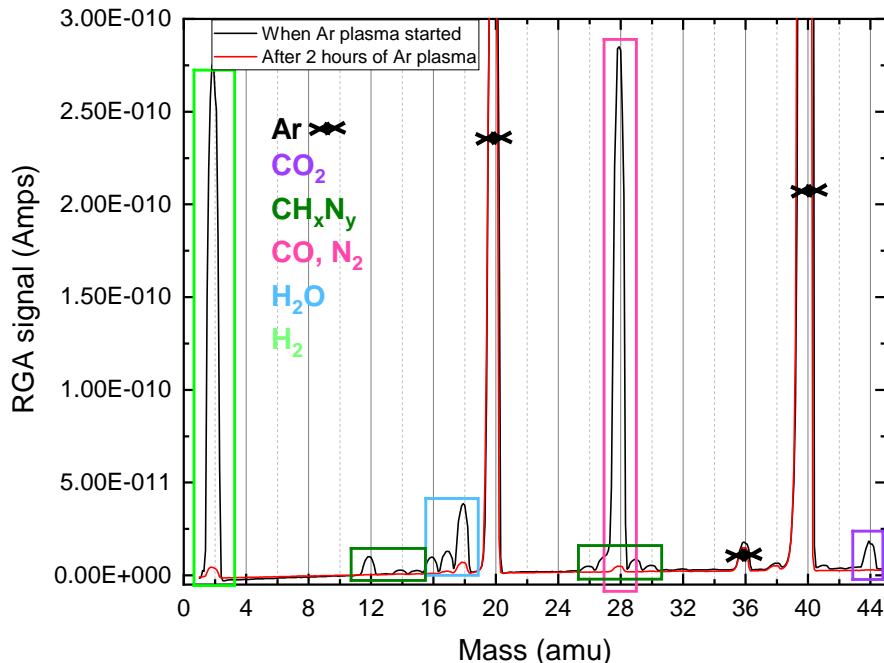

Figure 2.10: *RGA spectra recorded at the beginning and the end of the Ar plasma cleaning procedure identifying the major impurities*

RGA calibrations   After the cleaning step, an RGA calibration was performed. It consists in determining the cracking patterns and the calibration factors for the different plasma species (N$_2$, H$_2$, NH$_3$ and H$_2$O). Electron impact ionization of a gas creates an array of ion fragments that make up the RGA spectra. The ratio between the major peak intensity and the other fragments intensity is referred to as the cracking pattern. As an example, the NH$_3$ molecule presents four peaks in the RGA spectra: the main one at 17 amu for NH$_3^+$, one peak at 16 amu for NH$_2^+$, one at 15 amu for NH$^+$ and the last at 14 amu for N$^+$. The relative intensity of the different peaks for a given mass to charge ratio (m/q) constitutes the ammonia CP. Although the ratio of the peak heights in the cracking patterns can be found in tables of standard spectra, quantitative analysis of mixed gases generally requires accurate calibration of the cracking patterns (ionization energy, but also on details of the individual instruments) with pure gases. Therefore pure N$_2$, H$_2$, NH$_3$ and H$_2$O (introduced through a leak valve to the system) were injected separately in the quartz tube and their CPs were determined and summarized in table 2.3. By varying the pure gas pressure, CPs were verified not to depend on the pressure.

Calibration factor, on the other hand, represents the sensitivity of the RGA to a specific gas. It is, in fact, the proportionality factor of the measured detected current and the known partial pressure. A similar calibration procedure was reported by

Table 2.3: *Cracking patterns (CPs) of nitrogen, hydrogen, ammonia and water*

	1	14	15	16	17	18	28
H_2	1						
N_2		0.05					1
NH_3		0.01	0.05	0.77	1		
H_2O				0.04	0.26	1	

Malyshev and Middleman [52] and other [53–55]. Each gas CF was determined by relating the output current of the RGA to the known pressure of the gas measured by Baratron which is a capacitance manometer delivering direct absolute and gas independent measurement of pressure. CF of N_2, H_2 and NH_3 were extracted by introducing a controlled mixture of the three gases at known partial pressures. The choice of mixing the three gases together rather than introducing pure gases is justified by the detected change in the calibration factor when measuring pure gases or mixtures. This effect is probably resulting from the change in the preferential ionization of one gas over another when mixed together. Only the CF of H_2O was determined for pure gas because of its high reactivity with NH_3 to form NH_4^+ (through acid-base reaction) that can contaminate the system. Besides, the water peak contributes less than 2 % to the total pressure and its presence is assumed not to affect the other species CFs. Moreover, CF and CP calibration are performed before each experiment as the aging of the RGA filament can affect these values.

Formation process   Following the calibration step, the experiment was conducted by introducing nitrogen and hydrogen at different N_2/H_2 ratios set as:

$$\frac{[N_2]}{[N_2] + [H_2]} = 1, 2, 5, 10, 25, 50, 80\% \tag{2.1}$$

and constant total pressure (2×10^{-2} mbar) in the reaction chamber using mass flow controllers. (For a constant ratio of N_2/H_2, the NH_3 production was verified not to depend on the total pressure (see chapter 3))

The plasma was then ignited for 5 to 10 min when no W sample was introduced in the tube and for 15 min in the presence of the sample. The choice of this time duration will be explained later in the results section. The discharge zone is located in the quartz tube and the plasma is not in contact with any metallic surface before reaching the RGA head. All experiments were performed at room temperature (RT) and no additional heating was used for all experiments presented here although a temperature increase of about 20 °C was measured only due to the thermal energy of the plasma. The nitrogen-hydrogen plasma can heat up the surfaces in contact with (including reactor wall and W sample) by the impact of charge carriers, photons, metastable and excited neutrals, and fast ground-state neutrals [45], as well as through ammonia synthesis exothermic surface reactions. Product gases resulting from N_2/H_2 plasma were analyzed continuously and spectra recorded every twenty seconds. All

experiments were repeated at least twice and a reference experiment for an initial N$_2$ concentration of 10 % is repeated after each full cycle to ensure that the status of the W surface does not change over time. An example of an RGA spectrum resulting from a N$_2$/H$_2$ plasma is presented in Figure 2.11. The spectrum shows the main peaks identified during the plasma which are nitrogen, hydrogen, produced ammonia and small residual water peak.
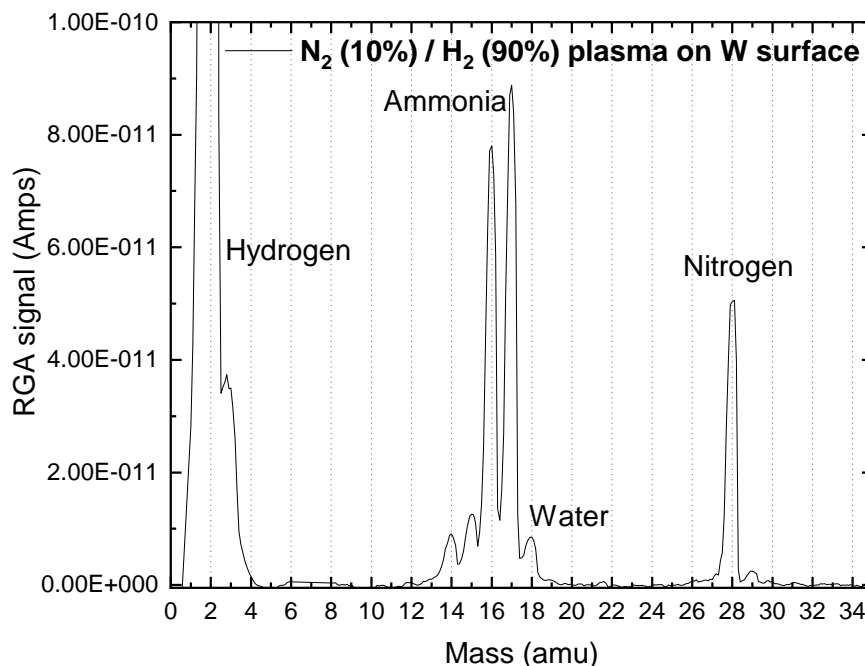

Figure 2.11: *RGA spectrum recorded during the N$_2$/H$_2$ plasma identifying the presence of residual water, nitrogen, hydrogen and formed ammonia*

Results analysis   For the deconvolution of the measured spectra, a python code that takes into account the different compound CP and CF was employed. The concentrations of the different species are derived by fitting the height of the measured peaks to the sum of the cracking patterns of the species and the RGA currents are converted back to partial pressures using the CF of each present specie.

2.2.3.2 Surface study

In order to study and follow the formation mechanism of ammonia on a W surface, chemical analyses using XPS were performed to identify surface species formed after hydrogen and/or nitrogen plasma. Three different experiments were performed as follow: the exposure of a tungsten coated surface to N$_2$/H$_2$ plasma, then an exposure to pure N$_2$ followed by pure H$_2$ plasma and finally the exposure to pure H$_2$ followed by N$_2$ plasma. For each step, a new fresh 20-nm tungsten film was deposited on silicon wafer by means of pulsed-DC magnetron sputtering of a 99.95 % pure W target.

Both magnetron sputtering and nitrogen and/or hydrogen plasma exposure were performed in a stainless steel high vacuum system (Figure 2.6) with 5×10^{-8} mbar

background pressure obtained using conventional pumping systems enhanced by a liquid nitrogen trap for selective trapping of residual gas. 20 nm of tungsten film were deposited by means of pulsed-DC (50 kHz, 496 ns) magnetron sputtering operated at 100 W using Ar as a process gas at a working pressure set to 1×10^{-2} mbar. Following the deposition, the grounded W samples were exposed for 20 min to a N_2 and/or H_2 plasma generated with an external surfatron plasma source at a fixed total pressure of 1.2×10^{-2} mbar.

Without breaking the vacuum, samples were transferred to an ultra-high vacuum chamber for XPS analysis. The typical time required for the sample transfer (i.e. the time between the plasma is stopped and the measurement start) is around 15 to 30 min.

The fitting procedure of the core level lines was described by B. Eren et al [56]. It was performed, using the UNIFIT software (Version 2016) [57], by Doniach-Sunjic functions [58] after a Shirley background subtraction [59]. The individual peaks were fitted as a convolution of a Lorentzian and Gaussian function. The intensities were then estimated by calculating the integral of each peak and the atomic concentrations were extracted using Scofield sensitivity factors [60].

2.3 Results

2.3.1 Tungsten surface catalytic effect on ammonia formation studied by RGA in the metal free setup

2.3.1.1 Ammonia formation with and without catalyst

In order to investigate the effect of the W and SS surfaces on the ammonia formation, produced NH_3 from N_2/H_2 plasma was quantified without catalyst (i.e plasma ignited in the empty quartz tube) and when a W or SS surface was loaded in the furnace zone. Prior to the plasma ignition, no ammonia was observed to be produced through gas cracking in RGA in a N_2/H_2 gas mixture. Therefore the measured ammonia peak results only from the plasma and the plasma-surface interactions.
In Figure 2.12 is plotted the ammonia percentage (defined as the ratio between its partial pressure and the total pressure during the plasma) against the nitrogen initial fraction without and with a catalyst (W and SS). All experiments were repeated at least twice and the error bars presented in this figure represent the standard deviation of the measurements.
For an increasing N_2 fraction and without catalyst, the ammonia production increases up to 6 % for an initial N_2 fraction of 25 % that corresponds to the stoichiometric composition of nitrogen in ammonia. By introducing a catalytic surface, we noticed an increase of the NH_3 production up to 20 and 24 % for SS and W, respectively and shift of these values to higher N_2 initial fraction (Figure 2.12).

As can be seen, without the presence of a metallic catalytic surface, the ammonia can be formed. It is still not clear if the production occurs in the plasma volume or on the quartz wall of the vacuum chamber. Based on previous studies [48, 61–63],

Hong et al. [64], summarized that ammonia can be produced in atmospheric pressure by three-body reactions between NH$_x$ radicals (produced themselves by reactions between dissociated atoms and excited molecules) in the plasma phase. In a glow discharge microwave plasma, Uyama et al. [65,66], stated the role of the volume reaction between NH radicals formed in the plasma volume and H$_2$ molecules on the ammonia formation. Recently, chemical kinetics modeling studies [47,48] revealed that the gas phase volume reactions alone are not able to produce ammonia in detectable amounts. Taking these results and our measurements into account, we can attribute the production of ammonia without catalyst to either production in the plasma volume or recombination of dissociated species in the plasma on the quartz tube. The recombinations in the RGA chamber (where the pressure during the process is in the range of 5×10^{-6} mbar) were neglected as the calculated mean free path is approximately equal to 50 m indicating a very low probability of species to recombine during the measurements.
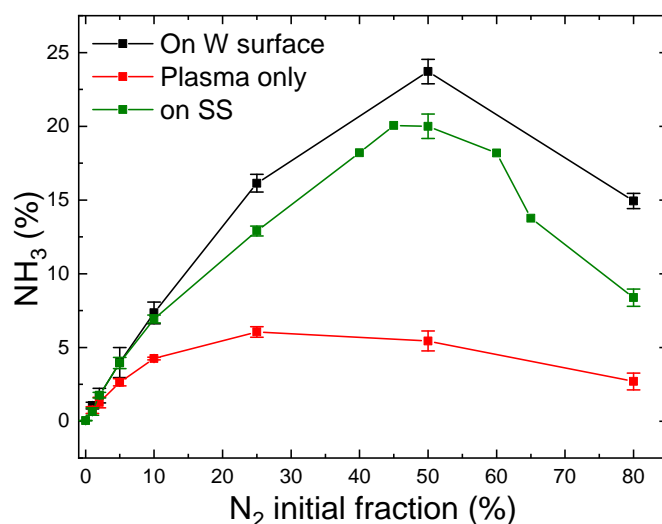
Figure 2.12: *Ammonia production without catalyst (red curve) and with W catalyst (black curve) at RT for different N$_2$ initial fractions*

When W and SS catalytic surfaces were loaded, the ammonia production highly increased. This was also reported in the PhD thesis of Patil [67] who studied the effect of Al$_2$O$_3$ supported metals and metal oxide catalysts on the ammonia formation in a DBD reactor. He showed that, with the presence of a catalytic surface, the ammonia production is around 3 times higher compared to the blank experiment where no surface is loaded in the quartz tube. In a more recent study, Shah et al [47] investigated the ammonia formation in an RF quartz plasma reactor and showed that the insertion of metal meshes catalysts in the quartz reactor highly increased the yield, in particular, on Au surface when 300 W of RF power was applied (5 times higher ammonia yield than without catalyst).

By comparing the performance of both catalysts towards NH$_3$ synthesis shown in Figure 2.12, we can see that the tungsten surface acts as a better catalytic surface than SS for nitrogen initial fractions above 10 %. This finding was quite unexpected as the

SS surface contains predominantly iron (around 70 % of the total composition), known as the best catalyst for ammonia synthesis under thermal condition (see volcano plot in [68]). This can be explained by the existence of other metals like chromium (16 %) in the SS which have lower activity than the Fe [69] or the presence of a native oxide layer. In fact, for SS, the surface is covered with a chromium oxide film that passivates the surface of the steel. This Cr_2O_3 oxide has typically few nanometers thickness [70] and it is not clear, for our case, if the argon plasma cleaning is removing the oxide as the sample is floating and if the hydrogen/nitrogen plasma is reducing the oxide layer to have an iron catalyst. Another factor that could also explain this difference between W and SS catalysts is the plasma effect on the catalytic activities of surfaces. In fact, Mehta et al. [71] showed, experimentally and through a micro-kinetic model, that the nitrogen excitation in the plasma changes the catalytic activity trends from those known in thermal catalysis.

Figure 2.12 revealed also a difference concerning the nitrogen fraction for which the ammonia production reaches its maximum. Without catalyst, the maximum production corresponds to the stoichiometric mixture of nitrogen hydrogen (25/75 % of N_2/H_2). This was also observed in a N_2/H_2 microwave discharge in a Pyrex tube by Uyama and Matsumoto [72] and in a DC glow discharge by Amorim et al. [73]. However, when a catalytic surface was introduced the maximum production shifts from the stoichiometry to higher nitrogen content. Although the exact reason is still not clear, this shift was reported in several papers [49, 71, 74–76]. In particular, in Body et al recent paper, using their RF helicon source plasma device that operates at 500 W of RF applied power, 1.3×10^{-2} mbar of gas pressure, and stainless steel as a material target, their results reveal the highest ammonia peak at a nitrogen content of 40 % ± 5 % (instead of 25 %). Besides, based on their volume-averaged computational model, the result also confirms the shift to a lower nitrogen content (44 % ± 1 %) for the highest ammonia production. This shift could be explained by a possible mechanism of ammonia formation on the surface where only nitrogen adsorbs onto the surface and reacts with the hydrogen from the gas phase. In this process, higher coverage of the adsorbed nitrogen as well as a higher pressure of the hydrogen gas yields a higher reaction rate. That would correspond to an equal nitrogen and hydrogen initial concentrations in the mixture, i.e. 50 % of N_2 and 50 % of H_2 (more details are in section 2.3.2).

2.3.1.2 W surface effect on the nitrogen cracking efficiency and the ammonia formation yield

In order to gain a better understanding of the surface catalytic effect on the ammonia synthesis, the evolution of two relevant parameters including the nitrogen cracking efficiency and the ammonia formation yield was investigated on the W surface. Nitrogen cracking efficiency is defined as the fraction of nitrogen molecules that are depleted from the gas phase during the plasma and can be written as:

$$Cracking\ efficiency = 100 \times \frac{\%N_2(gas) - \%N_2(plasma)}{\%N_2(gas)} \quad (2.2)$$

where % N$_2$ (gas) is the initial introduced nitrogen fraction and % N$_2$ (plasma) is the ratio of the nitrogen partial pressure from the total pressure during the plasma (calculated after peaks deconvolution by the python code).

The ammonia formation yield is on the other hand defined as the percentage of initial injected nitrogen molecules that converted to ammonia:

$$Formation\ yield = 100 \times \frac{\%NH_3(plasma)}{2 \times \%N_2(gas)} \tag{2.3}$$

The % NH$_3$ which represents the percentage of ammonia formed is calculated itself as the ratio of ammonia partial pressure from the total pressure during the plasma and the factor 2 in the denominator comes from the fact that one N$_2$ molecule, after cracking, can form two NH$_3$ molecules.

In thermal processes [47] as well as in atmospheric-pressure plasmas [64], the critical elementary step for ammonia formation is the N$_2$ triple bond dissociation as it presents a large free energy of activation (9.8 eV). The role of a catalyst is to decrease this activation energy and support the dissociative adsorption of nitrogen molecules. By comparing the nitrogen cracking efficiency without catalyst and on W surface, the influence of the surface in our low pressure plasma conditions regarding the nitrogen dissociation can be identified.

Both nitrogen cracking efficiency and ammonia formation yield are plotted in Figure 2.13 for different nitrogen initial fraction. As can be seen, the trend of the cracking efficiency curve does not change when introducing a W catalyst but the values are slightly increased. This indicates that the W surface either dissociates a part of non-cracked nitrogen from the plasma or the increase is only due to the surface consumption of nitrogen molecules or atoms. In fact, the cracking efficiency is not a direct measurement of dissociated nitrogen molecules but a parameter that presents the missing N$_2$ molecules in the plasma compared to the gas phase including therefore the dissociated molecules but also adsorbed molecules on the surface. The high cracking efficiencies in plasma only (red curve) suggest then that the plasma dissociated the precursor molecules already before they come in contact with a surface. Hong et al [64] reported that, in low-pressure plasmas (typically operating at pressures in the range from 1×10^{-2} mbar to several mbar), the dissociation of the gaseous precursors is provided by the energetic plasma environment so that the surfaces surrounding the plasma are bombarded with dissociated species. The direct adsorption of atoms is, therefore, the dominant process. Particularly, nitrogen molecules are dissociated in the gas phase through the reaction of ionized molecule in the plasma with electrons

$(e^- + N_2^+ \longrightarrow 2N)$.

The dissociation of the nitrogen triple bond (that requires 9.8 eV of energy) can be also caused by the photons emitted by the excited hydrogen in the plasma and specifically by the Lyman-alpha series lines at 121.6 nm (corresponding to 10.2 eV).
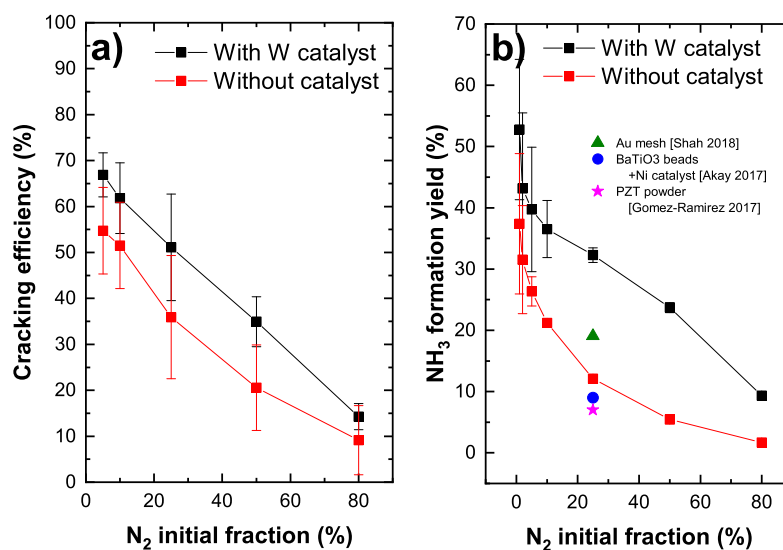
Figure 2.13: *a) Nitrogen cracking efficiency and b) ammonia formation yield for different N_2 initial fractions (with added data points from previous studies [47, 77, 78])*

The decrease of the cracking efficiency with increasing N_2 fraction, both with and without catalyst, can be explained by the increase of the recombination rate of cracked nitrogen atoms to form back N_2 molecules for a higher nitrogen density in the plasma. Another possible reason of this decrease can be a molecular assisted recombination process of nitrogen molecules in the presence of hydrogen. This process is proposed by Perillo et al [79] through a numerical simulation study of the nitrogen recombination mechanisms in N_2/H_2 plasma. One of the possible mechanisms they presented (specifically for the plasma edge) have the following reaction paths:

$$H_2^+ \; + \; N_2 \longrightarrow N_2H^+ + H$$
$$e^- \; + \; N_2H^+ \longrightarrow N_2 + H$$
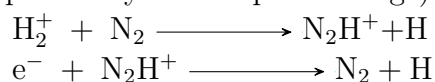
Concerning the formation yield, the catalyst seems to have a great impact on this parameter. The ammonia yield increases from 12 % (no catalyst) to 32 % (W) and from 5 % to 24 % for 25 and 50 % of N_2, respectively. This allowed us to obtain unprecedented ammonia formation yield, surpassing the yield reported in the literature. In fact, in their recent publications, Hong et al [64] and Shah et al [47] reviewed the literature and provided tables summarizing the ammonia yields for plasma-assisted ammonia synthesis in various types of plasma sources operating at atmospheric pressure, such as dielectric barrier discharges (DBDs), pulsed and AC plasmas and at low pressure such as RF plasma discharges. They demonstrated that the ammonia yield of plasma catalytic ammonia synthesis is in the range of 0.1 to 19 %. The highest value corresponds to the production of ammonia on gold mesh catalyst in working conditions of 400 °C of reaction temperature, 0.35 mbar of pressure and 300 W of RF plasma discharge.

In order to compare with Haber-Bosch process, the energy yield in g-NH_3/h was calculated. For 120 W of input power, a yield of 0.1 g/h was obtained (only the plasma input power was considered here and the power consumed by vacuum pumps

and other electronic devices are neglected for simplification reasons). The Haber Bosch process, on the other hand, consumes an energy value around 12 MWh/ton of ammonia which corresponds to 1.2 W of power for 0.1 g/h, 100 times lower than in our process. Therefore, despite the high ammonia formation yields achieved through RF plasma catalysis in this study, the values for energy yield are still very limited compared to the commercial Haber-Bosch process. With optimization of the plasma parameters as well as the catalytic surface, it is expected that substantial improvements of the energy yield will be possible for this process.

2.3.1.3 Relating ammonia formation to surface nitrides
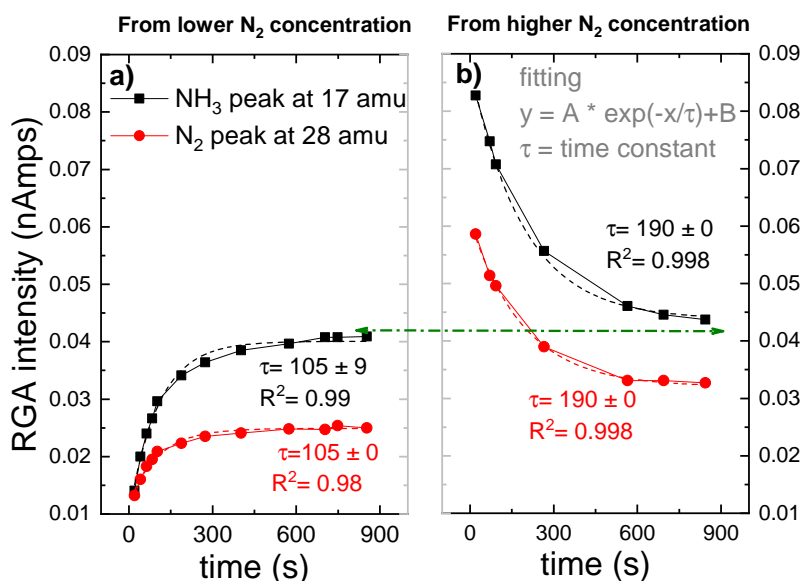
Figure 2.14: *Time evolution of the RGA peak intensities relative to NH_3 (at 17 amu) and N_2 (at 28 amu) for 5% of N_2 initial fraction*

Figure 2.14 shows both ammonia and nitrogen RGA peak intensities at 17 and 28 amu resulting from an N_2/H_2 plasma with a 5 % of nitrogen initial composition. On the left curve, the W surface was in the previous run exposed to a hydrogen-nitrogen plasma with a 2/98 % of nitrogen-hydrogen initial concentrations while in the right curve the surface was exposed to 80/20% of N_2/H_2. The purpose of this experiment is to verify the impact of surface pre-loading with nitrogen on the ammonia formation. All curves were fitted with an exponential decay function (a typical fitting function for asymptotic evolution) and the time constants were extracted.

RGA peak intensities reflect an indirect measurement of species on the surface by detecting desorbed species from the surface to the gas phase or missing species from the gas phase which get consumed by the W surface. In the Figure 2.14 ammonia peak RGA intensities represent the NH_3 produced in the plasma volume (or eventually on the quartz tube as discussed in the previous section) and also the ammonia that gets desorbed after being formed on the W surface. However, the nitrogen RGA intensities

represent an indirect measurement of the nitrogen consumed or released by the W surface. When comparing both figures a) and b) the ammonia peak followed the same trend as the nitrogen peak, saturating both with the same time constant. This observation indicates that the ammonia formation is directly related to the nitrogen adsorbed or released from the surface i.e NH$_3$ forms through surface nitrides steps. This mechanism will be developed in the following section. After reaching the saturation (either by loading the surface with nitrogen or desorbing residual nitrogen from the preloaded surface), the ammonia peak has a similar value indicating that ammonia formation is not dependent on the initial state of the surface. However, both nitrogen peaks saturation values do not overlap. This can be either due to the measurement time that have not been long enough to reach the equilibrium of both signals or to a partial diffusion of the nitrogen inside the W sample that can not be recovered. This was in fact observed by Oberkofler et al [17], who reported that the main mechanisms for nitrogen retention in N$_2$-seeded discharge of ASDEX Upgrade Tokamak are implantation of nitrogen into plasma-facing materials, co-deposition with other species present in the Tokamak and the formation of ammonia.

2.3.2 Surface study by XPS in the conventional SS chamber

2.3.2.1 Chemical analyses

After the exposure of the W coated surfaces to N$_2$/H$_2$, N$_2$ followed by H$_2$ and H$_2$ followed by N$_2$ plasma as described in 2.2.3.2, samples were immediately transferred to the XPS chamber without breaking the vacuum. The purpose of the three processes is to identify the dominant ammonia formation mechanism on the surface (L-H or E-R). If L-H mechanism is predominant, i.e. both nitrogen and hydrogen adsorb and react on the surface, it is expected to identify the same species for both exposure: to N$_2$ then to H$_2$ or H$_2$ then to N$_2$. XPS measurements revealed the existence of 4 species on the samples: tungsten, nitrogen (for samples exposed to N$_2$ in the plasma), oxygen and carbon contaminants. Despite the use of our cold trap, the existence of carbon (less than 4 %) and oxygen (in the range of 5 to 19 %) couldn't be avoided on the surface. This can be caused by the adsorbed oxygen and carbon during the transfer of the sample from the deposition chamber to the XPS chamber (that usually takes around 15 to 30 min).

Figure 2.15 and 2.16 represent respectively the W4f and N1s core level spectra measured on the W samples before and after N$_2$ and/or H$_2$ plasma exposures. The W4f core level peaks were deconvoluted into three doublets located at 31.4 eV, 32.4 eV and 33.2 eV assigned to metallic W, WN and WN$_2$, respectively, while the N1s was decomposed into 4 singulets attributed to N, NH, NH$_2$ and NH$_3$. The binding energy (BE) values for both W and N peaks are summarized and compared to literature values in table 2.4.

W4f core level spectra, in Figure 2.15, reveals no W oxides nor oxynitrides (at 35.8 eV and 33.5 eV [80]) despite the presence of oxygen on the surface, indicating that the O is only adsorbed on the surface and not bonded to W atoms. When exposed to pure H$_2$ plasma, no changes were observed for the W4f peak from its metallic state. Yet,
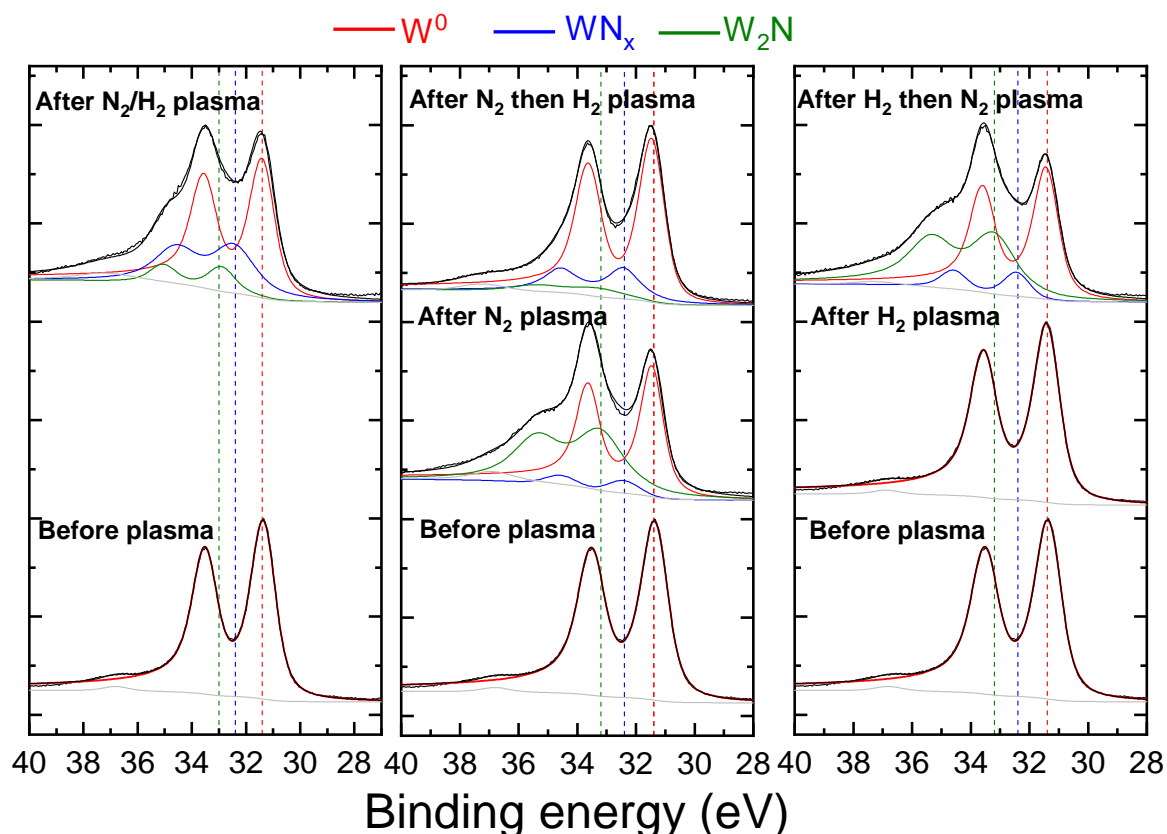
Figure 2.15: *W4f core levels spectra recorded before and after N$_2$ and/or H$_2$ plasma exposure of the W surface. The red, green and blue solid curves are the individual chemical states and the dashed vertical lines serves as an eye guide for these states. Solid black curves are the raw data and the sum curves. The graphs were shifted arbitrarily on the vertical axis to ease the view.*

tungsten nitride peaks are identified for the 4 samples exposed to N$_2$, N$_2$/H$_2$, N$_2$ then H$_2$ and H$_2$ then N$_2$ plasma. However some differences can be seen when comparing, for these samples, both tungsten nitride peaks (WN and WN$_2$) representing 2 different stoichiometry. After the exposure of the tungsten to pure N$_2$ plasma or to N$_2$ plasma following the hydrogen pure plasma, WN$_2$ peak intensity (green curves) is higher than the WN peak (blue curve) contrary to the other 2 samples.

For the same 2 samples exposed to N$_2$ only and H$_2$ then N$_2$ plasma N1s peak in Figure 2.16 present mainly 1 peak identified as nitrogen peak bonded to W. Very small peaks of NH and NH$_2$ were measured for the H$_2$ then N$_2$ plasma exposed surface. Moreover, no ammonia was detected on this sample. The NH$_3$ was in fact identified for both cases when the surface was exposed to a mixture of N$_2$ and H$_2$ and for N$_2$ then H$_2$ plasma exposure. It should be noted here that the non formation of ammonia on the sample exposed to hydrogen first then to nitrogen plasma cannot be caused by a thermal desorption of hydrogen. As Ertl addressed in [86], surface-adsorbed hydrogen can be desorbed above 200 ° C in vacuo, while for our experimental conditions, the hydrogen

Table 2.4: *W4f and N1s BE values extracted from XPS measurement on W surface. Reference values from literature and the corresponding species were added to the table.*

XPS peak	XPS BE measured (eV)	XPS BE from literature (eV)	Compound
W4f	31.3-31.4 32.4 33.2	31.2 [81] 32.3-32.4 [82,83] 33.3 [83]	W^0 WN WN_2
N1s	397.1-397.2 397.7 398.4 400.4	397.2 [84] 397.6-397.8 [80] 398.4 [85] 400.4 [80]	N NH NH_2 NH_3

nitrogen plasma heats up the W surface from RT by less than 20 °C. However, the low hydrogen retention, especially at those low energies, can not be excluded as a possible reason for the non formation of ammonia. It is also interesting to note here that the nitrogen atomic concentrations on the sample exposed to pure nitrogen plasma and on the sample exposed to hydrogen then nitrogen plasma are comparable (34 at% and 36 %, respectively). This result suggest that the pre-adsorbed hydrogen does not block the adsorption of nitrogen on the surface.

To summarize, N1s core level spectra shows that ammonia can be formed only when the surface is exposed either to a mixture of nitrogen and hydrogen or nitrogen plasma as a first step followed by hydrogen plasma. These results match to those observed by A. de Castro et al [87] who showed that deuterated ammonia was formed as a result of pure deuterium (D_2) plasma irradiation on tungsten sheet previously irradiated with pure N_2 plasma. Conversely, the symmetric experiment based on the irradiation of the tungsten wall, previously irradiated with D_2 plasma, with N_2 plasma did not show significant ammonia production. They suggested therefore that the presence of dissociated nitrogen on the W surface is the first mandatory step necessary to trigger the ammonia formation process.

2.3.2.2 Determination of ammonia formation mechanism from RGA and XPS results

Having presented experimental results from both gas phase study in the metal-free setup and surface study in the SS conventional system and reviewed from the literature the possible formation mechanism, we are able to highlight our findings concerning the dominant reaction pathway of NH_3 formation.

The results from the RGA study indicate that maximum production of ammonia on W surface is at equal nitrogen and hydrogen initial concentrations instead of stoichiometric mixture suggesting therefore that both species should be maximized in the mixture for an efficient NH_3 formation. Besides, ammonia follows the temporal evolution of nitrogen peak saturating both with the same time constant implying indirectly a connection between the ammonia formation process and the quantity of nitrogen that gets consumed by the surface.
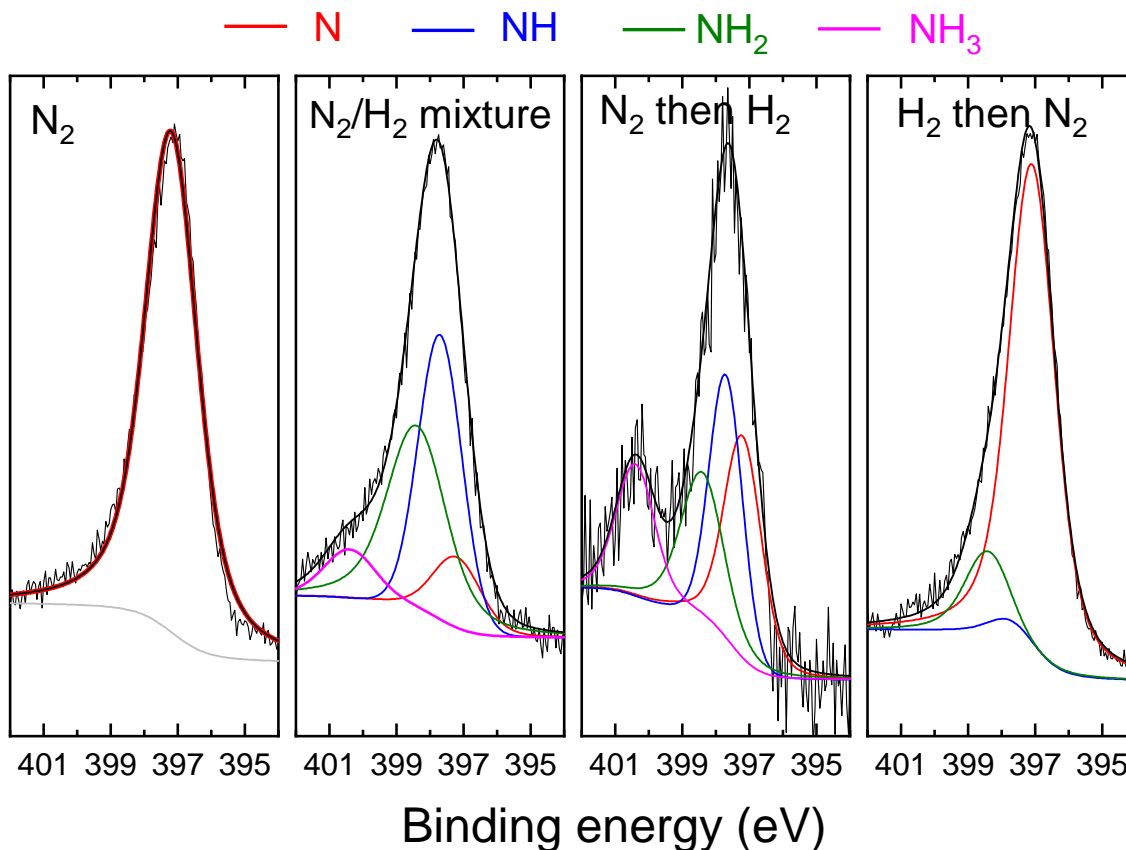
Figure 2.16: *N1s core levels spectra recorded before and after (a) N$_2$ (b) N$_2$/H$_2$ (c) N$_2$ then H$_2$ and (d) H$_2$ then N$_2$ plasma exposure of the W surface. The red, green and blue solid curves are the individual chemical states. Solid black curves are the raw data and the sum curves.*

On the other hand, XPS results show that the ammonia formation is conditioned by the presence of nitrogen on the W surface. In the experiment where the W surface is preloaded with nitrogen and then exposed to hydrogen plasma, ammonia is formed. On the contrary, when in the opposite experiment, the nitrogen is not previously present on the surface, ammonia is not formed.

On the basis of the above results, the dominant mechanism for ammonia synthesis from N$_2$/H$_2$ plasma can be identified. As explained at the beginning of this section, for L-H mechanism both nitrogen and hydrogen adsorb and react on the surface implying that the order of the exposure of the surface to pure N$_2$ and H$_2$ would not affect the results in terms of ammonia production on the surface. This was not the case for our measurement suggesting, therefore, the E-R mechanism predominantly contributed to the ammonia formation in the low pressure RF plasma. Besides, the ammonia formation was shown to be conditioned by the presence of nitrogen on the surface (either from the mixture or from the pure N$_2$ plasma) indicating that, in E-R mechanism, nitrogen gets adsorbed onto the surface and interacts with hydrogen from the gas phase (see E-R 2 in Figure 2.4). However, given that XPS measurements are restricted to

species identifications on the surface and do not consider what was formed and desorbed as compounds, the conclusions from such analyses should, therefore, be treated with considerable caution. Complementary in-situ measurement in the gas phase of formed and desorbed species are consequently needed to confirm our findings.

The NH_3 formed in this context is a result of interaction between the plasma and the catalyst. Therefore, both plasma characteristics (density, electronic temperature, excited/ionized species distribution...) and surface properties (nature, active area, roughness, temperature...) would determine the dominant mechanism for ammonia formation.

In the review of Hong et al [64], a simplified model that takes into account two parameters (the gas temperature and surface reactivity) was established to determine the conditions where L-H would be favored compared to E-R. They stated that, for low-temperature plasma catalysis and low surface reactivity, ammonia formation mainly proceed by the E-R mechanism. However, as gas and wall temperatures increase, the role of L-H interactions becomes more important. This study was performed for atmospheric pressure plasmas and to our knowledge, no general model taking into account both plasma and catalyst properties was set to conclude about the dominant ammonia reaction paths for low pressure plasma conditions. Besides, the disagreement on the dominant reaction pathways in the previous research (presented in section 2.1.4) and also in our study can be the result of the different plasma and catalyst conditions. As an example, most of the previously reported results from literature were considering an iron (Fe) surface as the catalyst and no single modeling study was interested in the W catalytic effect on the ammonia formation. In this context, to support our experimental findings, the analysis of our measurements by means of a kinetic model which takes into account our experimental conditions (plasma parameters, W surface, pressure, temperature...) is an important task for future research.

2.4 Summary

Although undesirable in the nuclear fusion reactor, ammonia formation from hydrogen nitrogen plasma by radio frequency plasma catalysis is an attractive option for an industry adapted to process as an alternative for the Haber-Bosch process.

In this chapter, we explored the formation of ammonia from an N_2/H_2 RF plasma both without and with tungsten and stainless steel catalysts for different nitrogen initial fraction. We demonstrated that the presence of the W surface as a catalyst highly increases the ammonia formed percentage by increasing mainly the formation yield and slightly the nitrogen cracking efficiency. Using a combination of RF low pressure plasma and a W surface as a catalyst, unprecedented ammonia yields up to 32 % at 25/75 % of N_2/H_2 were obtained, surpassing consequently the yields reported in the literature for different plasma discharges and different catalytic surfaces. So far, it is not clear what is the exact factor that drastically enhanced the formation yield in our experiment compared to previous research. It could be associated to the combination of different experimental conditions: low pressure, low temperature, high dissociation rate in the plasma and enhanced photo-dissociation of nitrogen by the

Lyman lines of dissociated hydrogen. However, It is worth mentioning that the energy yield is still very limited compared to Haber-Bosch process and need therefore to be highly improved. The optimization of the plasma parameters as well as the catalytic surface could lead to a better formation and energy yield.

Furthermore, by means of X-ray photo-electron spectroscopy, we could demonstrate experimentally the interaction of species from the plasma with the catalyst surface. By investigating both the tungsten and the nitrogen binding energies to identify the formed species, we proposed a formation pathway of ammonia through Eley-Rideal mechanism between adsorbed nitrogen and hydrogen from the gas phase.

Influence of temperature and noble gases addition

I N the present chapter, we demonstrate the effect of two parameters on the ammonia production from N_2/H_2 plasma including the sample temperature and He or Ar addition. The study was initially performed at room temperature (RT) for both surfaces and then for increasing temperature up to 1270 K. This highest temperature value is relevant for the ITER divertor and in particular for the divertor active areas where the plasma impact occurs [88]. The effects of helium and argon on the ammonia formation are also investigated. He will, in fact, be present in ITER as the ash of the fusion reaction. Argon, on the other hand, was identified as the best candidate for the simultaneous enhancement of core and divertor radiation [12] in the case where elevated main chamber radiation is desired as well. Although this gas is not foreseen to be used in ITER to avoid high core level contamination, the use of argon will be required in the future DEMO prototype reactor to ensure a high main plasma radiation level.

3.1 Results

3.1.1 Temperature effect

3.1.1.1 Ammonia formation at high temperature

Ammonia was in the first experiment formed from nitrogen-hydrogen plasma in the range of RT to 1273 K (setup described in 2.2.1.1). N_2/H_2 initial ratio was fixed to 1/9 and the total pressure inlet pressure of both gases to 2×10^{-2} mbar. In the absence of catalyst, the ammonia formation rate was almost constant up to 870K and then slightly decreased from 4.2 % to 2.7 % for higher temperatures. When a catalyst is used, a strong effect of T_{Surf} is observed. For both W and SS surfaces the NH_3 fraction decreases as soon as T_{Surf} is increased. Yet a clear difference can be observed between the two materials. On the SS surface, the NH_3 percentage drops drastically between

400 and 700 K and is very low for higher temperatures. For W, the effect of T_{Surf} is more gradual and the formation rate remains higher than for SS up to 1100 K, after which is does not evolve anymore.
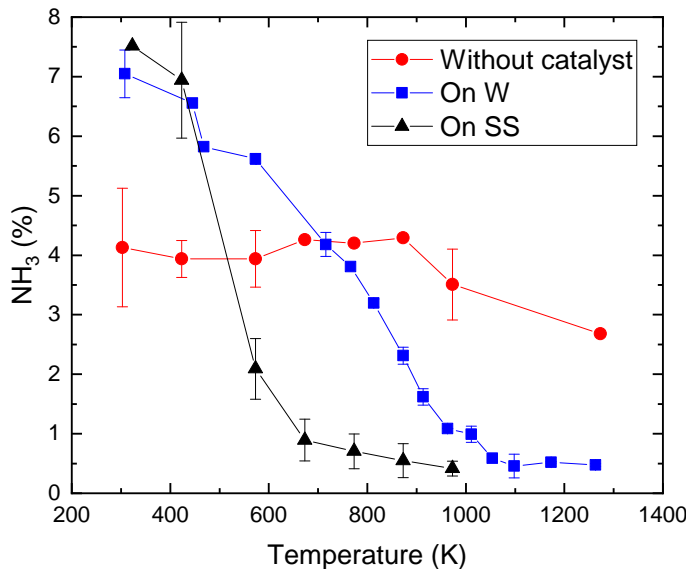
Figure 3.1: *Effect of T_{Surf} on ammonia production from N_2/H_2 plasma for different catalytic materials*

3.1.1.2 Thermal decomposition of the ammonia gas

The thermal decomposition of pure NH_3 gas without plasma was then studied as a function of temperature by flowing the ammonia gas at fixed pressure inside the quartz tube for different materials. The temperature was continuously increased up to 1273 K and the resulting peaks from the decomposition were recorded by the RGA on the other side of the tube.

Figure 3.2 shows the variation of the major RGA peaks of NH_3 (17 amu), H_2 (2 amu) and N_2 (28 amu) as a function of the temperature. Comparing the effect of the three materials, it is seen that the decomposition of ammonia into N_2 and H_2 starts at different temperatures. Without catalyst, ammonia starts to decompose into nitrogen and hydrogen at 970 K. The decomposition was partial under these conditions even for the highest measured temperature and only 23 % of the initial amount was decomposed. On the W surface, decomposition was initiated at a lower temperature of around 830 K. For temperatures between 830 and 1023 K, the ammonia peak intensity drops drastically while simultaneously both nitrogen and hydrogen peaks rise to near their maximum values. The SS surface, on the other hand, seems to be more efficient towards the NH_3 decomposition which started at lower temperature than W (650 vs 830 K). As can be observed, ammonia thermal decomposition to nitrogen and hydrogen exhibit a particular trend on this surface. Remarkably, the 17 amu peak of NH_3 slightly decreases from 650 to 900 K followed by the release of only hydrogen (no nitrogen), increases

back from 900 to 1050 K and decreases with a faster rate for a higher temperature values. The N_2 release increase is shifted to a higher temperature above 1050 K.
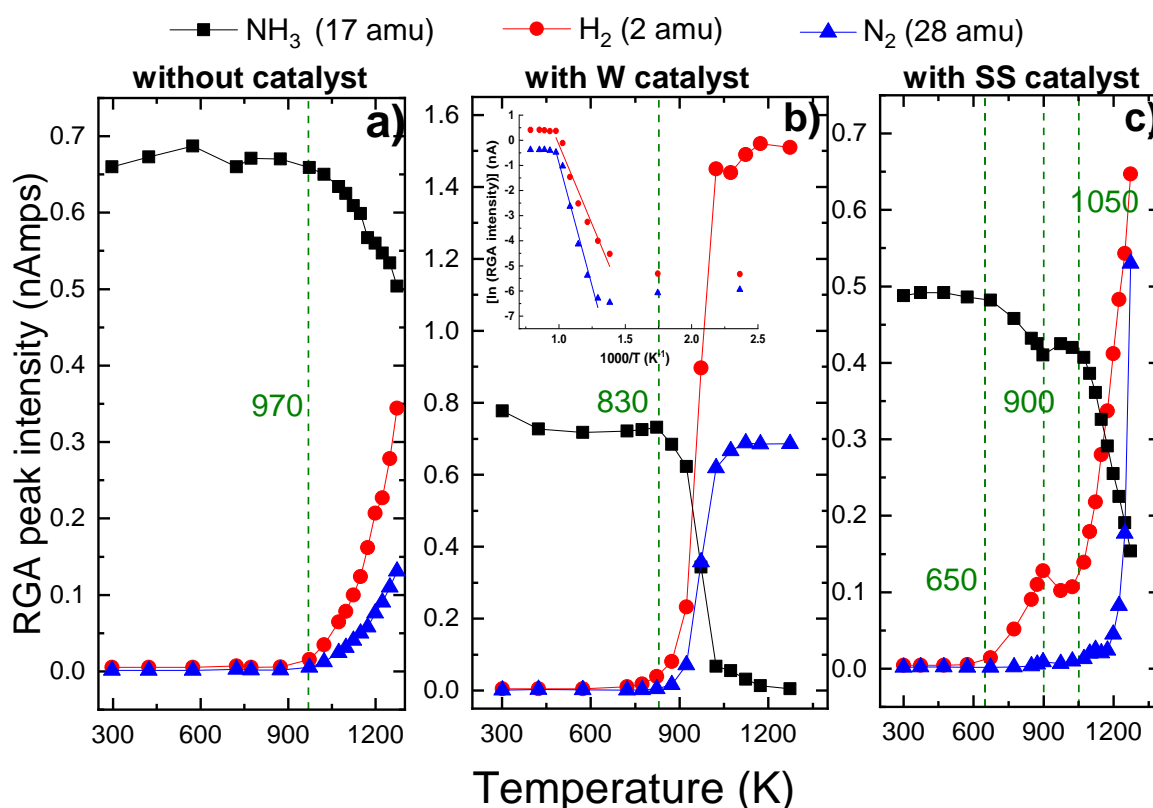
Figure 3.2: *Variation of the RGA peak intensities of the H_2, NH_3 and N_2 at 2, 17 and 28 amu respectively due to the ammonia thermal decomposition a) without catalyst b) on W surface and c) on SS surface. The inset of b) represents the logarithm of H_2 and N_2 peak intensities plotted versus inverse temperature values.*

3.1.1.3 Chemical species formed on the surface after plasma exposure: XPS studies

After plasma exposure in another conventional SS vacuum chamber (described in 2.2.1.2), chemical analyses were performed in vacuo by XPS.

Four elements were identified by XPS on the W plasma exposed samples: tungsten, nitrogen as well as oxygen and carbon contaminants. Despite the use of our cold liquid nitrogen (LN_2) trap, the presence of oxygen (3 to 9 atomic percent concentration (at.%)) and carbon (around 2 at.%) could not be avoided. These species are typically adsorbed during the time required for the transfer to the XPS chamber and or during the cool down of the sample (maximum 30 min).

Figure 3.3 represents the N1s core level spectra measured after N_2/H_2 plasma exposures of the W surface at three different temperatures. The total nitrogen atomic concentration on the surface as well as its decomposition fraction into N/NH (at

397.6 eV), NH_2 (at 398.5 eV) and NH_3 (at 400.4 eV) are presented. The total relative error on each concentration value was assumed to be 15% according to previous literature report [89].

Comparing the evolution of the three peaks for increasing T_{surf}, it can be observed that both NH_3 and NH_2 peaks drop drastically from 11 to 1 at.% and 28 to 9 at.%, respectively while the N/NH peak rises up to 90 at.% from the total nitrogen peak on the surface. W4f core level spectra of the exposed W sample to N_2/H_2 plasma show also a nitride formation (WN and WN_2). The spectrum was presented in Figure 6 of our last paper [90].
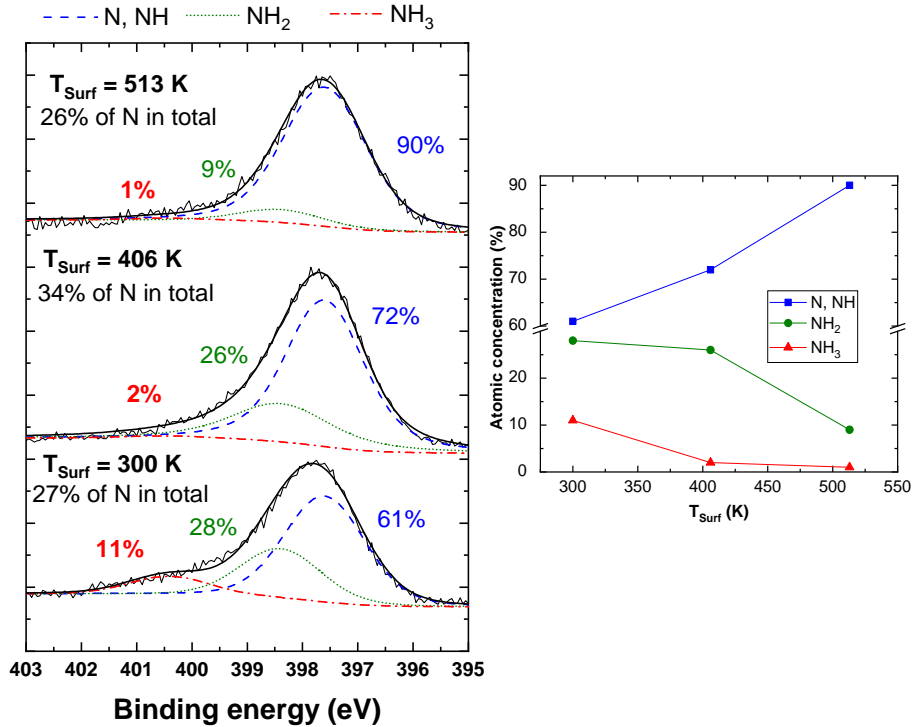
Figure 3.3: *(Left) N1s core levels spectra recorded after N_2/H_2 plasma exposure of the W surface at 300, 406 and 513 K. The red (dashdotted), green (shortly dotted) and blue (dashed) curves are the individual chemical states. Solid black curves are the raw data and the sum curves. (Right) Relative N, NH, NH_2 and NH_3 atomic concentration as a function of T_{Surf}*

3.1.2 Influence of Ar and He addition

3.1.2.1 Influence of Ar and He addition ammonia formation

In order to investigate the effect of noble gases addition on the ammonia formation, He or Ar gas was mixed with N_2 and H_2 at a fixed P_{tot} (2×10^{-2} mbar) and fixed X_{N_2}/X_{H_2} (1/9). As P_{tot} of the three gases should be kept constant during the process, increasing the Ar or He content would imply to decrease the nitrogen and hydrogen

concentrations and as a consequence the formed ammonia. One way to correct this effect can be achieved by normalizing the NH_3 formed amount to the initial N_2+H_2 content from P_{tot}. This normalization is valid if the ammonia formation would only depend on X_{N_2}/X_{H_2} and not on their pressure. To validate this assumption, an experiment devoted to study the influence of P_{tot} on ammonia formation was conducted by keeping the X_{N_2}/X_{H_2} constant and increasing their partial pressure. Figure 3.4a shows a nearly constant formation of ammonia for a $P_{tot}= P_{N_2}+P_{H_2}$ varied between 1×10^{-2} and 5×10^{-2} mbar allowing therefore to study the Ar and He effects using the above-mentioned approach.
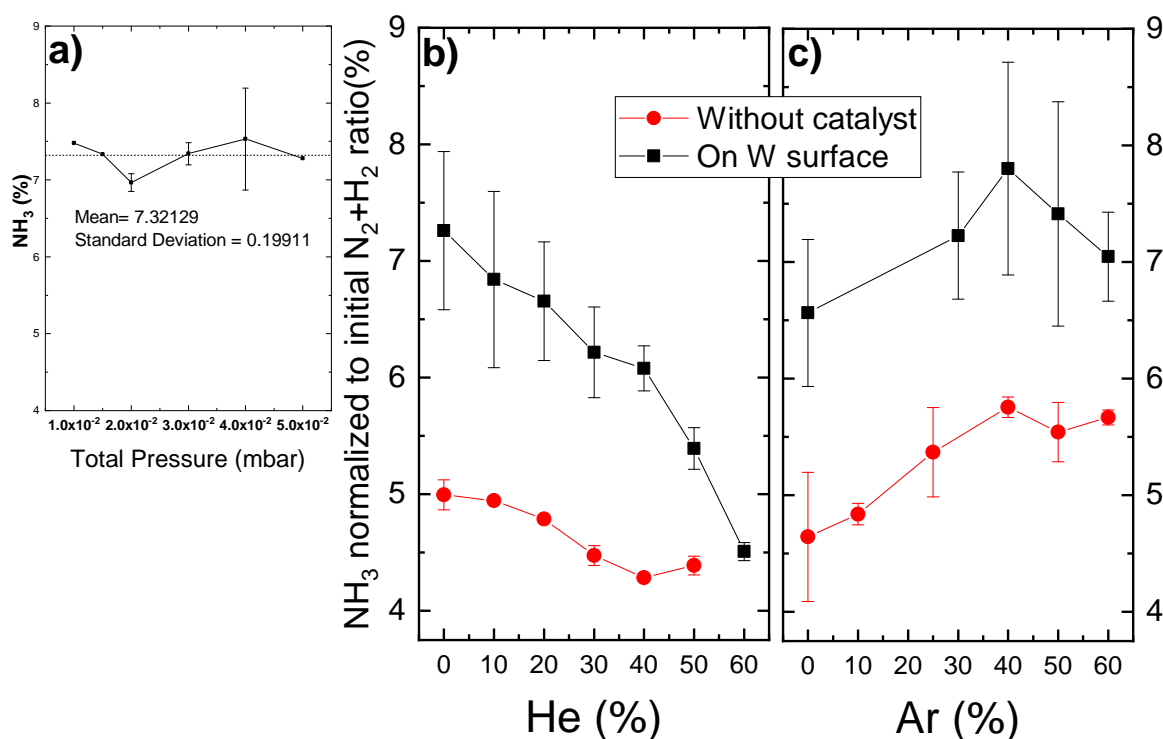
Figure 3.4: *Impact of the a) gas total pressure b) helium admixture and c) argon admixture on the ammonia production*

Ammonia production results without catalyst and on W surface are presented in Figure 3.4b and Figure 3.4c for several He and Ar percentages up to 60 %. For instance, the highest introduced argon or helium percentage (60 %) corresponds to P_{Ar} or $P_{He} = 1.2 \times 10^{-2}$ mbar and $P_{N_2}+P_{H_2} = 8 \times 10^{-3}$ mbar while the lower noble gas inlet concentration (10 %) corresponds to $P_{N_2}+P_{H_2} = 1.8 \times 10^{-2}$ mbar.
Two opposite effects can be seen for the two noble gases. Up to 40 % of argon addition, the ammonia production slightly increases both without and wit W catalyst. Meanwhile, it decreases by increasing the He percentage in the gas mixture and in particular on the tungsten where a significant drop can be seen.
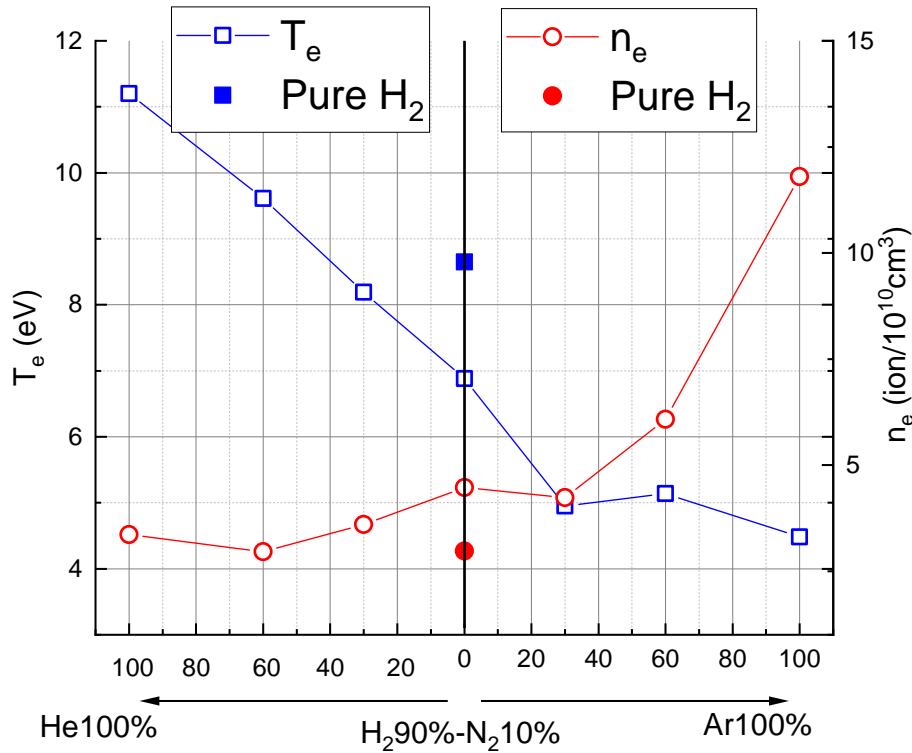
Figure 3.5: *Electron temperature T_e (blue) and density n_e (red) variation with helium and Ar percentage in the N_2/H_2 mixture. Plasma parameters (T_e and n_e) are also represented for pure hydrogen plasma*

.

The electron temperature (T_e) and electron density (n_e) are measured using a Langmuir probe for pure H_2, N_2/H_2 and several mixtures of He or $Ar/N_2/H_2$ plasmas. The results are represented in Figure 3.5. While the addition of He highly increases T_e and slightly n_e, the Ar increasing content impacts more the electron density than the electron temperature.

3.1.2.2 Influence of Ar and He addition on surface species

After the exposure at RT of several samples coated with W to N_2/H_2 + Ar or He plasma in the metallic chamber, the samples were analyzed by XPS. Measurements revealed the existence of three species on the samples: tungsten (63-69 % atomic concentration), nitrogen (28-33 at.%) and oxygen contaminants (less than 5 at.%). Figure 3.6 represents the N1s core level spectra resulting from a pure N_2/H_2 as well as $N_2/H_2/Ar$ or He plasma exposure of the surface. X_{N_2}/X_{H_2} was kept constant and 2 different fractions of the noble gases were added (20 and 50 %). In order the study the impact of lower fraction of He and Ar on the ammonia production, further experiments are required.
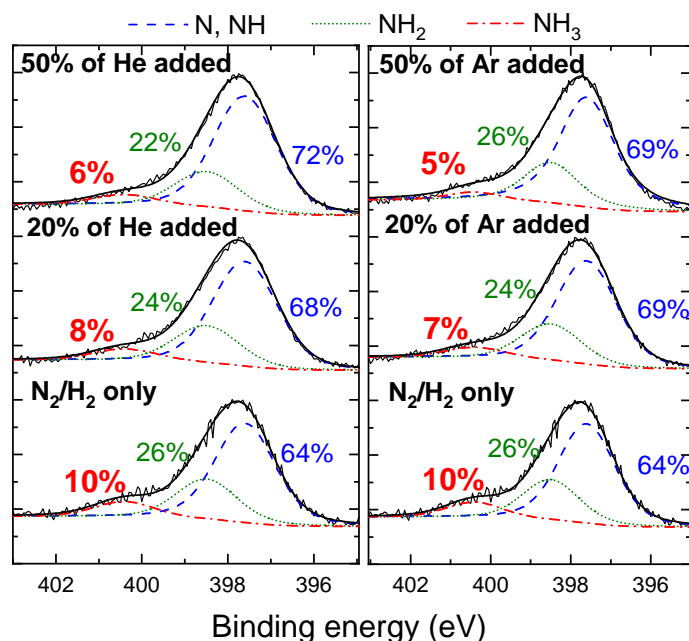
Figure 3.6: *N1s core levels spectra recorded after pure N_2/H_2 as well as $N_2/H_2/Ar$ or He plasma exposure of the W surface at RT. The red (dashdotted), green (shortly dotted) and blue (dashed) curves are the individual chemical states. Solid black curves are the raw data and the sum curves.*

N1s core level peaks were decomposed into three singulets attributed to N and NH (at 397.6 eV), NH_2 (at 398.5 eV) and NH_3 (at 400.4 eV) [80]. The existence of surface nitrides on a W exposed sample to nitrogen-hydrogen plasma was also confirmed by the W4f core level peaks presented in our previous paper (see WN and WN_2 peaks in Figure 6 of paper [90]).

The percentages shown on Figure 3.6 represent the ratio of N/NH, NH_2 and NH_3 from the total nitrogen atomic concentration on the surface. As can be seen, before the addition of the noble gas ammonia presents 10 at.% from the total nitrogen peak. This percentage decreases continuously by 40-50 % when Ar and He are added in equal ratio than nitrogen and hydrogen (50 % of the gas mixture P_{tot}). On the other hand, the N and NH ratio increased with the addition of He while NH_2 concentration decreases. However, the NH_2 peak is not affected much by Ar addition, and N/NH is not affected by further addition of Ar. It should be noted here that the nitrogen atomic concentration on the surface is almost unaffected by the addition of He (28 to 31 at.%) and Ar admixture (28 to 33 at.%).

3.2 Discussion

3.2.1 Plasma-assisted ammonia catalysis at high temperature

Unlike on SS and W surfaces, the ammonia formed without a catalyst is almost constant for an increasing the temperature up to 900 K (Figure 3.1). The decrease starts

at high temperature that corresponds to the decomposition temperature shown in Figure 3.2. This would suggest that, the quartz tube is not playing a catalytic role, as previously discussed, and that most likely the ammonia formed without the catalyst is predominantly in the plasma. The decrease of the production of NH_3 on W and SS with increasing temperature, shown in Figure 3.1, can be attributed to several causes: (i) increased desorption of N_2 as temperature is increased (ii) formation of more stable nitrides that react less with hydrogen to form ammonia (iii) ammonia thermal decomposition (iv) nitrogen continuous diffusion in the catalyst bulk leading to its decrease in the gas phase.

The first hypothesis (i) can be disproved by the XPS results in Figure 3.3. Indeed, the total nitrogen content on the surface is almost constant (in the range of 26-34 at.%) meaning that the decrease in the ammonia peak cannot be caused by a decrease in the nitrogen content on the surface with temperature. Previous studies have reported that the nitrogen release from W occurs only at high temperature in the range of 850 to 970 K [18, 91]. However, the decrease in the NH_3 and NH_2 peak and increase in the N/NH peak suggest that a surface temperature increase leads to the formation of more stable nitrides that react less with the hydrogen to form ammonia, confirming hypothesis (ii).

At high temperatures (650 K for SS and 830 K for W), the decrease in the production can be well attributed to the thermal catalytic decomposition (iii) of the formed ammonia as shown in Figure 3.2. Thermal catalytic decomposition of ammonia is known as the reverse reaction of the Haber-Bosch synthesis of ammonia, one of the most extensively researched processes over the past 150 years [92]. Upon heating, ammonia decomposes to nitrogen and hydrogen through the following reaction:
$$2NH_3 \rightleftharpoons N_2 + 3H_2$$
This reaction takes place in the gas phase, but it is strongly enhanced by the presence of a catalytic surface. Particularly over metals, the decomposition of ammonia occurs in a stepwise sequence of dehydrogenation reactions. These reactions are initiated by the adsorption of ammonia onto the active sites of the surface. The adsorbed molecules undergo then successive N–H bond cleavage, releasing hydrogen atoms that can combine to form molecular hydrogen. In the final step, nitrogen atoms recombine and desorb as molecular nitrogen [93, 94]. As shown in Figure 3.2b the ammonia decomposes with a fast rate to nitrogen and hydrogen on the W surface at 830 K. These observations are slightly different from the results of Markelj et al. [95] who studied the ammonia decomposition by flowing the gas through a hot tungsten capillary. For them, the dominant decomposition on W starts at lower temperature at about 680 K, attains the fastest increase at about 910 K and terminates around 1110 K. This discrepancy from our results could be attributed to the gas pressure difference. Previous studies [96,97] performed at high temperature and on tungsten surface showed that the ammonia decomposition rate increases with its partial pressure. While Markelj et al. introduced the NH_3 gas at 2.7×10^{-1} mbar inside the capillary, a much lower pressure of 5×10^{-3} mbar was used in our setup which could explain the temperature shift where ammonia starts to decompose. On the other hand, the complete decomposition of ammonia at high temperature as well as the activation energy (Ea) of the reaction (1.05 ±0.04 eV) are in a good agreement with their findings (1.07 ±0.08 eV). The Ea

was calculated by plotting the RGA peaks intensities in a logarithmic scale versus the inversed temperature values (known as the Arrhenius plot). The curve was then fitted linearly (as shown in the inset of Figure 3.2b))and the activation energy was extracted from the slope according to the formula R=A $\times$ exp(-Ea/k$_B$ $\times$ T) where R is the rate of the decomposition reaction, A is the pre-exponential factor, k$_B$ is the Boltzmann constant and T is the measured temperature (more details about this method can be found in [95]).

Concerning the SS surface (Figure 3.2c), the ammonia decomposition presents a particular trend. The decomposition starts at alower temperature than on W surface and the release of the nitrogen is shifted to a higher temperature values. This shift can be caused by the diffusion of the nitrogen and formation of stable nitrides with iron for temperature below 650 K (when ammonia start to decompose to nitrogen and hydrogen). This process is well known in the industry as the nitridation process where iron forms stable nitrides after exposure to ammonia at a high temperature around 870 K [94, 98]. However it has also been reported to start from temperatures as low as 570 K [68, 99]. This deactivation process is reversible at high reaction temperatures where desorption of the nitrogen takes place [94]. Note here that, the reason for ammonia peak rise between 900 K and 1050 K on the SS surface is still unknown.
The order of the activity of both catalysts (SS and W) is, therefore, reversed from ammonia synthesis to ammonia decomposition. Interestingly, even though the decomposition of ammonia is the reverse reaction of the synthesis, catalysts were shown in another study by Boisen et al. not to necessarily exhibit the same activity in both directions due to the difference in conditions and rate limiting steps [100].
It is also worth mentioning for the three thermal decomposition experiments without catalyst, on W and on SS, that ratios between ammonia peaks at 17, 16, 15 and 14 amu were constant and equal to the ammonia cracking pattern indicating therefore no release of the intermediate production of ammonia decomposition (NH$_2$ or NH) from the surface.
To sum up on the impact of temperature on ammonia production, we can conclude that the decrease is due to two major effects. For high temperatures (T$_{Surf}$¿ 650 K and 830 K for SS and W, respectively) the decrease in the production rate results from the thermal decomposition of ammonia. For lower temperature the temperature increase favor the formation of more stable nitrides that does not tend to react further with hydrogen to form NH$_2$ and NH$_3$. The possibility of a bulk diffusion of the nitrogen cannot be rejected also and further thermal desorption experiments are required to quantify the trapped nitrogen.

3.2.2 He and Ar effect

To our knowledge, only two groups [2, 24] were interested in the study of Ar and He effect on ammonia formation and there is still considerable disagreement between their results. Experiments performed in the linear plasma device (GyM), using a microwave sustained N$_2$/D$_2$ plasma, show a reduction of 80 % in the ammonia production when 17 % of He was added while the addition of 3.1 % of Ar to the hydrogen-nitrogen

mixture was almost not effective. This effect was attributed to a modification of the physical-chemical process on the surface where helium acts as a barrier for the ammonia formation by occupying the catalyst active sites. On the other hand, the other group [2] reported an increase by 45 % of the produced NH_3 for only 8 % of added He. According to them, the increased ammonia formation with the He addition does not result from a higher adsorption of active species on the surface but rather due to an enhancement of the N-H recombination induced by the helium bombardment. In both studies, the authors confirm the need for further experiments to investigate the surface state and species in order to support their explanation. In this context, surface analysis of the exposed surface to a $N_2/H_2/Ar$ or He plasma were performed in this manuscript.

When He and Ar are added to N_2/H_2, XPS measurements of the W surface (Figure 3.6) show a drop in the ammonia peak and a rise in the N/NH peak while the total surface nitrogen atomic concentration was constant. These observations indicate that the presence of the two noble gases does not inhibit the adsorption of nitrogen on the W catalyst (a key step for the ammonia formation) but is rather unfavorable for the hydrogen and nitrogen surface recombination to form NH_3 from the surface nitrides. It should be mentioned here that conclusions from XPS are restricted to species on the surface and do not consider what was formed and desorbed as compounds.

The slight increase in the ammonia production with argon addition can be explained by the generation of more active nitrogen species. Hong et al. [101] investigated this effect by adding 10 sccm of Ar to 30 sccm of N_2 and 30 sccm of H_2 feed gas stream in a dielectric-barrier discharge reactor. They observed an increase in the discharge power, uniformity and gas temperature, and those factors lead to higher ammonia production rates. The optical emission spectra also indicated an increase in N^+ possibly resulting from a reaction between Ar^+ and N_2. This increase in nitrogen dissociated atoms contributed therefore to the increase in NH_3 production. Nakajima et al. [102] further explained further this reaction between nitrogen and ionized argon as a charge transfer reaction followed by a dissociative recombination of nitrogen with an electron from the plasma:

$$N_2 \ + \ Ar^+ \xrightarrow{\hspace{2cm}} N_2^+ \ + \ Ar$$
$$N_2^+ \ + \ e^- \xrightarrow{\hspace{2cm}} N \ + \ N$$
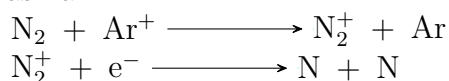
The charge transfer reaction between nitrogen and argon is favored by the fact that both species have almost the same ionization energy shown in table 3.1. However, when He is added to the mixture this reaction is not expected to occur due to the high ionization energy of helium.

A further explanation of the argon and helium effects can be related to the change of the electron temperature of electron density, key parameters in the generation of active species for the formation of ammonia. As shown in Figure 3.5, both gases show opposite effects on both T_e and n_e. These effects were already reported by Mansour et al. [103] and by Pu et al. [104] for adding He and Ar in pure N_2 plasma. Pu et al. explained these results in the following way. The electron energy distribution function in a plasma shows a tail region populated by high energy ("hot") electrons with energies above 30 eV. In the helium–nitrogen mixture, the tail is generated by He metastable states and superelastic collisions and is enlarged by adding more helium

in the discharge. As a result, T_e increases. However, when argon is added in the discharge, there is a sharp increase in electron density and hence a higher electron-electron collision frequency, which always tend to deplete electrons in the "hot tail" and decrease T_e. In the case of Ar in an H_2 plasma, Sode et al. [105] show that T_e decreases monotonically and they attributed the observed decrease to the increasing effective ion mass with increasing Ar fraction. As described by El-Sayed et al. [106], Ar can induce the dissociation of molecular nitrogen and increase the production of nitrogen atoms, however it has an insignificant effect on the nitrogen ionization mechanism. On the other hand, He addition enhances the production of, N^+ and N^- atoms through ionization, ionization dissociation and dissociative reaction, however it has a decreasing effect on the dissociative recombination mechanism.

Species	H_2	N_2	He	Ar
First ionization energy (eV)	15.42	15.58	24.56	15.76

Table 3.1: *first ionization energies of nitrogen, hydrogen, helium and argon*

In summary, on the catalyst surface, both He and Ar were to shown unfavorable impact on the hydrogen and nitrogen surface recombination to form NH_3. This effect, along with a high increase in the the electron temperature, is predominant when helium is added resulting in a total decrease of ammonia produced from the interaction of the plasma with the catalyst measured by RGA. Argon addition, on the other hand, was shown to increase the active nitrogen species in the plasma and, as a consequence, the percentage of ammonia formed. In this case, the competition between the ammonia increase in the plasma and the decrease on the surface results in a total increase of the production when a W catalyst is used.

3.3 Summary

To sum up, the rise of the surface temperature results in a decrease in the ammonia formed percentage due to two major factors. For high temperatures, the production results from the thermal decomposition of ammonia. For lower temperature range, no nitrogen gets released and the temperature increase causes the formation of more stable nitrides that does not tend to react further with hydrogen to form NH_2 and NH_3. These results implies that in the tokamak, the high temperature active area of the W divertor and its surrounding will not contribute much in the ammonia production. As the NH_3 formation is favoured by low temperature, a high contribution from SS pumping ducts and the plasma shaded areas is expected.

Finally, it was shown that the addition of helium and argon to the nitrogen hydrogen plasma have opposite effects on the ammonia production. While He effectively decreases the percentage of NH_3 by acting as a barrier for the surface processes, argon impacts more the plasma processes by increasing the active nitrogen species in the plasma and as a consequence the percentage of ammonia formed. This suggests that the presence of He as intrinsic impurity in the fusion plasma might help to decrease

the ammonia production and could further be used in a mixture with the nitrogen seeding gas. In contrary, it is not a good option to mix nitrogen and argon together to decrease the ammonia formation.

4

Ammonia interaction with gold, tungsten, boron, beryllium and stainless steel surfaces

D UE to its polarity, its aptitude to form hydrogen bonds as well its lone pair available for bonding, ammonia molecule may efficiently react with solid surfaces. In particular, the formed ammonia isotopologues in the fusion reactor are expected to stick on the tokamak surface materials before getting pumped. The in-vessel tritium inventory in ITER is limited to 1 kg for safety reasons and the sticking of large quantities of tritiated ammonia could contribute to the overall inventory by increasing the tritium retention, posing, therefore, a serious risk for ITER operation and maintenance. Quantification of NH_3 sticking and understanding of its adsorption mechanism on fusion-relevant materials are, in this context, of considerable importance.

The aim of this chapter is to investigate the interaction of NH_3 molecules with Au, W, SS, Be and B surfaces using a quartz microbalance (QMB) and X-ray photoelectron spectroscopy (XPS) techniques. The first section 4.1.1 will give a brief theoretical overview of the interaction types of a molecule with a solid surface. Then, a detailed explanation of quartz micro-balance theory and factors affecting its frequency shift will be presented in section 4.1.2 along with a new calibration technique for the QMB. In sections 4.3.1 and 4.3.2, a detailed NH_3 adsorption/desorption study will be presented by examining the effect of both pressure and surface material on sticking. Finally, an XPS study to analyze the residual NH_3 molecules sticking on the surface will be presented in 4.3.3.

4.1 Theoretical background

4.1.1 Interaction of atoms and molecules with surfaces

When an atom or molecule approaches the surface it feels the potential energy set up by the metal atoms in the solid. The interaction results in the formation of a bond between the adsorbate (atoms/molecules) and the surface. Depending on the nature of this bond, two cases are distinguished: physical and chemical adsorption called also

physisorption and chemisorption respectively.

Physisorption is a weak interaction (typically around 0.4 eV and below) characterized by the lack of a true chemical bond between the adsorbate and the surface, i.e. no electrons are shared. It is the result of Van Der Waals interaction (attractive but the weakest form of bonding) and a repulsive part originating from the kinetic energy increase of electrons in atoms at short distances from each other as a result of the Pauli exclusion principle.

In contrast to physisorption, chemisorption occurs through the formation of a chemical bond (ionic or covalent) with the surface. The binding energy, in this case, is typically found in the range of 0.4 to 8 eV per particle.
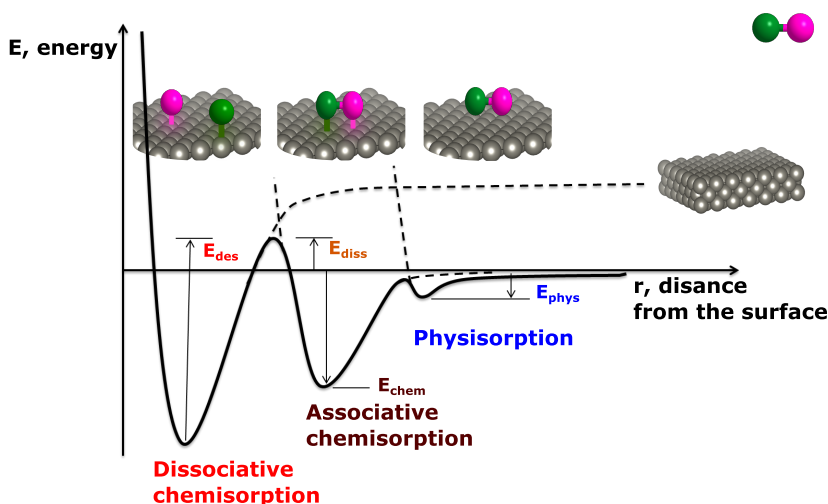
Figure 4.1: *Simplified schematic and potential energy diagram for the interaction of a molecule with a surface. E_{phys} and E_{chem} represent the energy required for the molecule to get physisorbed and chemisorbed on the surface respectively. E_{diss} is the activation barrier to overcome to dissociate the chemisorbed molecules into two chemisorbed atoms and E_{des} is the energy required to desorb these atoms from the surface.*

In Figure 4.1, a simplified potential energy curve for a molecule interacting with a surface is shown. When approaching, the molecule can lose its kinetic energy, get trapped in the weak attractive potential and become physisorbed on the surface. Through electron sharing between the surface and the molecule, the small energy barrier between the physisorbed state and the chemisorbed state is overcome and a net chemical bond forms. The molecule is then chemisorbed with an adsorption energy E_{chem}. The dissociative chemisorption of the molecule is possible if the molecules gets enough energy to go through the dissociation barrier (E_{diss}) and gets split into atoms that adsorb separately on the surface.

Another particular type of interaction specific to a limited range of molecules and in particular to ammonia is the hydrogen bond (H-bond) interaction. The H-bond is an intermediate interaction (0.1 to 1.7 eV) between covalent or ionic bonding and Van Der Waals bonding, making it strong enough to create stable structures but also sufficiently weak to be easily broken at ambient temperatures. This bond results from the

attractive force between a hydrogen atom covalently bonded to a very electronegative atom such as a N, O, or F atom and another very electronegative atom. In molecules containing N-H, O-H or F-H bonds, the large difference in electronegativity between the H atom and the N, O or F atom leads to a highly polar covalent bond where the H atom bears a large partial positive charge and the N, O or F atom bears a large partial negative charge. As a consequence, the positively charges H atom in one molecule is electrostatically attracted to the N, O, or F atom in another molecule. It is worth to mention here that, specifically for ammonia molecules on a surface, the hydrogen bond can form either between NH_3 and adsorbed residual oxygen on the surface or between ammonia molecules themselves.

4.1.2 Quartz Microbalance theory

The adsorption of ammonia and specifically the quantification of the adsorbed mass on fusion relevant materials surface was studied in this chapter using the quartz microbalance technique. The fundamental principle of this technique is based on the measurement of the frequency change of a crystal due to the mass loading, Δf_m. However this frequency change is not only affected by the mass change but by 4 other factors. These factors can be classified into two groups; namely the physical parameters of the surrounding gas and the structural parameters of the crystal. The former includes the temperature, pressure, viscosity, and density of the surrounding fluid, whereas the latter involves the mass loaded on the crystal and the surface roughness of the crystal. The total frequency shift of the QMB can be written in the form:

$$\Delta f = f - f_0 = \Delta f_m + \Delta f_T + \Delta f_P + \Delta f_\nu + \Delta f_r \qquad (4.1)$$

where Δf is the shift of frequency from the fundamental value f_0, f is the measured frequency of quartz, Δf_m, Δf_T, Δf_P, Δf_ν and Δf_r are frequency shifts related to mass loading, temperature change, pressure change, density/viscosity of the surrounding fluid and the roughness of the QMB surface respectively.

The response of the QMB to thermal changes was neglected in this work (i.e. $\Delta f_T = 0$). In fact, all our experiments were performed at room temperature (RT) with ± 0.4 °C temperature variation per day, implying less than 0.04 Hz frequency variation per adsorption/desorption cycle for the AT-cut quartz crystal used in this work (1.3 Hz variation per degree between 15 and 45 °C [107]). In addition to the temperature fluctuation around RT effect, the QMB vibration could also impact the quartz temperature. For a vibration at 6 MHz with a 10 nm oscillation amplitude [108,109], we calculated a maximum temperature increase approximatively equal to 0.3 °C, thus negligible in this work.
The mass effect on the QMB frequency was first derived by Sauerbery [110] and is given by:

$$\Delta f_m = \frac{-2nf_0^2}{(\rho_q \mu_q)^{\frac{1}{2}}} \Delta m = -C_m \Delta m \qquad (4.2)$$

Where n is the number of faces of the crystal in contact with the gas, ρ_q the density of the quartz ($\rho_q = 2.648$ g/cm^3), μ_q the shear modulus of quartz ($\mu_q = 2.947 \times 10^{11}$ g/cm.s^2),

Δm the change in mass per unit area and C_m the mass sensitivity of the QMB. For our experiment, the gas is in contact with both sides of the QMB and n is thus fixed to two for Au bare crystals. For other materials (SS, W, B and Be), as the coating was done only from one side of the crystal, n is fixed to 1 and the mass of ammonia adsorbed on the Au back-side was subtracted from the total mass.

Both Δf$_P$ and Δf$_\nu$ terms are associated with the influence of the medium surrounding the quartz crystal. The effect of pressure can be described as the frequency change due to the hydrostatic pressure exerted on the crystal by a hypothetical gas of zero density. It represents the compression effect of an increasing pressure of the surrounding gas on the quartz crystal. Stockbridge [111] showed that the frequency increases linearly with increasing pressure (P) for the case of gases up to pressures of 1 bar and can be written as:

$$\Delta f_P = f_0 \alpha P = C_P P \qquad (4.3)$$

where α is the proportionality constant and C_P is the pressure sensitivity of the crystal. Both terms are independent of the type of fluid in contact with the crystal. Considering the value of α proposed by Stockbridge for a 6 MHz resonating crystal, the C_P calculated is equal to 6.28×10^{-3}. The density (ρ_f) and viscosity (η_f) of the surrounding fluid increase with increasing pressure at a given temperature, leading to an amplitude damping of the oscillating QMB and consequent frequency decrease. Kanazawa and Gordon [112] quantified the relation between the frequency shift (Δf$_\nu$) and the viscosity and density of the surrounding fluids:

$$\Delta f_\nu = \frac{-n f_0^2 (\rho_f \eta_f)^{\frac{1}{2}}}{(\pi f_0 (\rho_q \mu q))^{\frac{1}{2}}} \qquad (4.4)$$

While Δf$_m$, Δf$_P$ and Δf$_\nu$ can be calculated directly using equations 4.2, 4.3 and 4.4, an analytical equation to precisely calculate Δf$_r$ cannot be found in the literature. Δf$_r$ originates from non-uniform morphology of the surface, where gas can fill the cavities and holes of the crystal and thus increase the mass loading on the surface. In most experimental work published so far, the roughness effect was not taken into account and only a few papers [113–115] have addressed the problem of quantifying the contribution from the roughness to the total frequency shift. However, it was found that surface roughness can drastically affect the resonance frequency of quartz crystal in contact with fluids [114]. In the next section 4.2.2, the method employed to derive Δf$_r$ will be presented.

4.2 Experimental section

4.2.1 Experimental procedure

The experiments were carried out in a SS vacuum chamber similar to the one described in 2.2.1.2 with a specificity of being equipped with a monochromatic source for the XPS allowing a better resolution of adsorbed ammonia peaks. The background pressure in the system during the process was better than 5×10^{-7} mbar. NH$_3$ interactions

with several surfaces was studied at different pressures in the range of 10^{-3} to 800 mbar.

A thin film of the desired elements was first deposited on the QMB surfaces. For that, 20 nm of tungsten (W), stainless steel (SS), and boron (B) were deposited using a magnetron sputtering technique with an Ar process gas at 0.01 mbar. The water-cooled magnetrons were operated in pulsed-DC mode with 496 ns pulse width and 50 kHz frequency. Powers were adjusted to 150 W for W and SS and 60 W for B depositions resulting in 0.23, 0.16 and 0.01 nm/s deposition rate respectively. On the other hand, beryllium (Be) deposition (20 nm) was performed by Thermionic Vacuum Arc (TVA) technique described in [116]. In fact due to the toxicity of Be, the deposition was not possible in our system and was done in INFLPR laboratory in Romania. Only the QMBs deposited with Be were exposed to air while the other materials were deposited and exposed to NH_3 without breaking the vacuum. In Table 4.1, we present the final atomic composition of deposited films as measured by XPS.

Table 4.1: *Atomic composition of deposited materials as measured by XPS*

Deposited material	Composition
W	W (89.6 %), O (10.4 %)
SS	Fe (63.8 %),Cr (12.1 %), Ni (7.6 %), O (16.5 %) Traces of Mo, C, Si and Cu
B	B (77.8 %), C (17.6 %), O (3.4 %) and N (1.2 %)
Be	Be (52.06 %), O (37.76 %), C (10.19 %)

When the QMB reached a stable frequency (less than 0.1 Hz frequency change per 30 min), NH_3 gas was introduced through leak valve from the gas line to the vacuum chamber after shutting off the valves to pumps. The NH_3 pressure was maintained for 30 minutes while the frequency of QMB was continuously monitored. During this time no wall outgassing effect was seen, i.e. after reaching the constant pressure and stopping the gas inlet, no pressure increase was seen however this pressure was slightly decreasing due to the ammonia sticking on the walls. The pressure decrease caused by the SS wall pumping of ammonia was continuously corrected by introducing the gas in the chamber until reaching back the constant pressure. By recording the frequency change of the quartz, the mass of NH_3 adsorbed on the surface can be determined using the method described in section 4.1.2. A gas desorption step was then done by pumping the gas from the chamber and measuring the resulting frequency. After the desorption process, samples were transferred without breaking the vacuum to the XPS chamber for chemical analysis at several time intervals.

To verify the reproducibility of the results, all measurements on W surfaces were performed twice and two adsorption/desorption cycles were repeated for SS, B and Au for one fixed pressure. Furthermore, to verify the accuracy of each new installed QMB crystal, an Ar cycle at 50 mbar was done before each experiment. Although Ar does not adsorb on the surface at RT, there is still an effect on the quartz frequency change (explained later in section 4.3.1)that can be used to verify the QMB's accuracy. The standard error measured was equal to 0.09 Hz which indicates the accuracy of the QMB

technique for our measurements. The error bars shown in Figure 4.7 were calculated by taking the two above mentioned points into account (50 mbar Ar cycle and experiment repetition). The QMB crystals used are AT-cut piezoelectric quartz crystals (6 MHz resonance frequency) with deposited Au electrodes purchased from Inficon company. The QMB was connected to a 6 MHz oscillator circuit (Inficon OSC-100 Oscillator). A frequency counter (Agilent 53132A Universal counter) was used to monitor the QCM oscillation frequency.

For the XPS characterization, samples were transferred without breaking the vacuum. The ultra-high vacuum (UHV) chamber is equipped with a monochromatic Al-Kα X-ray source (hν=1486.6 eV) and a photoelectron spectroscopy analyzer (VG ESCALAB 210) with an energy resolution of 0.5 eV at 20 eV pass energy. The Au 4f7/2 peak was set to 84 eV for electron binding energy (BE) calibration. Fitting of the core level lines was performed with the same procedure described in 2.2.3.2.

To characterize the roughness of the bare crystals before deposition and also of the deposited layers, a Tencor 500 alpha stepper was used. The average roughness (R_a) was obtained by averaging 10 measurements of 1 mm length.

4.2.2 Experimental methods for the determination of the frequency shift due to roughness

Herein, we present a calibration method using non-adsorbing noble gases that will allow extracting the frequency shift caused by the sample roughness. Based on the ideal model for surface roughness from Urbakh $et\ al.$ [117–119], and using a perturbation theory model for a slowly varying roughness surface [118,119], Δf_r can be written in the form:

$$\Delta f_r = -0.5 C_m C_r \rho_f \tag{4.5}$$

The slowly varying roughness condition for which this equation is applicable is valid when both the average lateral length of surface shapes (ridges and valleys) and the decay length (defined in [114]) is higher than the average height of the surface shapes. In order to calculate Δf_r in equation 4.5, the value of the roughness factor C_r should be determined. As shown in [114], for the particular case where the density of the adsorbing gas on the QMB is less than 0.2 g.cm^{-3} and the QMB roughness value is in the range of few nanometers to approx. 700 nm, C_r can be written as:

$$C_r = a_1(1 + b_1 \rho_f) \tag{4.6}$$

where a_1 and b_1 are the constants assumed to be independent of the gas type and the surface material.
All the QMBs used in this study, either bare rough Au coated crystals (as received from the manufacturer) or coated with 20 nm W, SS, B or Be, had R_a values comprised between 300 and 465 nm. Also, for our working conditions, i.e. temperature and pressure, and for all gases used in this work, density values do not exceed 0.015 g.cm^{-3}. Therefore, equation 4.6 can be applied.

Replacing C_r in equation 4.5, Δf_r can be written as a second order polynomial as a function of the gas density:

$$\Delta f_r = -0.5 C_m C_r \rho_f = -0.5 C_m \rho_f (a_1(1 + b_1 \rho_f)) = B_1 \rho_f + B_2 \rho_f^2 \qquad (4.7)$$

To determine B_1 and B_2 values, we measured Δf_r for 3 noble gases Ar, He and Ne on a bare gold crystal. As these gases cannot adsorb at RT on any surface we can consider $\Delta f_m = 0$ and measure the total frequency shift. Then Δf_r is calculated directly by subtracting pressure and viscosity terms from the total frequency shift (see equation 4.1). Δf_r is plotted in Figure 4.2 as function of the gas density. Using a second order polynomial fit, B_1 and B_2 coefficients were extracted, allowing one to calculate Δf_r for NH_3 gas.
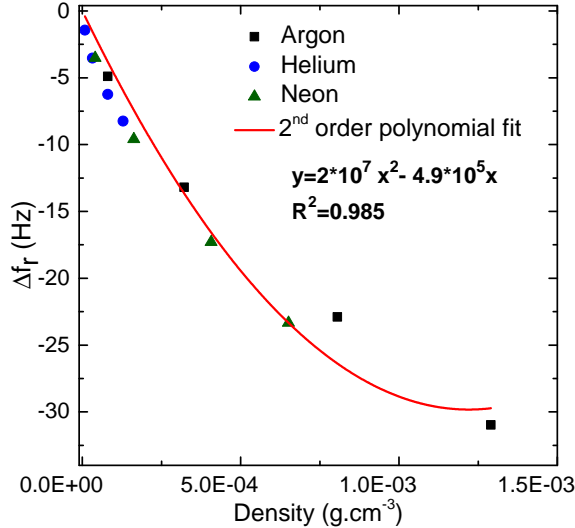
Figure 4.2: *Frequency shift caused by the crystal surface roughness as a function of gas density measured for Ar, He and Ne on Au surface fitted with a second order polynomial.*

4.3 Results and discussion

4.3.1 Interaction of NH_3 with different materials

NH_3 adsorption/desorption cycles done at 50 mbar will first be presented on Au and W surfaces and compared to a reference Ar adsorption/desorption cycle done on Au (non-reactivity and zero adsorption at RT). The results of adsorption cycles of (a) Ar on Au bare crystal, (b) NH_3 on Au bare crystal and (c) NH_3 on W coated Au crystal are shown in Figure 4.3.
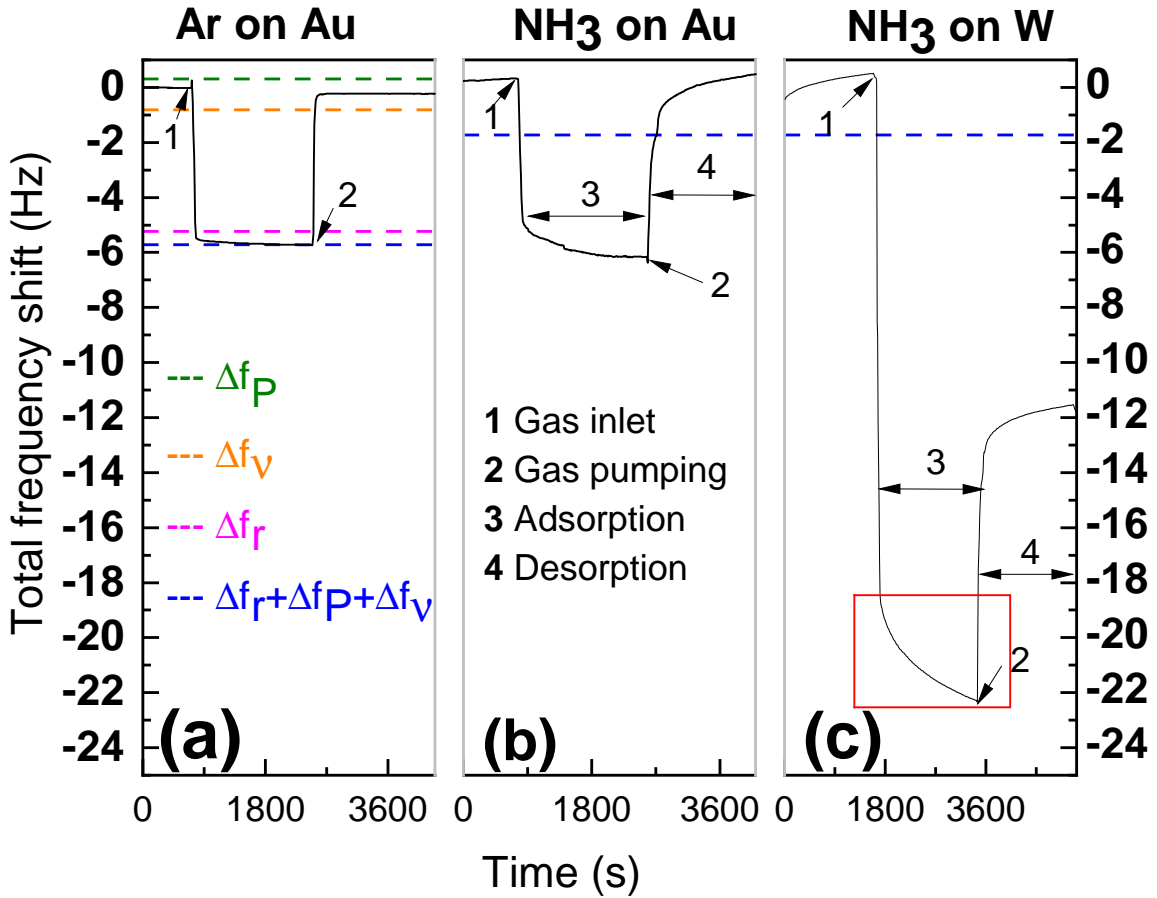
Figure 4.3: *Total frequency shift as a function of time for adsorption/desorption cycle at 50 mbar of a) Ar on Au, b) NH_3 on Au and c) NH_3 on W surfaces.*

The QMB total frequency shift as a function of time is represented by the black curve while the blue dashed line represents the calculated sum of Δf_P, Δf_ν and Δf_r. As can be seen, the sum of the three terms is higher for Ar than NH_3 due to the higher density of Ar ($\rho_{Ar} > \rho_{NH3}$). In fact, while Δf_P does not depend on the gas nature, Δf_ν and Δf_r both increase with the gas density. The typical behaviour of a non-adsorbing gas ($\Delta f_m = 0$) is shown in Figure 4.3a. A sudden frequency decrease is observed when Ar was introduced. The vertical slope corresponds to the phase when the gas pressure is rising until reaching the constant value of 50 mbar. As the desired pressure is attained, the total frequency variation stabilizes and corresponds to the sum of pressure, roughness and viscosity effects on the QMB (blue dotted line). By pumping the gas from the vacuum chamber, these effects disappear and the QMB returns to its initial resonance frequency. As seen in Figure 4.3b, NH_3 exhibits a different trend on Au. The total frequency shift is much higher than the sum of Δf_P, Δf_ν and Δf_r. According to equation 4.1, this observation indicates that the observed frequency is mainly due to adsorbed mass on the surface. When the gas was fully pumped from the chamber, the QMB returns to its initial resonance frequency value,

indicating a total desorption of NH_3 molecules from the Au surface. The QMB coated with W behaves differently as can be seen in Figure 4.3c. In fact, the measured total frequency shift caused by the NH_3 adsorption is around 3.5 times higher on W than on Au indicating that more NH_3 can adsorb on the W surface. Moreover, after the pumping of the chamber, the initial resonance frequency was not reached and, as the base pressure is recovered, there is no residual NH_3 in the vacuum chamber. This indicates that the partial frequency recovery can only be caused by remaining NH_3 molecules on the QMB, i.e. a partial NH_3 desorption.

Taking a closer look on the adsorption phase, one can notice that even though the pressure reached the desired value, the frequency continues to decrease for NH_3 on Au or W with different slopes depending on the material. For clarifications, this phase was highlighted in Figure 4.3c with a red box. The slope is steeper on W than on Au surfaces, probably because of different adsorption kinetics of NH_3 molecules on those surfaces. More information could be obtained by applying and adjusting a kinetic model to our results. Over the years, a wide variety of kinetics models have been proposed (Langmuir, Pseudo order 1, Pseudo order 2, Pseudo order n, Elovich, Crank, Boyd, Bangham, Weber and Morris...) [120] but none were used in this work as kinetics do not represent the main focus of this study. Yet, the adsorption equilibrium was not reached during the 30 min of exposure time and it is important to quantify the amount of NH_3 molecules that is missing compared to the equilibrium case.
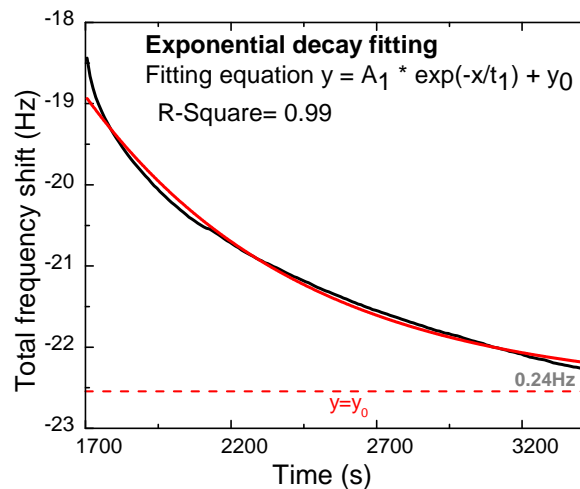
Figure 4.4: *Total frequency shift as a function of time following NH_3 adsorption at 50 mbar on W surface for 30 min. Red curves represent an exponential decay fitting for the measurement points.*

By fitting the total frequency shift during NH_3 adsorption on W with an exponential function, as shown in figure 4.4, it was found that the difference between the experimental frequency shift due to NH_3 adsorption on W after 30 minutes and the calculated frequency shift at the equilibrium from fitting is equal to 0.24 Hz. This value corresponds to approx. 1% of the total frequency shift measured after introducing the gas

at 50 mbar. We can, therefore, assume that after 30 minutes, the adsorption is close to steady state.

In order to explain the difference in NH_3 sticking between the studied materials, we refer to their electronic structure. In ammonia molecule shown in Figure 4.5, the sp^3 hybrid orbitals of the central nitrogen atom are formed by the overlapping of three half-filled orbitals of nitrogen with s-orbital of three hydrogen atoms. There remains a full-filled sp^3 hybrid orbital constituting one electronic doublet, lone pair. This doublet can be shared with an atom that has an empty orbital and thus forms a polarized covalent bond, with a partial positive charge on nitrogen and a partial negative charge on the atom that has accepted the nitrogen electrons ($N^{\delta+}$—$M^{\delta-}$). The strength of this chemical covalent bond is directly affected by the empty atomic orbitals on the surface as reported by Gundry and Tompk [121].
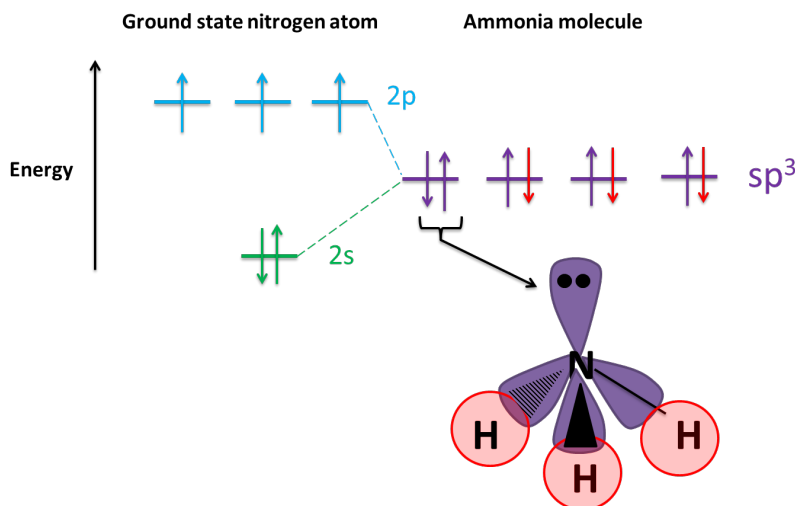
Figure 4.5: *sp^3 orbital hybridization in ammonia molecule*

On Au surfaces, NH_3 interaction is described as a "weak chemisorption" [122–125] arising from electron transfer from the NH_3 lone pair orbital to the partially filled Au s band. Yet calculations done by Ante Bilic *et al.* [126], based on DFT showed that the charge transfer from NH_3 to Au is minimal and the local densities of states and the charge distribution provide an indication of poor covalent bonding, i.e. a dispersive interaction. Beside this dispersive and/or weak chemisorption of NH_3 on the Au surface atoms, the low mass adsorption measured on gold, in our case, can be explained by another weak interaction. It consists of the NH_3 interaction via one of its H atoms to an O atom adsorbed on the surface [127]. XPS measurements (presented later in section 4.3.3) of Au coated QMB exposed to NH_3 showed that 11% of the Au surface atomic composition is physisorbed O (no chemical bond between surface oxygen and Au atoms). Therefore, the weak interaction of NH_3 on Au can also be explained by H bond between NH_3 and surface O atoms (purely electrostatic bond with the lower energy than the covalent bond).

On the other hand, NH_3 strongly chemisorbs on electron acceptor surface atoms such

as W with 4 electrons in the d orbitals, explaining the strong adsorption seen in Figure 4.3. It has to be pointed out that oxygen (from H_2O mainly) is also present on the W surface and can interact with ammonia via H bond but the strong covalent bond between the metal and nitrogen of ammonia is the dominant interaction.

The NH_3 adsorption showed that depending on the nature of the surface, NH_3 can adsorb in mainly 2 different ways: (i) weak interaction consisting of a weak chemisorption and/or dispersive interaction with Au atoms and/or an H bonding to the surface O atoms. The three interactions are weak bonding and can be broken when pumping the gas from the surface, explaining, therefore, the complete desorption of NH_3 from Au and (ii) a strong interaction where NH_3 molecules stick on the surface via electron sharing involving NH_3 lone pairs and the partially filled surface material valence bands. This results in a strong chemical bond and an incomplete desorption of the gas molecules from the surface after pumping.

4.3.2 Pressure effect on NH_3 adsorption/desorption process
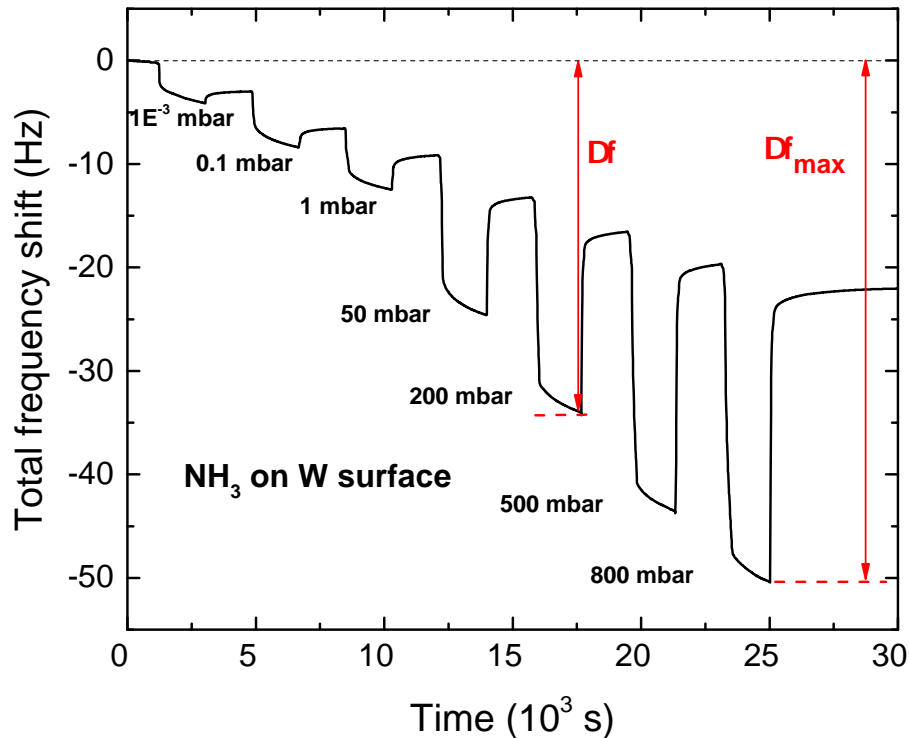
Figure 4.6: *Total frequency shift Δf as a function of time for the adsorption/desorption consecutive pressure cycles of NH_3 on a W surface.*

In order to investigate the effect of pressure on NH_3 sticking, consecutive cycles of NH_3 adsorption/desorption on Au, W, SS, B and Be (oxidized surface) were carried

out with pressures ranging from 1×10^{-3} to 800 mbar.

Note that for this consecutive cycle experiment, in order to make sure that the resulting equilibrium values at each fixed pressure are not affected by the previous amount of ammonia absorbed at earlier phases of the experiment, a freshly deposited W surface was exposed to a fixed ammonia pressure and compared to the amount of ammonia adsorbing on a previously exposed surface at lower pressure. Results showed that both amounts are equal indicating that a consecutive stepwise ammonia cycle on the same sample allows calculating the amount of ammonia adsorbed at each fixed pressure.

The results of such consecutive cycles are shown for a W surface in Figure 4.6 and three main trends can be observed: (i) the total frequency decrease following the gas inlet (Δf) is higher for each cycle at higher gas pressure, suggesting that the NH_3 uptake increases with the pressure, (ii) the frequency shift after the gas pumping i.e the non-desorbed mass remains larger for a higher pressure and (iii) no saturation was reached up to 800 mbar.
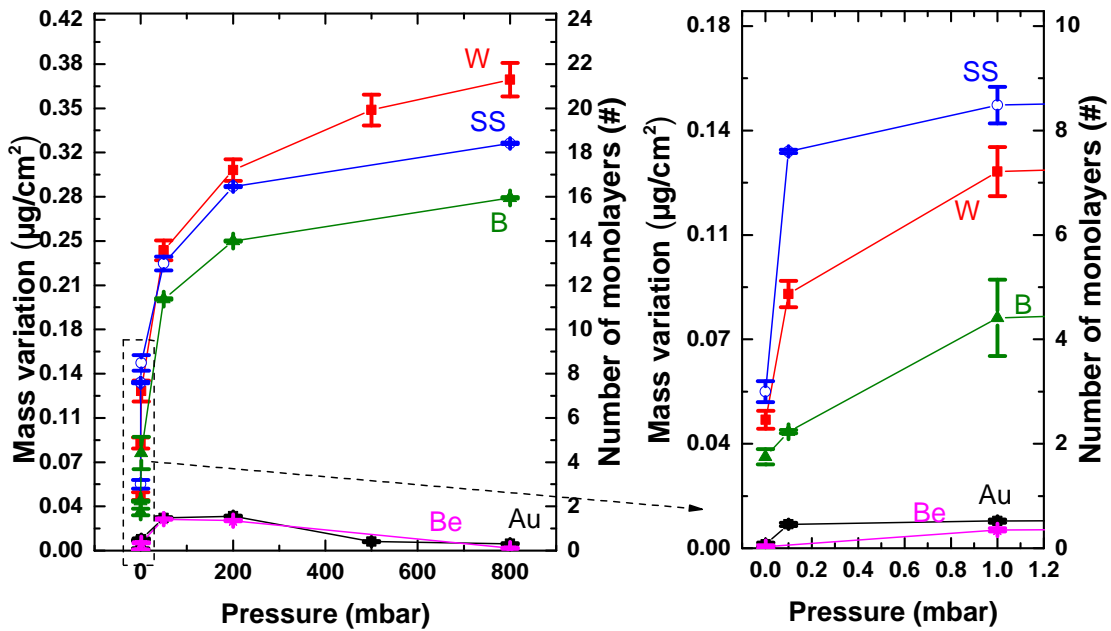
Figure 4.7: *NH_3 mass and number of ML adsorbed on W, SS, B, Au and Be surface after 180 sec of ammonia exposure as a function of pressure.*

The frequency change for each pressure was then extracted and the maximum value of the NH_3 adsorbed mass was calculated according to the procedure described in section 4.1.2, after subtracting the roughness, viscosity and pressure effect. In order to convert this mass uptake into a number of monolayers (ML) adsorbed on the surface, the following calculations were done. Assuming one ML is equal to 6.2×10^{14} molecules/cm² [128], the number of ML adsorbing on a surface can be calculated by dividing the number of gas molecules per surface area N_{NH3} by one ML. N_{NH3} can be calculated using the following equation:

$$N_{NH_3} = \frac{\Delta m}{M} \times N_A \qquad\qquad (4.8)$$

where M is the gas molar mass and N_A is the Avogadro number. We should note however that the number of ML can be overestimated as we assume a flat surface and neglect the effect of surface irregularities (steps, kinks...) on adsorption. Figure 4.7 represents the mass and number of ML of NH_3 adsorbed on Au, Be, B, SS and W surfaces.

4.3.2.1 Adsorption mechanism on Be, B and SS

From Figure 4.7 two major interaction types are observed: a low mass uptake for NH_3 on Be and Au surfaces that does not exceed 2 ML and a high adsorption for W, B and SS. As done earlier for Au and W in section 4.3.1, the interaction mechanisms of NH_3 on Be, B and SS can be explained and classified in two categories. For SS and B surfaces, NH_3 interaction exhibits similar behavior as W consisting of high adsorption and partial desorption. On the other hand, NH_3 adsorption on Be surface was observed to be equal to NH_3 adsorption on Au.
For Be, the highest occupied orbital s is filled, making the surface non-reactive to NH_3. A. Allouche *et al.* also confirmed that NH_3 does not adsorb on the Be surface [129]. Yet, in our experiment, NH_3 was found to adsorb on Be and can be explained by the presence of O on the surface. XPS measurements revealed 42% of O on the Be surface (both adsorbed and bonded to Be atoms forming oxides) and NH_3 is known to bind to adsorbed O or to the metal atom for BeO [127]. It should be noted that in the tokamak and precisely in the erosion zone Be will be only in the metallic state. As for Au, NH_3 is weakly bound to the Be surface and can be fully desorbed when pumping the gas from the vacuum chamber. Similarly to W, the three main constituents of SS, i.e. Cr, Fe and Ni possess electrons in the d orbitals (respectively 5, 6 and 8) and NH_3 can thus strongly chemisorbs on this electron acceptor surface. The pressure dependence of the adsorption on the SS surface observed in figure 4.7 (higher than W for low pressure less than 1 mbar and lower than W at high pressures) cannot be explained yet.
Regarding B, NH_3 interacts with the surface through a strong covalently bonded Lewis adduct where the electron deficient B atoms represent the Lewis base and NH_3, with its lone pair, plays the role of Lewis acid adsorbate. On SS and B surfaces, NH_3 is thus strongly adsorbed and is only partially desorbing when the gas is pumped from the vacuum chamber.

4.3.2.2 Pressure dependence

For Au and Be, the mass uptake increases with pressure until 200 mbar and then decreases for higher pressures which is still not understood. For W, SS and B, the adsorbed mass increases with the NH_3 pressure and no saturation was reached up to 800 mbar. At least 16 ML were measured for B, SS and W surfaces at 800 mbar, indicating the formation of a multi-layered system.

The formation of multilayers is a result of the polarization of the N-H bond as an intrinsic property of the ammonia molecule. In fact, nitrogen is more electronegative than hydrogen. Therefore, in the formation of N-H bonds, the distribution of electrons in the molecular orbitals is such that the electrons are closer to the nucleus of nitrogen. A partial separation of charge generates and makes partially negative nitrogen and partially positive hydrogen. This permanent dipole and the particular shape (pyramidal) of the ammonia molecule generates intramolecular forces such that each monolayer binds successive molecular layers, similarly to what happens with water.

When ammonia molecule adsorbs on a metallic surface, this polarization effect could also be heightened. When an adsorbed molecule loses charge from the lone pair orbital to the surface atom, this local loss polarizes the N-H bonds, causing the H to be even more positive, and increasing the strength of the H-bonds. This effect was confirmed by D.R. Jennison *et al.* for NH_3 adsorption on Pt surface [130]. They have calculated an H bond energy of 0.38 eV between the first adsorbed layer on the surface and the second layer of NH_3 molecules, almost three times higher than that of the gas phase NH_3 dimer $(NH_3)_2$. When NH_3 chemisorbs to Pt it donates electrons from the electron lone pair of the N atom to the empty Pt orbitals. The resulting increased polarization of the N–H bonds in the first layer of NH_3 molecules allows a second layer of NH_3 molecules to form unusually strong H bonds. Furthermore, the multilayer formation of NH_3 was shown previously on W [131], Ru [132, 133], ZrB_2 [134], Ni [135, 136] and SS [128] by different techniques.

Figure 4.8a illustrates this suggested mechanism where we present three intermolecular H bonds (red dashed bond in the figure) between NH_3 molecules from each single layer. The decomposition fragments of NH_3 shown in the same figure will be discussed in section 4.3.3.
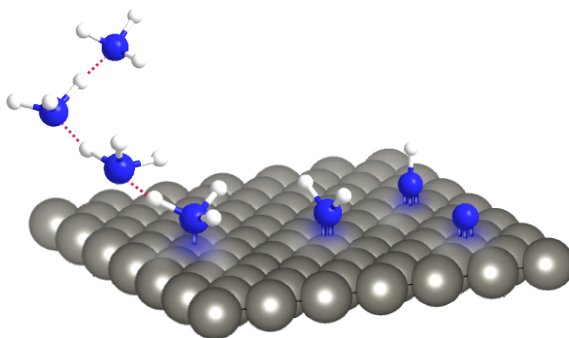
Figure 4.8: *a) Multilayer formation of NH_3 on the W surface through H bonds and b) NH_3 decomposition species on surface. N and H atoms are respectively represented in blue and white. The red dashed lines represent intermolecular H bounds.*

In the next section, XPS analysis of the non-desorbed NH_3 will be presented.

4.3.3 XPS study of non-desorbed NH_3

After the desorption process, samples were immediately transferred to the XPS chamber without breaking the vacuum. In Figure 4.9, the N1s core level spectra of Be and

Au surfaces before ammonia exposure (only for Be, was not measured for Au) and after the last NH_3 absorption/desorption cycle (see Figure 4.6) is presented. As can be seen, no N peak was observed, indicating the absence of NH_3 on both surfaces confirming, therefore, the total desorption discussed in sections 4.3.1 and 4.3.2.

For the other materials subject to strong NH_3 adsorption, i.e. B, W and SS, XPS measurements performed before and after exposure of NH_3 are shown in Figure 4.10. The B surface (Figure 4.10a) was composed of B (77.8 %), O (3.4 %), C (17.6 %) and N (1.2 %). The presence of N and C in the film is due to the fact that B atoms can easily catch species present on the vacuum vessel walls during deposition. The B was either in the form of a carbide B_4C (187.4 eV) or of a nitride BN (190.4 eV) or bound to other B atoms (188.4 eV) [137]. After exposure the N atomic percentage more than doubled from 1.2% to 2.7%, highlighting the bonding of NH_3 to the surface. It has to be pointed out that this increase cannot be related to the number of ML observed in section 4.3.2 as XPS measurements were done after the chamber pumping (ammonia desorption from the sample) and sample transfer. On the other hand, despite the presence of O and carbon (C) on the surface no BCNO (at 191.9 eV) nor BO (at 192–192.7 eV) [138] were measured.
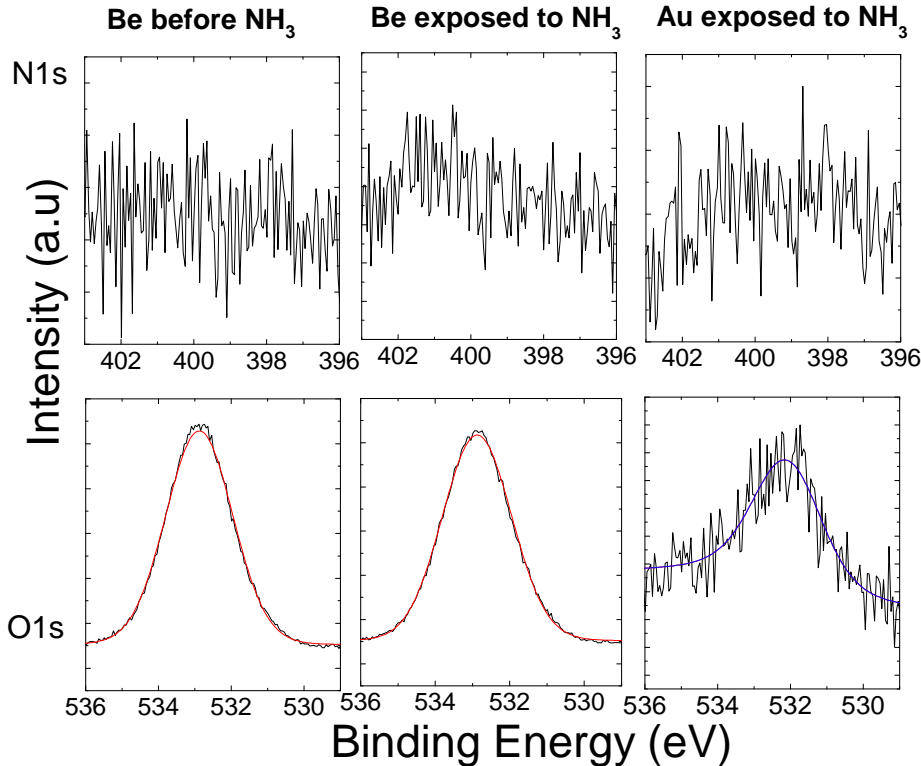
Figure 4.9: *N1s (top) and O1s (bottom) core level spectra recorded before ammonia exposure on Be surface and 30 min after NH_3 desorption from Au surface and Be surface.*

On the SS surface, Cr2p, Fe2p, and Ni2p core level spectra were measured before

and after NH_3 exposure. No change in Ni and Fe peaks were observed and this is probably due to the preferential reactivity of ammonia only with the highest electron acceptor metal of the SS which is the Cr (6 valence electrons missing compared to 4 and 2 for Fe and Ni respectively). Cr2p peak is, therefore, shown in Figure 4.10c. Before NH_3 exposure, the Cr was measured in a metallic state (Cr^0 at 574.2 eV) and in two different oxidic states: Cr^{+3} in Cr_2O_3 (576.2 eV) and Cr^{+6} in CrO_3 (578.2 eV) [139]. After NH_3 exposure, another peak was identified at 575.1 eV and could be assigned to Cr bound to N (CrN, Cr_2N or CrN_xO_y) [140,141]. This hypothesis is further supported by the absence of changes in the O1s core level spectra, indicating that the Cr peak at 575.1 eV is a sign of Cr-N bonding rather than Cr-O bonding.

The W surface was fully metallic before NH_3 exposure as shown in Figure 4.10c ($W4f_{7/2}$ at 31.1eV) [142]. W exposure to NH_3 resulted in the formation of W nitride with a peak assigned at 32 eV [143]. Similarly to B, no W oxides were measured at the surface despite the presence of 10% O on the surface, indicating that the O is only adsorbed on the surface and not bonded to W atoms [144]. Furthermore, no oxonitrides peaks were observed at 33.5 eV ($W4f_{7/2}$) and 35.71 eV ($W4f_{5/2}$) [145].
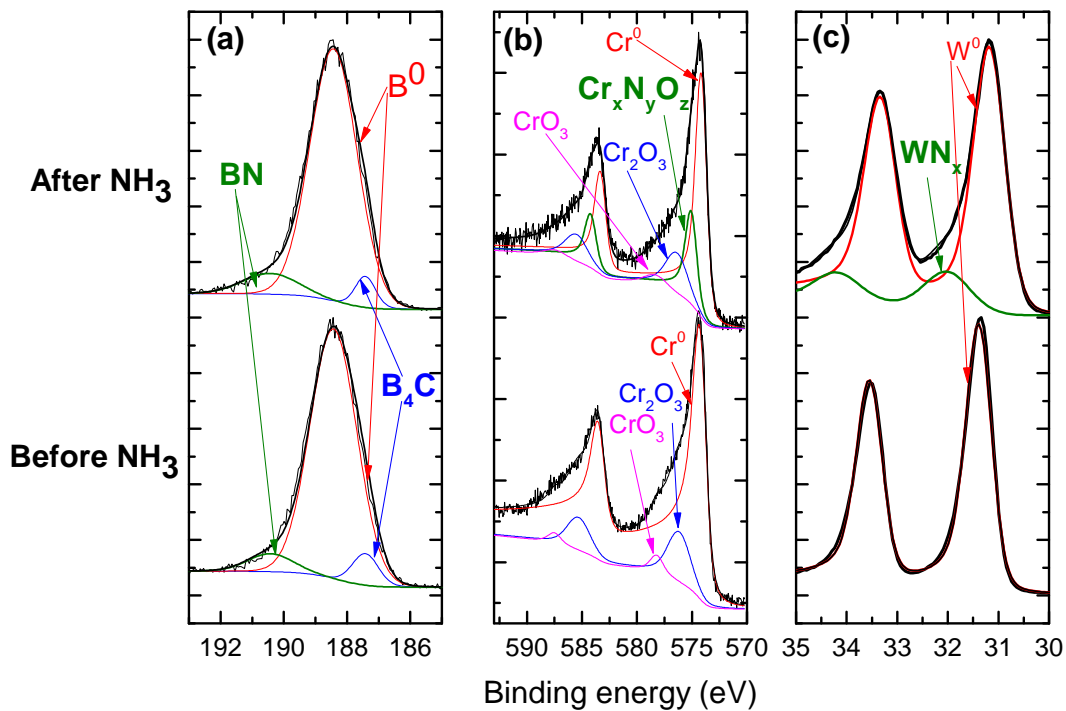
Figure 4.10: *B1s, W4f and Cr2p core levels spectra recorded before NH_3 exposure and 30 min after NH_3 desorption from a) B surface, b) SS surface (only Cr is shown) and c) W surface. The red, green, blue and magenta solid curves are the individual chemical states. Solid black curves are the raw data and the sum curves.*

In addition to XPS measurements performed 30 min after NH_3 exposure, N1s core

level spectra were recorded at different time intervals ranging from 30 min to one week after the NH$_3$ exposure. In between measurements, the samples were kept in the XPS vacuum chamber at 10^{-10} mbar. Results are shown in Figure 4.11 and the measured binding energy (BE) of the different chemical species are summarized in Table 4.2. B was the sole surface containing N before the NH$_3$ exposure with 2 peaks located at 397.8 and 399.0 eV, the former corresponding to CN and the latter resulting from B-N bounding.

After NH$_3$ exposure, the N1s core level spectra on the W surface can be decomposed in three peaks corresponding to a second layer of NH$_3$, NH$_2$, NH and/or surface nitrides (see Table 4.2). With ongoing waiting time, the decomposition products of NH$_3$, e.g. NH$_x$ (where x = 0, 1 and 2), saw their peak intensities increase while the peak intensity of NH$_3$ decreases, indicating a continuous decomposition of NH$_3$ on the W surface. A similar decomposition process was found on the B and SS surface. All the peaks were identified to be NH$_3$ and its decomposition products (except for CN on B surface at 397.7 eV), and the corresponding BE are given in Table 4.2.
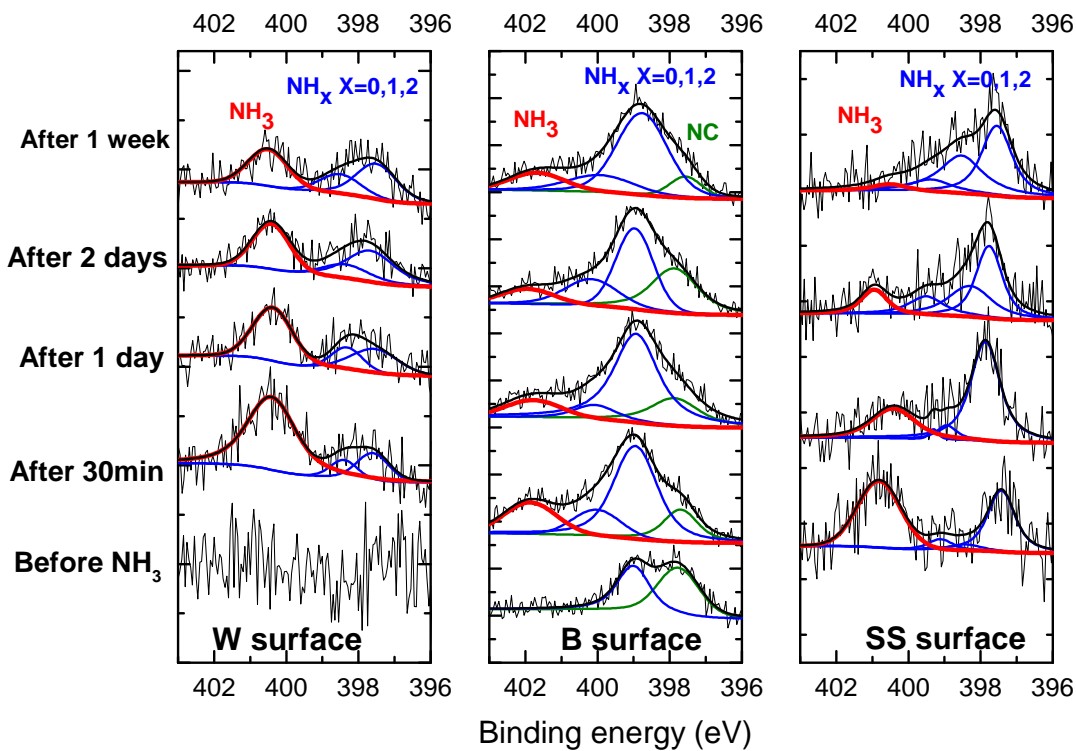
Figure 4.11: *N1s core level measurements for the W, B and SS surfaces performed before and after NH$_3$ exposure. The red curves are the individual peaks assigned to NH$_3$ while the blue curves stand for the individual peaks assigned to NH$_x$ (x = 0, 1 and 2). The black curves are the raw data and the sum curves.*

The XPS measurements showed a continuous decomposition of NH$_3$ into NH$_x$ (x = 0, 1 and 2) species, in agreement with previous studies done on W [85, 131, 146, 147],

B [148] and Cr [149]. The progressive dehydrogenation is schematized in Figure 4.8b, with NH_2, NH and N bound to the surface. During of the dehydrogenation process of the ammonia on a metal surface, ammonia loses hydrogen atoms from NH_3 to N. During this process nitrogen changes the hybridization from sp^3 (four orbitals direct along the corners of a tetrahedron, three bonds with hydrogen and one with metal N——M) to sp^2 (three orbitals direct along the corners of an equilateral triangle, two bonds with hydrogen and two with metal N═══M) to sp (three bonds with metal N═══M).

Table 4.2: *N1s BE values extracted from XPS measurement on W, B and SS surfaces after NH_3 exposure. Reference values from literature and the corresponding species were added to the table.*

Surface material	XPS N1s BE measured (eV)	XPS N1s peak BE from literature (eV)	Species
W	397.6 - 397.8	397.6 [131], 397.8 [131]	NH, surface nitride on W
	398.3 - 398.5	398.4 [85]	NH_2 on W
	400.4	400.7 [131]	second layer of adsorbed NH_3 on W
Cr	397.3 - 397.9	397 - 397.8 [139]	CrN
	398.3 - 398.9	398.6 [150]	NH_2 on Cr_2O_3/Cr
	399.1 - 399.5	399.0 - 399.8 [139]	CrN_xO_y
	400.4 - 401.0	400.7 [150]	NH_3 on Cr_2O_3/Cr
B	397.9	397.9 [151]	CN on B
	398.8 - 398.9	398.7 - 398.9 [137]	BN
	399.9 - 400.1	399.8 - 400.2 [152]	NH_2, NH on B
	401.7 - 401.9	401.7 - 402.1 [152]	NH_3 on B

4.4 Summary

In summary, NH_3 adsorption/desorption cycles performed on bare Au and on W, SS, B and Be coated quartz crystals showed that the adsorption process is pressure and material dependent. This material- dependent sticking in the fusion device would lead to a non-uniform distribution of adsorbed tritiated ammonia in ITER (highest on the W divertor and SS pump ducts).

The amount of NH_3 molecules bound to the surfaces was found to increase with increasing pressures for B, SS and W. Regarding Au and Be surfaces, a smaller number of ML was measured at higher pressures (500 to 800 mbar). No saturation was observed up to 800 mbar for W, B, and SS. Therefore, the adsorption of tritiated ammonia on the fusion device wall divertor and pumping ducts would be cumulative from one operational cycle (issues with tritium limit in the device) especially on the stainless steel surfaces which are not directly exposed to plasma impact.

In order to explain the difference in the adsorption between materials, two types of interactions were presented. A strong adsorption on W, SS and B due to electron sharing between the NH_3 and the surface, leading to a true chemical bond. This strong interaction led also to the formation of multilayers through H bonds. In this case, the desorption of the gas was not complete and a continuous decomposition of the NH_3 on these surfaces was measured with XPS performed during several time intervals after the exposure.

On the other hand, a weak NH_3 adsorption is assumed on Au and Be and explained

mainly by the H bond with O present on the surface. For those two materials, the desorption was complete according to QMB measurements and confirmed through XPS analysis. The total desorption shown on Au makes it a possible option as a coating material for the low neutron heat load SS pumping ducts to decrease ammonia and therefore tritium retention on these surfaces.

<div style="text-align: right;">*5*</div>

Mirror cleaning

C LEANING techniques for metallic first mirrors are needed in more than 20 optical
diagnostic systems from ITER to avoid reflectivity losses. Plasma sputtering is
considered as one of the most promising techniques to remove deposits coming
from the main wall (mainly beryllium and tungsten). Previous plasma cleaning studies were conducted on mirrors contaminated with beryllium and tungsten where argon
and/or helium were employed as process gas, demonstrating removal of contamination
and recovery of optical properties. Still, both above-mentioned process gases have a
non-negligible sputtering yield on mirrors. Our collaboration with the National Institute for Laser, Plasma and Radiation Physics (INFLPR, Magurele, Romania), allows
us to work in Be environment and offer us the possibility to use a sputter gas having
a small impact on mirrors while being efficient on Be deposits, namely deuterium. In
this chapter, two sputtering regimes will be studied, on laboratory deposits as well as
on mirrors exposed in JET-ILW, namely physical sputtering (220 eV ion energy) and
chemically assisted physical sputtering (60 eV ion energy) using capacitively coupled
plasma with radio frequency.

5.1 Deuterium plasma cleaning of Be contaminated mirrors

Metallic First Mirrors (FMs) will play a crucial role in ITER's optical diagnostic systems. Being the first element of the optical path allowing light from the plasma to
travel through the neutron shielding towards detectors, their reliability is crucial for
proper plasma analysis, i.e. well controlled fusion reactions. Therefore one main requirement for these FMs is the ability to reflect direct light to the next mirrors with
as small losses as possible during the whole ITER life time. Yet, as FMs will be placed
close to the plasma they will be subject to erosion and/or deposition [153, 154], the
latter being considered the most problematic for FMs. Indeed, more than 20 optical diagnostics, operating in the UV/Vis range, are expected to be affected by re-deposition
of beryllium (Be) and tungsten(W) eroded from the First Wall and require mirror

surface recovery techniques. The removal of such deposits via capacitively coupled RF plasma was the main focus of several studies in the past years [155–159], confirming the viability of this technique for ITER FMs, that is currently foreseen on optical diagnostics [160–162]. Nevertheless, it is to be noted that all of those experiments have been conducted with a Be proxy with similar chemical properties namely aluminium (Al) [163].

Previous experiments [164] devoted to plasma cleaning of Be contaminated deposits has been carried out in the JET Beryllium Handling Facility. Laboratory made deposits (Be and W) [164] and tokamak deposits grown in JET-ILW on typical FM material [165] (molybdenum (Mo) and rhodium (Rh)), were cleaned with helium (He), argon (Ar) or a mix of both with ion energies ranging from 200 to 600 eV. The deposits thickness was significantly reduced, often fully removed and accompanied by an increase of the reflectivity. Helium was proven to be as efficient as Ar on Be contaminants, even with the presence of W (up to 10 at.%). Nevertheless, some mirrors suffered from energetic sputtering, especially with Ar (increase of the diffuse reflectivity up to 12 % at $\lambda = 250$ nm). Helium offers a gentler cleaning, preserving the mirrors surfaces, although it still has a non-negligible sputtering rate on Rh and Mo. Despite good results, the previous study was limited to the use of noble gases and did not explore the possibility of deuterium due to safety regulations (later abbreviated as D or D_2).

D_2 is an interesting gas for Be removal due to its high sputtering yield on Be (both have a low mass) while having an extremely small sputtering yield on mirror material (see Table 5.1). It was shown in the last years that Be can be removed with D ions having as small energies as 7 eV due to chemically assisted physical sputtering (formation of BeD molecules) [166]. Björkas *et al.* also showed that chemically assisted physical sputtering is promoted at low D energies; at 60 eV, 60 % of the sputtered Be is in the form of BeD while at 100 eV it is nearly 0 %. Ar on the other hand has a high sputtering yield on both contaminants and mirror materials. In addition, the use of D_2 as a process gas for plasma cleaning routine in ITER has another advantage, namely preventing pollution of the Neutral Beam Injection (NBI) system used in ITER [167, 168]. Indeed, D_2 used during the plasma cleaning should not cause any problem for the NB injectors. On the other hand, if exposed to helium gas contamination, it was already observed that injectors needed to be re-conditioned (private communication). In the presence of nitrogen, cesium nitrides would form in the NBI ion source without any known way to remove them. For argon or neon, there were not yet any experiments conducted but it is likely that the NB injectors would need some re-conditioning.

To complete the aforementioned studies and ensure a wide variety of operational parameters for mirror cleaning in ITER, a new experimental campaign was developed with Be contaminated mirrors and based on the use of D_2 as a process gas. Two sputtering regimes were targeted, namely pure physical sputtering with high ion energy (220 eV) and chemically assisted physically sputtering with as low as possible ion energy (60 eV). Interesting here is to see whether small amounts of W present in JET-ILW deposits (up to 1.5 at.%) can become an issue for D-based sputtering.

In this chapter, laboratory coatings of Be as well as mirrors exposed in JET-ILW were plasma cleaned with deuterium and analysed thoroughly in terms of surface structure,

Table 5.1: *Sputtering yield and damage threshold of ITER relevant materials as function of gas and energy used for plasma cleaning. Data are extracted from [169, 170].*

Sputtering yield (10^{-2} at./ions)	Be	W	Mo	Rh
D^+ (60 eV)	2.4	0	0	0
D^+ (220 eV)	3.5	0	0.1	0.2
Ar^+ (220 eV)	16.3	22.2	25.7	52.8
Damage threshold (in eV)	Be	W	Mo	Rh
D	7	342	125	113
Ar	62	32	26	22

Table 5.2: *List of mirrors from JET-ILW and their location during exposure.*

Mirror	Location	Position in the channel
130 Mo	Outer wall	0.0 cm
184 Rh	Inner divertor	2.5 cm
186 Rh	Tungsten Wedge	0.0 cm

chemical composition and optical properties. The effectiveness of the deposits removal as well as the mirror's integrity was assessed.

5.2 Experimental Conditions

Beryllium deposition and cleaning processes were both conducted in a controlled environment namely the Beryllium Laboratory at the National Institute for Laser, Plasma and Radiation Physics (INFLPR) due to the toxicity of Be, especially in form of dust. The mirrors employed for Be laboratory deposits were 25 mm in diameter and 8 mm thick stainless steel (SS) polished samples (polished with SiC paper, diamond paste and alumina powder of 0.05 μm). Prior to Be deposition, each SS mirror was coated with a 500 nm thick Rh film using magnetron sputtering at the University of Basel to mimic an ITER first mirror (see deposition procedure in [171]). The mirror samples exposed in JET-ILW were 10×10×10 mm^3 polycrystalline Mo with one polished face. Two of them were coated with 1 μm of Rh as described above. The 3 mirrors were exposed in various locations of the tokamak including the inner divertor, the tungsten wedge and the outer wall (see [172,173] for location schematic). More information can be found in Table 5.2.

A vacuum system was constructed and installed in the Beryllium Laboratory and is presented in Figure 5.1. The system is composed of a vacuum chamber, evacuated to 1×10^{-4} Pa with a conventional pumping unit, a magnetron for Be deposition and a sample holder that can be rotated and biased for the cleaning phase.
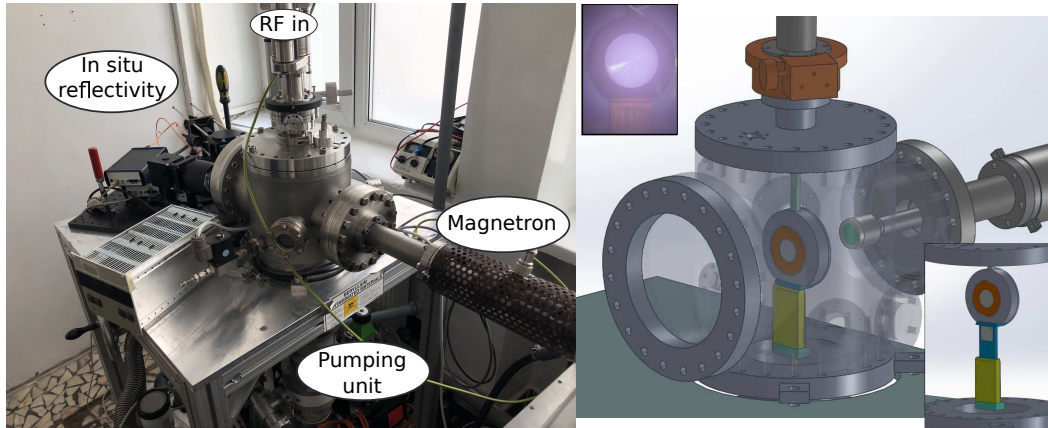
Figure 5.1: *Left : vacuum chamber employed in the Beryllium facility to perform deposition of Be and plasma cleaning. Right : CAD drawing of the chamber with magnetron sputtering system. The reference mirror for in situ reflectivity measurement is located below the electrode and protected in a cover (here in yellow). The top insert displays a picture of the cleaning discharge while the bottom insert shows the location of the reference mirror when moved out of the cover.*

5.2.1 Be Deposition process

For the laboratory deposits, a thin film of Be is first deposited on the mirror. The sample is thus placed in front of the magnetron (see Figure 5.1) by rotating the electrode. A water-cooled 2 inch target magnetron was employed in an Ar atmosphere at 3 Pa applying 60 W of RF at 13.56 MHz frequency. The deposition rate was monitored with a quartz micro-balance (QMB) and was equal to 1.3×10^{-2} nm.s^{-1}. The estimated thickness was also verified by cross-section SEM on films deposited on Si wafer. By adjusting the deposition time, different thicknesses were obtained. For cleaning experiments, the Be film was 30 nm thick while for erosion rate measurements, the thickness was equal to 100 nm.

5.2.2 Plasma cleaning

In order to remove the contamination from the mirrors, a plasma is generated by applying 60 MHz RF directly to the electrode (capacitively coupled discharge) on which the mirrors are mounted (one cleaning at a time as only one sample can be mounted on the rotational holder). Cleaning was performed in a pure D_2 environment with a pressure of 1 Pa. Due to the asymmetry between the powered to grounded areas, a negative DC component, the self-bias (V_{DC}), is created on the mirror that can be regulated by varying the RF power. The DC voltage across the powered electrode sheath is defined by $V_s = V_p - V_{DC}$, where V_p stands for the positive plasma potential (approx. 20 V). The maximum ion impact energy (in eV) is then determined by the sheath potential drop, e.g. V_s for the mirror [174]. In this study, self-biases of -40 V and -200 V were obtained by applying RF powers of 5 and 40 W, leading to ion energies of 60 and 220 eV respectively. When the mirrors were coated in the chamber, they

were directly cleaned afterwards without breaking the vacuum. On the contrary, the mirrors exposed in JET-ILW are exposed to air prior to the cleaning process. During the cleaning of all mirrors, the samples were rotated in front of a large window to conduct in situ relative reflectivity measurements (see Figure 5.1) during the process.

After the cleaning campaign at INFLPR, some mirrors were Be free but their reflectivity was not fully recovered. A second capacitively coupled RF plasma cleaning was therefore performed in Basel in a vacuum chamber with a base pressure of 1×10^{-5} Pa and using a frequency of 13.56 MHz. Ar was used as a process gas at 0.5 Pa.

5.2.3 Characterisation techniques

To follow the advancement of the cleaning, the change of reflectivity of the mirrors was monitored with a reflectometry system developed in Basel [175] for wavelengths ranging from 400 to 800 nm. Below the electrode on which the mirror to be cleaned is mounted, a Rh mirror is hidden and can be used as a reference for the relative reflectivity measurement. Moreover, the optical properties of this reference mirror were measured ex situ before the experiment and they are not changing with time as the mirror is covered during deposition or cleaning. This enables one to calculate absolute reflectivity of samples from in situ reflectivity measurements for given wavelengths (for example at 400, 550 and 700 nm wavelength as displayed in Figure 5.2). A typical evolution of the in situ relative reflectivity is shown in Figure 1 of [165].

The cleaning results were confirmed by ex situ measurements of the total and diffuse reflectivity with a Varian Cary 5 apparatus (250 – 2500 nm). After JET-ILW exposure, the total and diffuse reflectivity of contaminated mirrors were measured from 400 to 1600 nm using a photo-spectrometer (GetSpec) system complying with work procedures on materials retrieved from JET. All diffuse reflectivities shown or discussed subsequently always correspond to absolute reflectivities. Ion beam analysis (IBA) were conducted on JET-ILW mirrors after their exposure in the tokamak by a Heavy Ion Elastic Recoil Detection Analysis (HIERDA) set up with a time of flight tube for velocity measurements followed by a gas ionisation chamber for energy detection located at 45° relative to the incoming beam (36 MeV I) and symmetric incoming and outgoing angles [173,176]. Some specific HIERDA measurements were performed after cleaning steps employing 15 MeV $^{16}O^{5+}$ ions [177] using a foil-ERDA setup with a movable RBS detector. The incident beam angle and the exit angle as measured from the normal to the sample surface were both 75°. X-ray photoelectron spectroscopy (XPS) was performed for samples with low Be content (setup and fitting procedure described in [56]). Surface images were done using a Scanning Electron Microscope (SEM) from Hitachi (S-4800) capable of high-resolution imaging while energy dispersive X-ray analysis (EDX) was done on a SEM-FEI Nova Nano SEM23 microscope, where the beam voltage can be varied from 2 to 30 kV for surface composition measurements. For a thin film system, e.g. one or multiple layers on a substrate, the mass coverage of the layer(s) can be calculated by the film analysis software STRATAGem [178–181] from EDX determined k-values (the ratio of normalized intensity between unknown sample and standard) based on the Pouchou and Pichoir approach [182]. To obtain the precise Be amounts, the intensity of the Be Kα, C Kα, O Kα and Rh Lα lines were

measured for several electron beam voltages (5, 6, 7, 8 and 10 kV) where oxygen (O) and carbon (C) are coming from the air contamination (top layer). The information are then introduced in the STRATAGem software and the amount of Be on the Rh mirror is fitted to match the experimental intensities, given in μg.cm^{-2}.

5.3 Results and Discussion

Cleaning experiments were conducted on laboratory deposits and on JET-ILW mirrors. As the second type of sample is rather scarce due to long exposure time in JET (several years for some mirrors), experiments were first conducted on laboratory deposits that are not only easier to produce but also possess a well-defined contamination layer (controlled deposition) for straightforward conclusions.

5.3.1 Laboratory deposits

The first set of experiment was dedicated to the measurement of erosion rates of Be with low or high energy deuterium. Both the initial Be amount of a non exposed sample and the remaining Be amount after plasma exposure were determined by EDX analysis. The obtained results represent a quantity of Be per unit area expressed in μg/cm^2. In order to convert this quantity into thickness, a calibration measurement is required and can be obtained from another technique. In our case we measured the thickness of the reference sample (non exposed to plasma) by cross-section SEM on a cut done by focused ion beam technique that revealed an initial thickness of 100 nm, giving in turn a film density of 0.78 g.cm^{-3} (1.848 g.cm^{-3} for bulk Be). Partial cleaning experiments performed on Rh mirror coated with 100 nm of Be gave the following results: a removal rate of 0.198 nm.min^{-1} at high D energy (220 eV) and a removal rate of 0.052 nm.min^{-1} at low D energy (60 eV). Although the sputtering yields are similar for low and high energy ion energy (respectively 2.4 and 3.5 10^{-2} at./ions), there is nearly a factor 4 in the sputtering rate. It is well-known that self-bias, e.g. ion energy, and plasma density are simultaneously increasing with increasing RF power supplied to the discharge (see for example Figure 4.4 from [183]). Measurements performed with a retarding field energy analyser in an equivalent system (capacitively coupled plasma at 60 MHz, neon gas at 1 Pa) showed that the ion flux varies by a factor of 3.3 when going from -50 V to -200 V self-bias. A comparable ion flux increase is expected in our system, explaining the removal rates differences that we observed.

Cleaning trials were then performed on Rh coated mirrors on which 30 nm of Be was deposited. The aim of the cleaning experiments was to prove that all of the deposited Be could be removed without damaging the mirror material. The impact on optical properties of a 30 nm thick Be film can be seen in Figure 5.2 with 26, 27 and 27 % reflectivity loss for $\lambda = 400$, 550 and 700 nm respectively.The first sample, Rh #1, was cleaned for 8 hours with D$_2$ at 220 eV. The time was defined with the help of in situ reflectivity measurements, waiting for the reflectivity of the sample to reach a maximum followed by a plateau. Although the relative reflectivity was stable after 6 hours of plasma, the cleaning was extended by 2 hours to ensure a complete
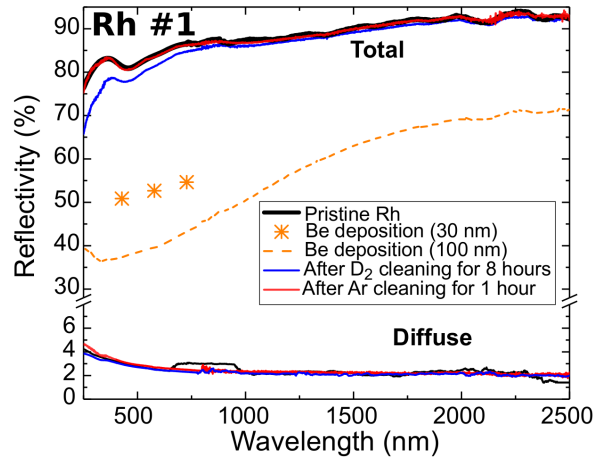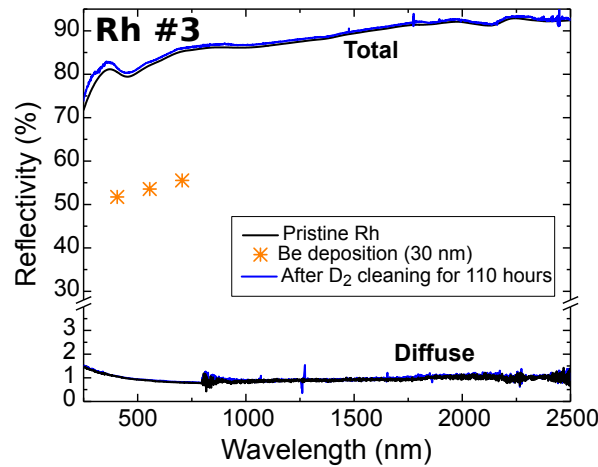
Figure 5.2: *Total and diffuse reflectivity of the Rh #1 mirror before Be 30 nm of deposition, after one cleaning with high energy deuterium at 220 eV (60 MHz) and after a final cleaning step performed in Basel with Ar at 220 eV (13.56 MHz). The Be film reflectivity at 400, 550 and 700 nm wavelength calculated from in situ reflectivity measurement is shown. The reflectivity of a thick Be deposit of 100 nm was added for comparison.*

removal of contaminants. The cleaning time is higher than expected from erosion rates measurements (30 nm should have been removed in 2 hours and 30 minutes). One possible explanation for this phenomenon is that as the amount of Be atoms becomes scarcer at the surface of the mirror, Rh or Mo atoms are affected by incoming D ions as well. Some of these Rh or Mo atoms can be eroded and redeposited back on the surface or, if their energy was too low for sputtering, they could as well migrate over the Be atoms, hiding them to sputtering. Another possibility might originate from plasma enhanced diffusion of Be atoms within the first layers of the mirror material. The situation with the last layers of contaminants will be investigated more precisely in further studies. The sample was later characterized off-site with SEM, XPS and ex situ reflectivity measurements. The XPS measurements, not shown here, revealed a Be-free surface, with carbon and oxygen (air storage) present along with Rh, the mirror material. The core level spectrum of Rh3d was fitted with one doublet at a binding energy (BE) of 307.2 eV, corresponding to metallic Rh [184,185]. SEM images taken after the D_2 cleaning displayed a flat surface without any peculiar structures (that would be indicative of remaining contamination but are not shown here, see for example Figure 7 of [165]). The surface was similar to the image shown in Figure 5.3 after D_2 plasma cleaning, where the initial nano-crystalline structure of the deposited Rh film can still be observed after the plasma cleaning. The situation is different for optical properties, not entirely recovered after the D_2 plasma, as displayed in Figure 5.2. Although the diffuse reflectivity did not increase during the cleaning process, the total reflectivity is still 9 % lower than the pristine mirror at $\lambda = 250$ nm.

As the surface of Rh #1 is free from contamination, the only possible explanation is a modification of the surface's optical properties due to the interaction of D with
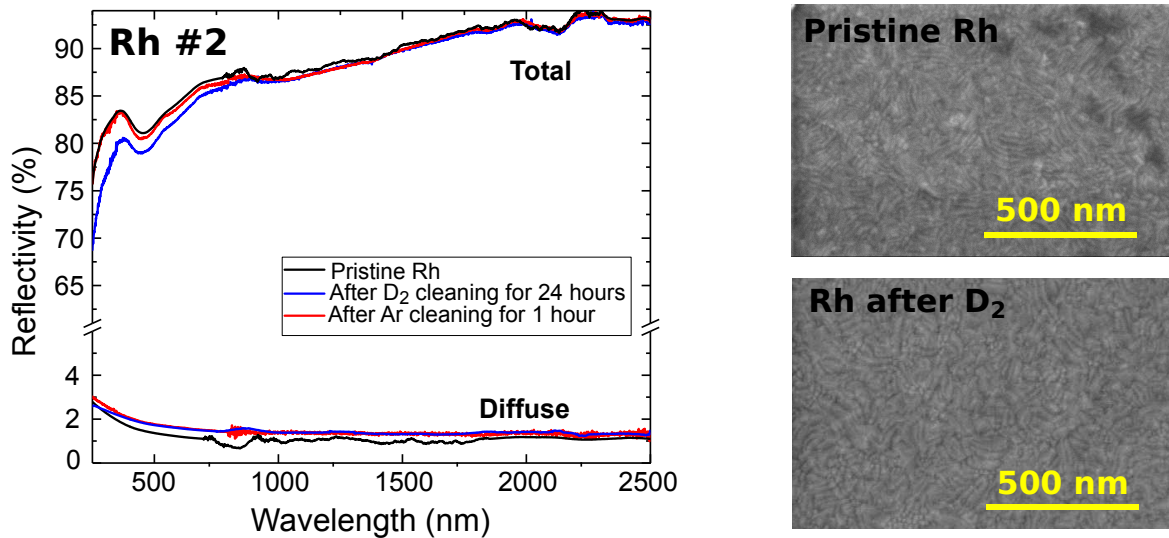
Figure 5.3: *Total and diffuse reflectivity of the Rh #2 mirror (no Be deposition) after one cleaning with high energy deuterium at 220 eV (60 MHz) and after a final cleaning step performed in Basel with Ar at 220 eV (13.56 MHz). SEM images of the pristine Rh mirror and after D_2 plasma cleaning at 220 eV are shown.*

the Rh surface. Such an effect was observed previously with molybdenum mirrors that were exposed to a D_2 plasma with 200 eV ion energy in a work done by Eren *et al.* in [56]. The same author also performed a similar study on Rh mirrors, exposing them to a D_2 plasma with 200 eV ion energy [186]. In this study, the reflectivity of the Rh mirror suffered from exposure to D_2 plasma in the vacuum chamber due to deuteride formation, but as soon as the sample was exposed to air, the reflectivity was restored immediately as D desorbs rapidly to air. In our case, despite the exposure of the sample to ambient after cleaning, the reflectivity was not recovered. To determine if the loss of reflectivity we experienced is effectively originating from the deuterium plasma exposure, a pristine Rh-coated mirror without any Be deposition, Rh #2, was exposed to a D_2 plasma at 220 eV for 24 hours with the same discharge parameters as for the Be contaminated samples. The reflectivity was measured ex situ (see Figure 5.3) and as can be seen, the reflectivity of Rh #2 decreased as well by 7 % at $\lambda = 250$ nm. SEM was employed to verify that the nano-crystalline structure of the Rh film was not altered by the plasma exposure (see Figure 5.3). Although XPS measurements cannot confirm the presence of D implanted in the mirror surface nor the formation of a Rh deuteride, the reflectivity decrease offers a clear evidence that the plasma cleaning procedure at high ion energy favours the formation of stable deuterides. Compared to the study of Eren *et al.* in [186] where the Rh mirrors were heated to 150 °C, the plasma cleaned mirrors are heated to a maximum temperature of 50 °C due to the applied RF power and this temperature difference could explain the different observed behaviours. Further studies are needed but are out of the scope of this article.

In order to remove the surface of the Rh mirror contaminated by D, a second cleaning was performed at the University of Basel with Ar as a process gas (at 0.5 Pa) due to

its high physical sputtering on all kind of material and its inertness. The discharge was driven capacitively as in the cleanings performed in the Be facility but 13.56 MHz were employed instead of 60 MHz while the ion energy for Ar was set to 220 eV. The change in frequency will mainly affect the ion flux on the sample and reduce it by a factor 9 when going from 60 to 13.56 MHz (see [159]). The sample was cleaned for 1 hour (would correspond to 7 minutes at 60 MHz) and the reflectivity of the Rh mirror was fully restored as can be seen from Figure 5.3, indicating a complete removal of the D contamination. The sample did not suffer from this extra step as the diffuse reflectivity did not increase. Given the effectiveness of Ar cleaning to remove deuterides, an additional Ar cleaning was applied on Rh #1 mirror, using the same procedure as mentioned above. After 1 hour, the mirror's optical properties were completely recovered, without any increase of the diffuse reflectivity (see Figure 5.2).

A second mirror was coated with 30 nm of Be, Rh #3, and cleaned for 110 hours with D_2 at 60 eV. As the cleaning experiment at high deuterium energy was requesting more time than expected compared to erosion rate calculations and because low energy deuterium is not sputtering the Rh from the mirror (damage threshold at 113 eV), the cleaning of Rh #3 was performed over several days to ensure a complete removal of contaminants. The mirror was characterized after the exposure. XPS measurements highlighted the absence of Be on the Rh surface (metallic at binding energy of 307.2 eV) that was slightly contaminated with C and O due to air exposure. SEM images taken after the cleaning indicated that the surface of Rh #3 still possesses a typical nano-crystalline appearance, similar to the one shown in Figure 5.3. Finally, the optical properties of the pristine mirror were restored as displayed in Figure 5.4 and no deuterides affected the reflectivity. It is currently not known whether no stable deuterides were formed on the Rh surface or if the amount was too low to impact the optical properties of the Rh mirror. The diffuse reflectivity did not increase, as Rh cannot be sputtered at such low energies.

5.3.2 JET-ILW mirrors

The three mirrors exposed in JET-ILW (one Mo, two Rh) were heavily contaminated with material from the main wall (Be and W) as well as other typical JET elements (D, nitrogen (N), C and O). The exact amounts measured with HIERDA after the JET-ILW exposure are given in Table 5.3. Especially 130 Mo has an extremely high Be amount (a millimetric Be droplet was found on the mirror surface), probably originating from a melted Be tile due to an off-normal event (runaway electron for example) [187]. It is worth mentioning that W was present on all the mirrors, even for the one located in the main wall of JET, with percentage varying from 0.03 to 1.5 at.%, and to highlight that the damage threshold for W bulk with D is located around 340 eV ion energy. The mirrors optical properties were strongly degraded after the exposure in JET-ILW as can be seen in Figure 5.5, 5.6 and 5.7 (measurement carried out in the 400–1600 nm range due to Be and tritium contamination). Taking the example of mirror 186 Rh, it observed a reflectivity loss of 60 % at $\lambda = 625$ nm that would already have dramatic effects on an optical diagnostic operating in the visible light range, despite the presence of only 353×10^{15} atoms of Be per cm^2 (the main

Figure 5.4: *Total and diffuse reflectivity of the Rh #3 mirror before Be 30 nm of deposition and after one cleaning with low energy deuterium at 60 eV (60 MHz). The Be film reflectivity at 400, 550 and 700 nm wavelength calculated from in situ reflectivity measurement is shown.*

contaminant, equivalent Be thickness of 29 nm). To improve the clarity of discussion for the reader, the Be amounts measured by HIERDA in thin film units (10^{15} number of atoms per cm^2) were converted into an equivalent film thickness, by using Be bulk density of 1.848 $g.cm^{-3}$. It is to be noted that the density of Be oxide (BeO) could have been used for the equivalent thickness calculations but as all samples do not have a 1:1 Be to O ratio, the standard Be bulk density was employed.

Mirror 130 Mo was cleaned with a 220 eV D_2 plasma. Based on erosion rates calculated in section 5.3.1, the equivalent Be film should have been removed in 118 hours. As it was possible to conduct ex situ on-site HIERDA measurements of the Be quantity, the cleaning was segmented to follow the cleaning process and results are added in Table 5.3. During the first 72 hours, it was expected to have a reduction of the equivalent Be thickness from 591 to 231 nm but the sample only had 33 nm left, implying that JET-ILW deposits are removed faster than pure Be laboratory deposits (factor 1.5). Such an effect was already observed in a previous study where the cleaning was conducted with Ar and He [165]. The following cleaning steps (measurements after 80 and 86 hours) displayed a reduction in the erosion rates calculated after each cleaning and plotted in Figure 5.5. It was first believed that this phenomenon could originate from the fact that the remaining Be was implanted or diffused in the Mo in a so-called modified mirror layer, thus decreasing the concentration of Be on the surface and in turn reducing the removal rate of Be. Another possibility could arise if the W initially present would not be sputtered, leading to an enrichment of the surface with W acting as a protective layer against sputtering. Both hypothesis were disproved from XPS measurements conducted after 86 hours of plasma cleaning, that did not reveal the presence of Mo nor W but only Be along with C and O. Although the contaminant film composition is determined from HIERDA, the chemical state of Be is not known throughout the entire film thickness and could vary, contributing to

Table 5.3: *HIERDA characterisations after exposure in JET-ILW and after cleaning in the Be laboratory. Units are 10^{15} atoms per cm^2. The equivalent Be thickness was calculated using the standard Be density of 1.848 $g.cm^{-3}$ to give an estimation to ease the reading. The symbol (-) stands for not measured.*

Mirror	Be	Be thickness	D	C	N	O	W
130 Mo after JET-ILW	7300	591 nm	390	30	94	1125	2
130 Mo after 72 h	400	33 nm	-	-	-	-	-
130 Mo after 80 h	120	10 nm	-	-	-	-	-
130 Mo after 86 h	80	7 nm	-	-	-	-	-
130 Mo after 114 h	0	0 nm	-	-	-	-	-
186 Rh after JET-ILW	353	29 nm	69	14	29	300	12
186 Rh after 44 h	0	0 nm	-	-	-	-	-
184 Rh after JET-ILW	728	59 nm	298	52	204	408	10
184 Rh after 61 h	200	16 nm	-	-	-	-	-
184 Rh after 93 h	100	8 nm	-	-	-	-	-
184 Rh after 117 h	100	8 nm	-	-	-	-	-

erosion rates differences. Despite a removal of Be, the reflectivity was only slightly recovered after 86 h of cleaning with a strong increase of the diffuse reflectivity as shown in Figure 5.5, the latter most likely originating from a roughening of the contaminants surface under the impact of the high energy sputtering. A final cleaning step was conducted for accumulated time of 114 h. XPS measurements highlighted the absence of Be and W from the Mo surface (with C and O from air exposure) indicating a complete cleaning of the JET-ILW contaminants. The core level spectrum of Mo3d was fitted with three doublets corresponding to 3 different chemical states that are not in a metallic state (located at 227.8 eV), namely 36 at.% of Mo deuteride (Mo-D) at 228.3 eV BE [56], 24 at.% of Mo oxide (MoO_3) at 232.6 eV BE and 40 at.% of D_2 reduced Mo oxide at 229.2 eV BE [188]. Important to mention here is the low diffuse reflectivity measured after the Be removal. Indeed, as the Be is removed, the Mo mirror is almost not eroded by the high energy D ions (see Table 1), leading to a surface smoothening. Given the effectiveness of Ar cleaning to remove deuterides, an additional Ar cleaning was applied on mirror 130 Mo in Basel, using the procedure mentioned in Section 5.3.1. After 2 hours, the Mo was in a metallic state as measured by XPS, and the mirror's total reflectivity was completely recovered and exceeded the one before JET-ILW exposure. The latter is due to the fact that the mirrors are initially measured a few months after their polishing and therefore suffer from a slight oxidation of the surface. This phenomenon was previously described in [173]. With the Ar cleaning, the Be contamination as well as this Mo oxide layer are removed, leading to higher reflectivities. Regarding the diffuse reflectivity, a non-negligible increase of the diffuse reflectivity equal to 10 % at $\lambda = 250$ nm was noticed. This increase was expected due to the polycrystalline nature of the mirrors exposed in JET-ILW, and was previously observed in numerous publications [159, 164, 165, 189].

A second mirror from JET-ILW, 186 Rh, was also exposed to a D_2 plasma at 220 eV,
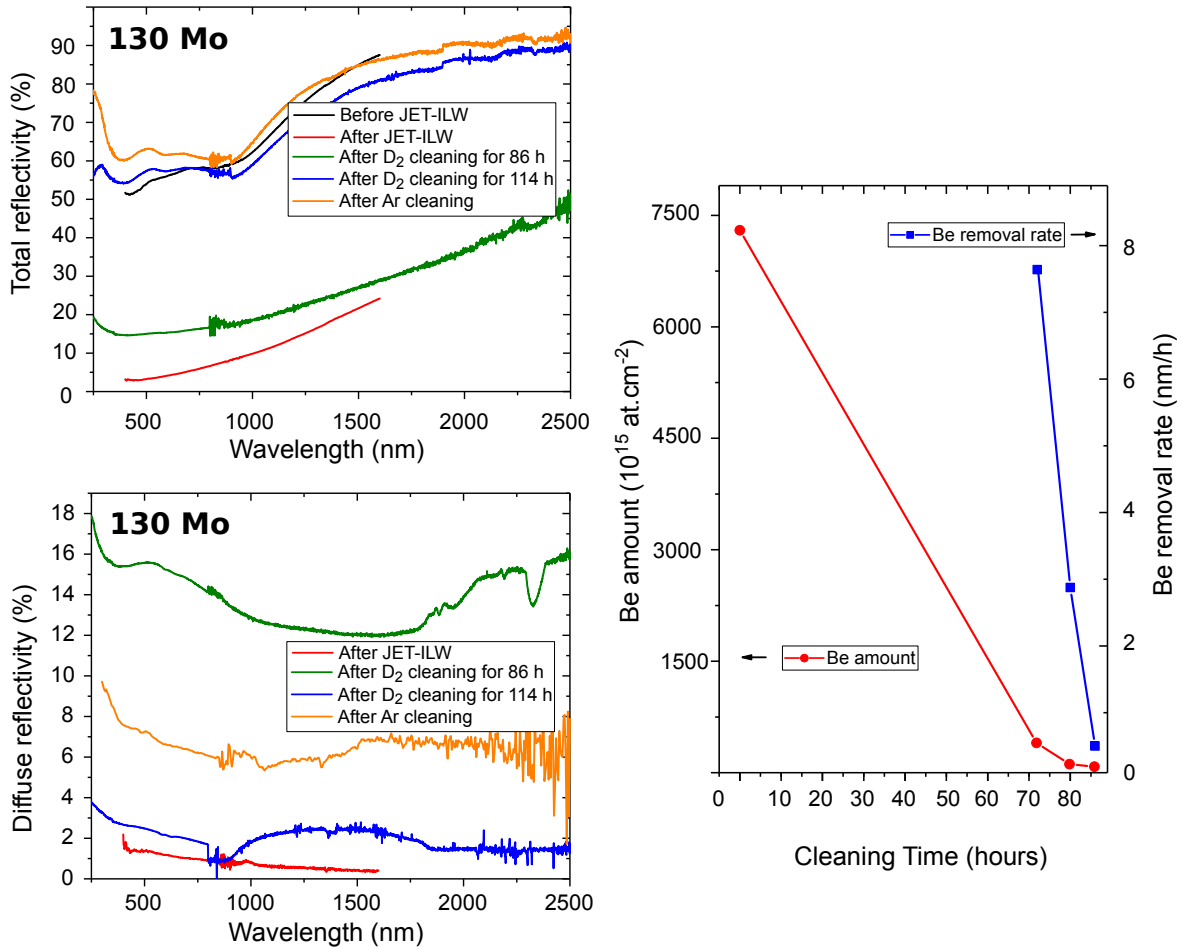
Figure 5.5: *Left: Total and diffuse reflectivity of the 130 Mo mirror before (only for total) and after exposure in JET-ILW, after two cleanings with high energy deuterium (220 eV) and after a final cleaning step performed in Basel with Ar. Right: Amount of Be measured on 130 Mo mirror after exposure in JET-ILW and after each cleaning with D_2. Calculated erosion rates for each cleaning are plotted except for the last D_2 cleaning (accumulated 114 hours).*
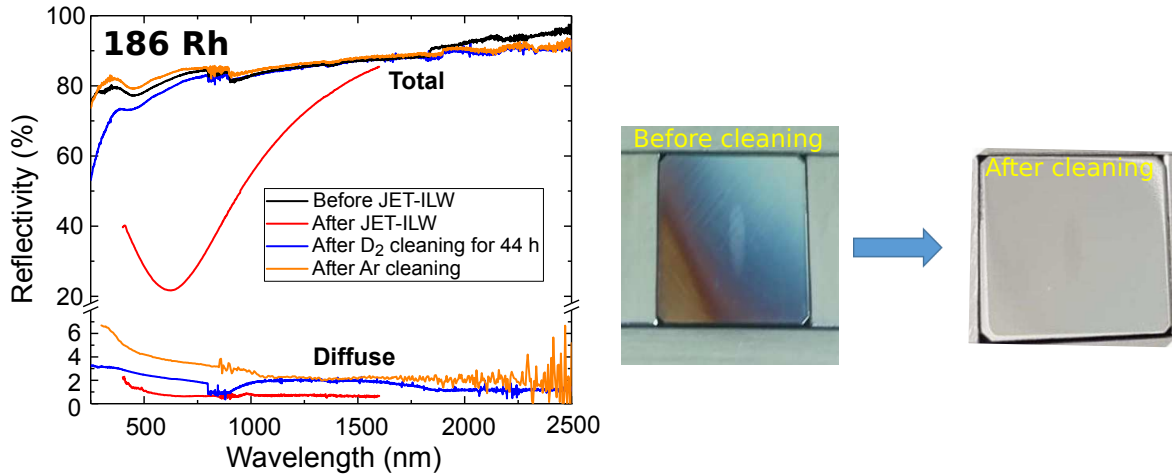
Figure 5.6: *Total and diffuse reflectivity of the 186 Rh mirror before and after exposure in JET-ILW, after one cleaning with high energy deuterium (220 eV) and after a final cleaning step performed in Basel with Ar. Picture taken after JET-ILW exposure (before cleaning) and after cleaning with high energy deuterium.*

this time for 44 hours to ensure a complete removal (according to erosion rates, 6 hours were sufficient). This sample had the particularity to contain 1.5 at.% of W in the contaminant film. After the cleaning procedure, the Be and W were completely removed from the mirror (verified by XPS), leading to a partial recovery of the reflectivity towards Rh deuteride values (see Figure 5.6). The effectiveness of the cleaning can also be observed by comparing pictures of the mirror taken before and after the D_2 plasma. A final cleaning step was needed in Basel with Ar, using the same procedure as mentioned in Section 5.3.1. After 2 hours, the total reflectivity was completely recovered, accompanied with a small increase of the diffuse reflectivity (see Figure 5.6) that remained below 10 %.

Finally, one JET-ILW mirror was cleaned with low energy deuterium (60 eV), namely 184 Rh. As for mirror 130 Mo, Be amount still present on the surface was measured with HIERDA between several cleaning steps (after 61 h, 93 h and 117 h, see Table 5.3) and are plotted in Figure 5.7 along with removal rates. The erosion rates are decreasing with on-going cleaning time and are even reaching zero (no net Be removal in the last step). The optical properties of the mirror were not recovered as Be is still present on the surface. The XPS measurements displayed extremely interesting results, as Be was not the sole contaminant still present on the surface but was accompanied with W. The core level spectra of Be1s and W4f were respectively fitted with one singulet and two doublets corresponding to oxides; BeO at 115.1 eV and for W 73 at.% of WO_3 at 35.4 eV BE and 27 at.% of WO_x, $2 < x < 3$, at 33.6 eV BE [190]. The decrease in erosion rate of Be towards zero is not originating from the implantation of Be in the mirror material as no Rh was recorded with XPS. Regarding the surface composition, it was found that the W at.%, initially equal to 1 at.% of the Be amount, significantly increased to reach 5.7 at.% after 117 h of plasma. Due to the high damage threshold for D on W (342 eV), the concentration of W on the surface is increasing with on-going
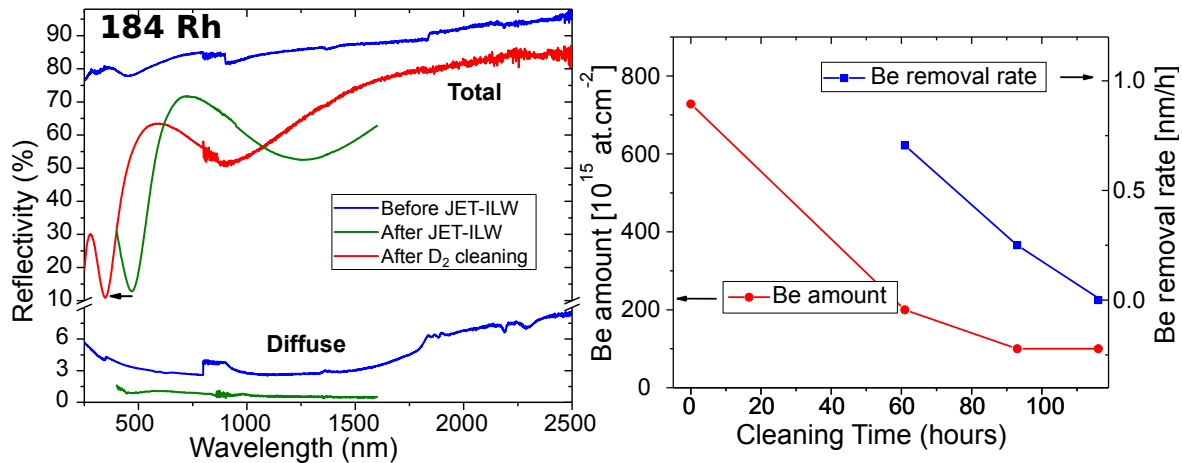
Figure 5.7: *Left: Total and diffuse reflectivity of the 184 Rho mirror before and after exposure in JET-ILW and after one cleaning with low energy deuterium (60 eV). Right: Amount of Be measured on 184 Rh mirror after exposure in JET-ILW and after each cleaning with D_2. Calculated erosion rates for each cleaning are plotted as well.*

cleaning time, up to the point where the entire surface is completely recovered with a thin W layer. The thin W layer will act as a protection against sputtering and the cleaning is no longer effective. Similar effect was already observed for EUROFER where an estimated W layer being two monolayers thick strongly reduced global sputtering under D plasma exposure [191]. One way to get rid of this protective layer would be to increase the D ion energy to overcome the damage threshold or to add another gas that possesses a lower damage threshold on W such as He (155 eV) or Ar (32 eV).

5.4 Summary

Rh and Mo mirrors were contaminated with Be, either deposited in laboratory or from exposure in JET-ILW that resulted in deposits containing up to 1.5 at.% of W. All contaminated mirrors were treated in the Beryllium laboratory at the INFLPR, which allows to work with toxic Be, using RF plasma with D_2 at different ion energies. Two sputtering regimes were investigated, namely physical and chemically assisted physical sputtering at respectively high (220 eV) and low (60 eV) ion energy. It was possible to remove all the Be contamination that was deposited with magnetron sputtering with low and high ion energy D_2 cleaning while it was only possible to fully remove deposits from JET-ILW at 220 eV. At lower energy, the fraction of W initially present in the deposit was not sputtered and led to a W-enrichment of the surface, acting as a protective layer against sputtering.

Although the reflectivity of all samples increased (except for JET-ILW cleaned at low ion energy), an additional step with Ar was needed for samples cleaned at 220 eV due to the formation of stable Rh or Mo deuterides. With this additional step, the pristine reflectivities were fully recovered without any noticeable damage to the surface, e.g. no increase of the diffuse reflectivity.

Yet, in order to employ D_2 alone in ITER for cleaning of all kind of deposits, additional points need to be cleared :

- Can the formation of stable deuterides be avoided for Mo and Rh based FMs?

- What is the maximum amount of W that contaminants deposit can contain to avoid the formation of a protective layer and hinder further cleaning?

Only when those questions are addressed can D_2 be considered for an ITER FMs cleaning regime where the entire vessel is filled with D_2 and all mirrors are cleaned simultaneously without damaging their surface.

<div style="text-align: right; font-size: 3em;">*6*</div>

Wall reflection

As previously described in chapter 1, the heat loads on the first wall and on the divertor is a critical issue for fusion reactor. The monitoring and protection system of plasma facing components (PFCs) is commonly ensured by infrared (IR) thermography. However, the interpretation of the IR measurements become much more complicated in a metallic environment since the signals will be perturbed by the significant contribution of the reflected flux in the total collected flux by the camera. The reflection from the metallic walls leading to false hotspots can be an important issue in ITER. In this chapter, a photonic simulation based on experimental optical properties measurement to discriminate the parasitic light-reflection to other thermal events is described. This chapter starts with an introduction 6.1 about the actual context and challenges of the standard IR thermography. Section 6.2 will then briefly describe the ray tracing photonic simulation based on multi-parametric models. In particular, a surface reflectance model decomposing the reflected light into three components is established in section 6.3 along with a general reflection model represented by the Bidirectional Reflectance Distribution Function (BRDF). A new redesigned and developed goniophotometer is presented in 6.4 with a description of the apparatus, the measurement and calibration procedure and the assessment of the accuracy of BRDF results followed by the major finding in the last section. A collaboration with the CEA Cadarache (IRFM Institute for Magnetic Fusion Research) during the thesis aimed to integrate these optical BRDF measurements in the ray tracing SPEOS software and the first results are shown in this chapter.

6.1 Infra Red thermography challenges in metallic tokamaks

Infrared thermography is a reliable and robust method widely used in tokamaks to monitor and to protect the PFCs by measuring in real time their surface temperature. Unlike carbon wall previously used fusion devices, the future tokamaks will be fully metallic. In particular, ITER PFCs will be made of beryllium and tungsten making

more complicated the analysis of the IR thermography measurement. Indeed, due to their low and variable emissivity (ranging from 0.1 to 0.5), the contribution of the reflected flux in the total collected photon flux by the IR camera will not be negligible anymore and could be even dominant [192–195]. It has been shown that the contribution of the reflected flux from the upper port visible/infra red system of ITER can lead to overestimation of the surface temperature of up to 20 % for the hottest targets and up to 90 % for the coldest surfaces [192]. These false hotspots resulting from the incorrect interpretation of the IR measurements could lead to excessive interruptions of the plasma shots as well as to limitations on scenario development towards high performance. The development of a photonic simulation taking into account the contribution of the reflected flux in the collected flux for surface temperature evaluation is therefore essential to discriminate the parasitic light-reflection to other thermal events with a real risk for the machine protection [196–198]. Furthermore, in order to get accurate results, this simulation will certainly have to be based on experimental data set for different PFC optical properties including their BRDF. In the following sections, details about a ray tracing photonic simulation will be given in addition to the experimental setup developed and employed to obtain the experimental BRDF data input for this simulation. Furthermore, bidirectional reflectance measurement of W samples will be presented. The knowledge of the optical properties of W is essential as it represents the material of the divertor, the component that withstand the highest heat loads in the tokamak and which temperature should be controlled. Some of the divertor target areas sustain a large fluence of incident energetic particles and are easily eroded which results in a change of their topography. The idea here is, therefore, to measure W samples with different roughness and correlate the directional reflectance to their surface roughness.

6.2 Ray tracing photonic simulation: SPEOS software

The photonic simulation code is based on a Monte Carlo ray tracing (SPEOS CAA V5 Based from OPTIS) able to propagate the ray through the complex geometry of tokamak and taking into account the multiple inter-reflections of the ray in the vacuum vessel.

As an output, the simulation delivers two images: the "real" image that reproduces the IR camera view and includes the reflected flux from the metallic walls and the "reflection free" image resulting from materials emission only. The reflection free image is therefore used to quantify the contribution of the reflected light from PFCs and evaluate the real surface temperature.

To do so, the simulation is based on three input models, shown in Figure 6.1, including the thermal scene model, the camera and optics models and photon-materials interaction model. While the thermal model presents the 3D distribution of the heat flux on PFCs and their resulting surface temperature, the optical model includes the camera geometrical parameters (field-of-view, image size in the focal plane and wavelength range) to reproduce the camera view. The accuracy of simulated results will depend on the accuracy of each model used as input of ray tracing code. The study in
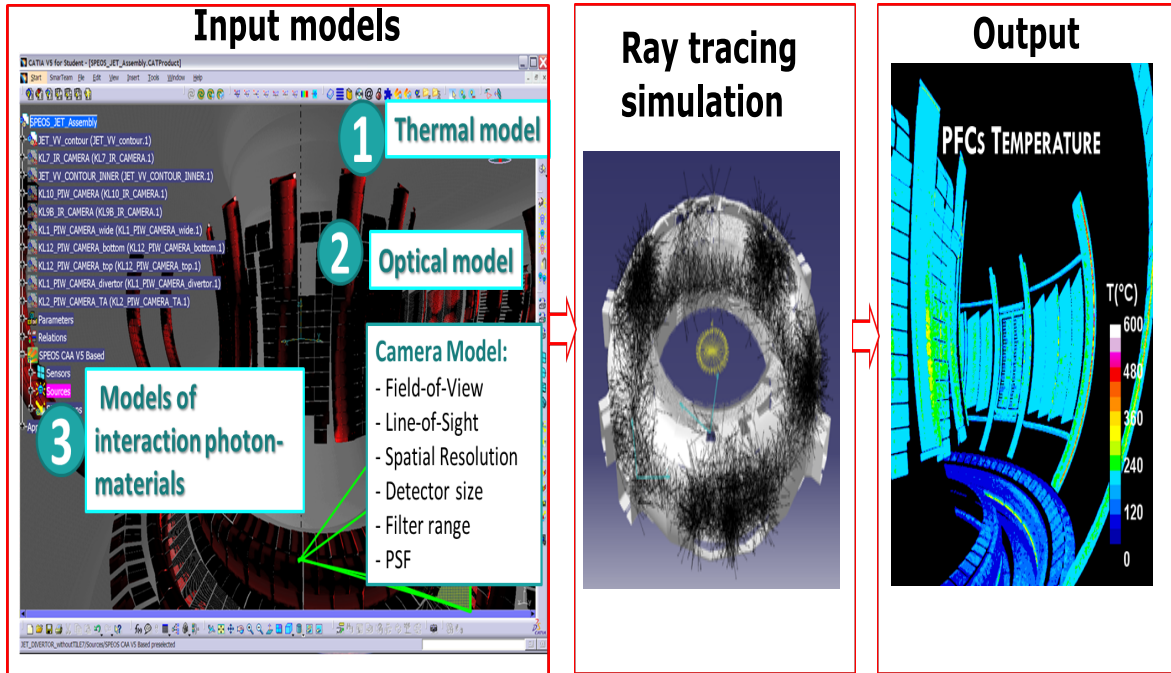
Figure 6.1: *SPEOS simulation main features*

this chapter aims to affine the model of photon-materials interaction from experimental measurements of a particular optical material property known as the bidirectional reflectance distribution function.

6.3 Surface reflectance model

The reflected light behavior is described with a combination of three main components shown in Figure 6.2: a diffuse, a specular and Gaussian reflectance.
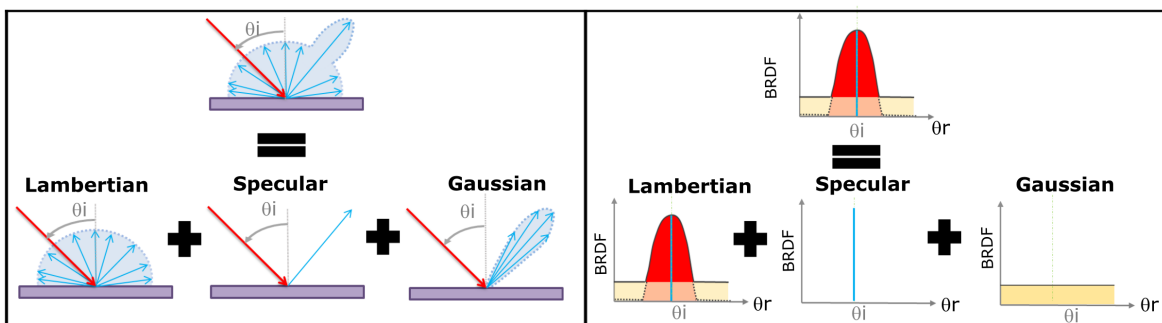
Figure 6.2: *Illustration of the reflectivity model as a combination of Lambertian, specular and Gaussian components. (left) Beam geometry (right) BRDF of each component.*

Diffuse reflection, also called Lambertian reflection, occurs with an equal spread of

reflecting light in all directions from a surface. Specular reflection occurs with directional reflection of light from the surface, with an incident angle equal to reflection angle defined by Snell - Descartes laws. An example of diffuse and specular reflectance for a sphere is shown in Figure 6.3. In practice, most of the specular materials reflection is a combination of a pure major directional specular components with a diffuse component following a Gaussian model, for which the reflected light has a Gaussian probability to be reflected with a particular angle around the main direction.
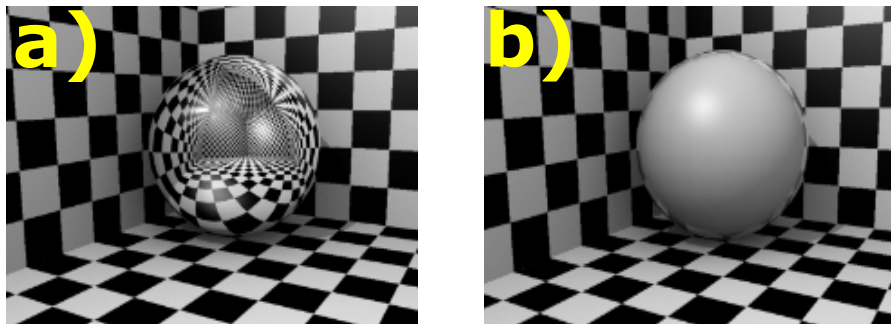
Figure 6.3: *An example of a)specular and b)diffuse sphere surfaces*

Reflection models are generally presented in terms of a BRDF: a combination of the three previously mentioned components. It is a general model that relates the energy arriving at a surface from the direction of illumination to the reflected intensity in the direction of the detector:

$$BRDF(\lambda, \theta_i, \phi_i, \theta_r, \phi_r) = \frac{L_r(\lambda, \theta_r, \phi_r)}{E_i(\lambda, \theta_i, \phi_i)} \tag{6.1}$$

Where λ is the wavelength of the incident light, E_i is the irradiance onto the surface, L_r is the radiance leaving the surface, (θ_i, ϕ_i) is the direction of the incident light and (θ_r, ϕ_r) is the direction of the reflected light presented in Figure 6.4.

In order to collect BRDF experimental data, a specialized measurement device called gonioreflectometer is used. The full description of this device and the measuring procedure is described in the following section.

6.4 Goniospectrophotometer

6.4.1 Setup description

Basel University Laboratory GOniospectrophotometer (BULGO) is a device with a four degree of rotational freedom designed to measure the optical properties of materials by measuring the directional reflectance of the sample as a function of angles of illumination and observation. The incident light on a material surface comes from the light source aperture. The light viewed by the detector is delimited by its aperture. Both the direction of illumination (θ_i, ϕ_i) and viewing direction (θ_r, ϕ_r), in spherical
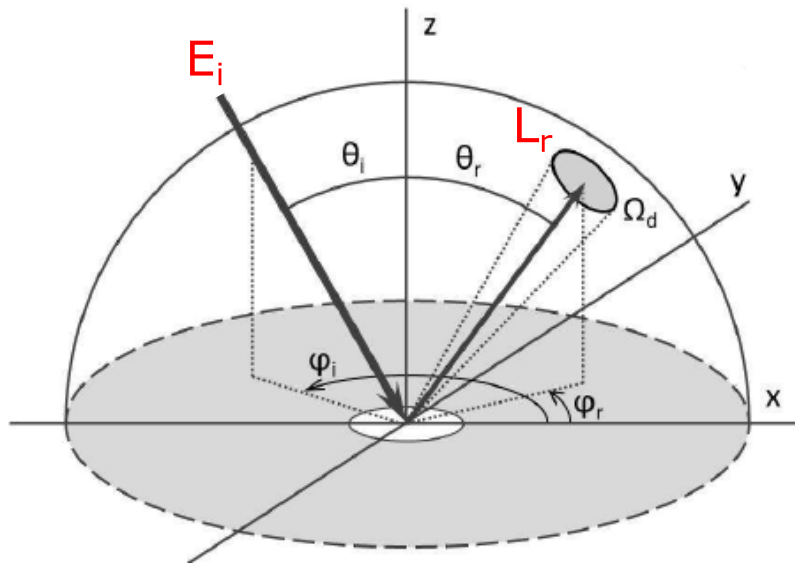
Figure 6.4: *Geometry for the definition of the BRDF (adapted and modified from [199])*

coordinates, can vary independently within the hemisphere above the material sample. An overview of this gonioreflectometer is shown in Figure 6.5b) and 6.5c)). The instrument consists of:

i) a rotatable and height adjustable sample holder

ii) a vertical half circular arc supporting the zenith motion of the light source

iii) a horizontal circular rail for the azimuthal motion of the light source

iv) a vertical stationary half-circular arc to support the zenith motion of the light collimator.

The light source mounted on the apparatus is a tungsten halogen 50 W Ushio lamp, inside a Lowel assembly of 12.7 cm diameter. The assembly allows for two possible settings on the lamp which are 'spot' and 'flood'. Spot position is used for yielding a more parallel light beam, increasing the homogeneity of the illuminated area over oblique illumination angles. In both configurations, the light coming from the lamp is not collimated which implies that it reaches the surface of the sample with different angles. In order to eliminate the reflected flux from non-parallel rays, a pure specular aluminium reference sample was measured. Its BRDF represents the angular distribution of the light source and it is therefore deconvoluted from the BRDF of measured samples to get corrected results describing the pure reflectance of the sample surface. The lamp, which produces 1250 lumen, covers the electromagnetic spectrum in the region of 0.35 to 2.5 μm and provides a sufficiently strong signal for the detector. The detector is composed of a light collimator connected to a spectrophotometer through an optical fiber. The spectrophotometer is an Avantes spectrophotometer (AvaSpec-2048) that measures in the wavelength range from 0.2 to 1.1 μm. The motion and positioning of the BULGO components, as well as the operation of the spectrometer, are remotely controlled by a LabVIEW program. The system is therefore able to operate in a full automatized mode.
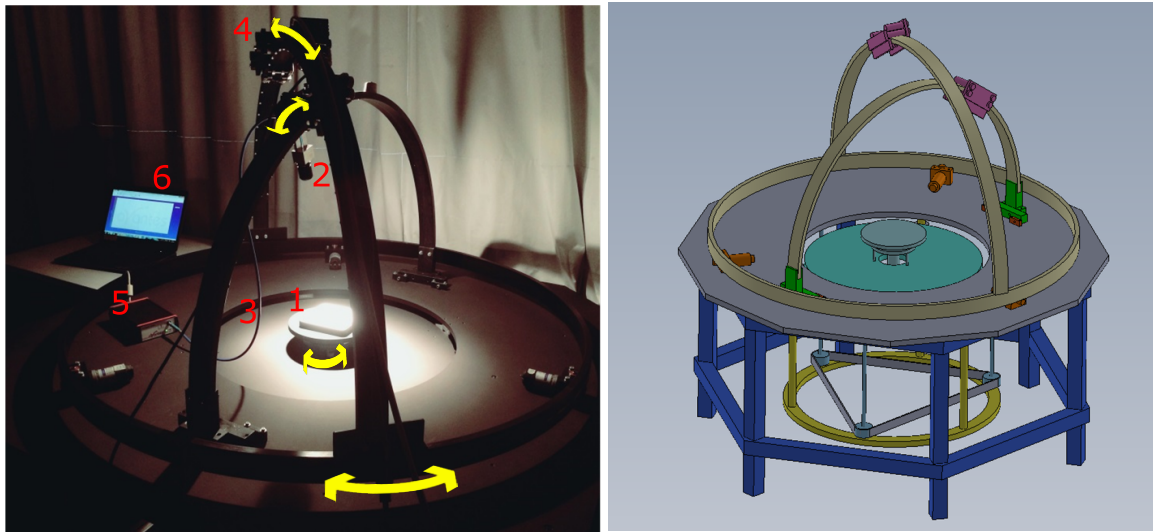
Figure 6.5: *Overview of BULGO gonioreflectometer. 1)Sample holder 2)Collimator 3)Optical fiber 4)Light source 5)Spectrophotometer 6)Labview computer software*

6.4.2 Alignment process and assembly precision

For BRDF measurement, the sample reflected flux collected by the spectrophotometer is compared to the diffuse reference reflectivity (Spectralon, polytetrafluoroethylene). The Spectralon reflectance is the same in all directions. As a result, the measurement conditions of samples and spectralon should be strictly the same. The following section describes the alignment process and its accuracy. The sample holder was adjusted in the horizontal plane in order to align the sample surface with the detector and light horizontal planes. The sample was then placed in the center of the sample holder and its height was adjusted to the same height of the spectralon reference in order to measure under the same geometrical configurations.

The focusing of the setup was performed by collimating the detected signal in the optical fiber. This was done by using a laser pointer connected to the end of the optical fiber (instead of the spectrophotometer). The collimator lens position was then varied until reaching the position where the beam footprint does not dependent on the object distance. Due to the reversibility of the optical path, this step permits to find the collimator focal length to get a collimated beam inside the optical fiber.

The geometric accuracy of the sensor FOV was tested by placing a sharp thin stick in the collimator position. This was accomplished by moving the stick over the zenith arc that supports the detection system while tracing on graphic millimeter paper the maximal deviations of the stick from the center of the sample holder. The observed deviations among the 6 zenith positions (0° to 75°) were smaller than 1.2 cm in both x and y directions. The same procedure was followed for the zenithal and azimuthal rotation of the light source and a maximum deviation of 0.8 cm was found in both cases.

In order to determine the position of the measurement spot on the sample while the

detector is rotating on the zenith arc, the deviation of the collimator FOV across the target was examined by connecting a laser pointer to the end of the optical fiber. The footprint was recorded on millimeter paper for each zenith position of the detector. At zero incidence, the laser footprint on the sample was circular with 1 cm diameter (corresponding to the collimator diameter) that became distinctively elliptical towards higher zenith angles reaching around 3 cm at 75°. This would limit the smallest size of samples that can be measured with BULGO to 3 cm with the condition of surface homogeneity over the detection area. The detector footprint variation impact on the BRDF measurement is canceled by measuring the reference spectralon and the sample with the same geometrical configurations (details in the next paragraph).

6.4.3 Measurements

A two-hour warm-up period was maintained for both the spectrophotometer and the light source before starting any measurement. The warming-up of the spectrophotometer is essential to stabilize dark current while the warming-up of the light source is used to provide a stable and homogeneous intensity distribution over time.

Any sequence of positions can be programmed and executed from a LabVIEW program and the spectrophotometer detects the reflected intensity from the target surface. The full measurement cycle starts by measuring a spectralon reference followed by a dark current measurement of the spectrophotometer (by closing the collimator aperture) and finally a measurement of the sample under the same geometrical configurations as those used for the spectralon. The sample BRDF is then calculated as follows:

$$BRDF = C_f \times \frac{\frac{I_{sample}}{T_{sample}} - \frac{I_{dark}}{T_{dark}}}{\frac{I_{spectralon}}{T_{spectralon}} - \frac{I_{dark}}{T_{dark}}} \qquad (6.2)$$

where I is the intensity of reflected light detected by the spectrophotometer, T is the integration time automatically adjusted by the program to have enough measured intensity and C_f is the spectralon correction factor representing the deviation of the spectralon reflectance from a pure Lambertian.

6.4.4 Validation

Due to the complexity of the BRDF measurement process and the multiplicity of parameters that can influence the precision of the measurement (stability of the light source, stability of the spectrophotometer and its dark measurement, angular positioning on 4 axis....), the measurement error cannot be calculated precisely. However another way to estimate this error is by measuring a specific sample with another goniospectrophotometer and compare the results to BULGO measurements. For that, an inconel tile sample from JET tokamak [200] was measured and compared to the results obtained with the Field Goniometer System FIGOS at the University of Zürich, Switzerland [201]. The measurement position sequence was the following: the sample
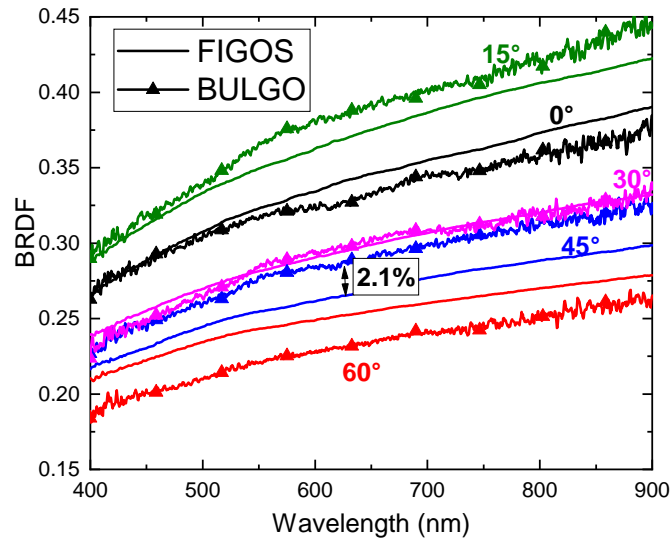
Figure 6.6: *BRDF of JEt inconel tile measured by BULGO and FIGOS goniophotometers*

holder was fixed at 0°, the light position at 10° and 0° in the zenith and azimuth directions respectively and the spectrometer was moved on its zenith supporting arc by a step of 15°. BRDF results obtained for both systems are shown in Figure 6.6. Both devices deliver very similar BRDF values for the same sample with 2.1% maximum difference between both measurements confirming the accuracy of the BULGO system.

6.5 Further characterization techniques

Using BULGO, the bidirectional reflectance of a surface cannot be measured for some angular combinations of the light source and detector. In particular, the 0° light source zenith position over the 0° sensor position is a "blocked" angular combination due to the shadow casting effect on the sample. This artifact is attributed to the sensor being directly underneath the light source. Furthermore, the high grazing angle (in the range of 80 to 90°) cannot be measured due to mechanical restrictions. Different method are thus required to extrapolate the full BRDF at these extreme geometrical configurations.

The 0 degree incidence normal reflectance was measured using a UVvis- near-infrared (NIR) spectrophotometer Varian Cary 5 equipped with a 110 mm diameter integrating sphere under nearly normal incidence (3°20) in the wavelength range of 0.25–2.5 μm [202]. An integrating sphere is designed to collect reflected radiation (diffuse or total) from a sample. It consists of a spherical cavity with a polytetrafluoroethylene coating of high diffuse reflectance on its inner wall. The sample reflects the incident light, which is repeatedly reflected by the spherical cavity's inner wall. This produces diffuse light which enters the detector. The measurement with this spectrophotometer does not allow to measure the pure specular reflectivity part due to the sphere aperture which includes the reflected flux around the specular direction (+/-1°6). To measure

the pure specular reflectivity, a third se up is used consisting of a spectral ellipsometer (Sentech SE 850). This measures the ellipsometric parameters angles (Ψ, Δ) in the range 0.3-2.3 μm for angles of incidence of 45, 55 and 65°. The fit of these six data sets (fitting routine SpectraRay) using a fixed refractive index and absorption model were performed to obtain the optical constants (refractive index n and extinction coefficient k) of the surface as a function of the wavelength. The pure specular reflectivity of the surface at normal incidence was then recalculated using this optical constants [202].
The specular reflectance of samples was also measured using a commercial Bruker Vertex 70 Fourier Transform IR (FTIR), with extended spectral ranges, from 100 cm^{-1} (100 μm) to 20,000 cm^{-1} (0.5 μm). The far and mid-infrared measurements were performed using a combination of broadband beam splitter, high power IR source (globar lamp) and deuterated-triglycine sulfate detector, while for near-IR and visible a combination of quartz beam splitter, high power tungsten lamp and silicon diode detector. A specular reflection/transmission stage (A510/Q-T) with fixed angle of incidence of 11° was used in conjunction with FTIR spectrometer. The beam size was between 1 and 1.5 mm, focused close to the center of the sample. A three dimensional laser scanning with a confocal microscope (3D LSCM, VK-X1000, Keyence) was used to reconstruct the surface topography with an objective lens of 20 times. The surface roughness is calculated using an area of 531 × 708 μm.

6.6 BRDF results for W samples with different surface topography

The plasma facing components are submitted to high heat flux and others erosion-deposition phenomenon causing change of the materials surface state (oxidation) and roughness. This paper focuses on the impact of roughness on BRDF. To investigate the effect of surface roughness on the BRDF, four W samples M100-M103 (shown in Figure 6.7) were prepared by mechanical polishing to achieve several roughness. The results of their measured average roughness are displayed in figure 6.7.

The total and diffuse reflectivity were measured in the range 0.25-2.5 μm. This allows us to plot the specular reflectivity in the inset of Figure 6.8 (dotted line) on the right side. On that same figure is displayed the specular reflectivity measured by a FTIR in the range 0.5-100 μm. A good agreement between both spectrophotometer is demonstrated. Interestingly, for samples M102 and M103, in the range 0.25-4.6 μm the specular reflectivity is not following the corresponding roughness measurements i.e. decrease of specular reflectivity for increasing roughness. In fact, it is possible to calculate the specular reflectivity with the well-known Bennett's formula [203], which correlates the specular reflectivity at normal incidence with the surface roughness:

$$R_s = R_0 \times \exp(\frac{-(4 \times \pi \times RMS)}{\lambda^2})^2 \qquad (6.3)$$

where R$_s$ is the measured specular reflectivity, R$_0$ is the reflectivity of an ideally smooth surface of the same material, RMS is the root mean square roughness, and λ is the wavelength of light. The formula describes a decline of the reflection as a function
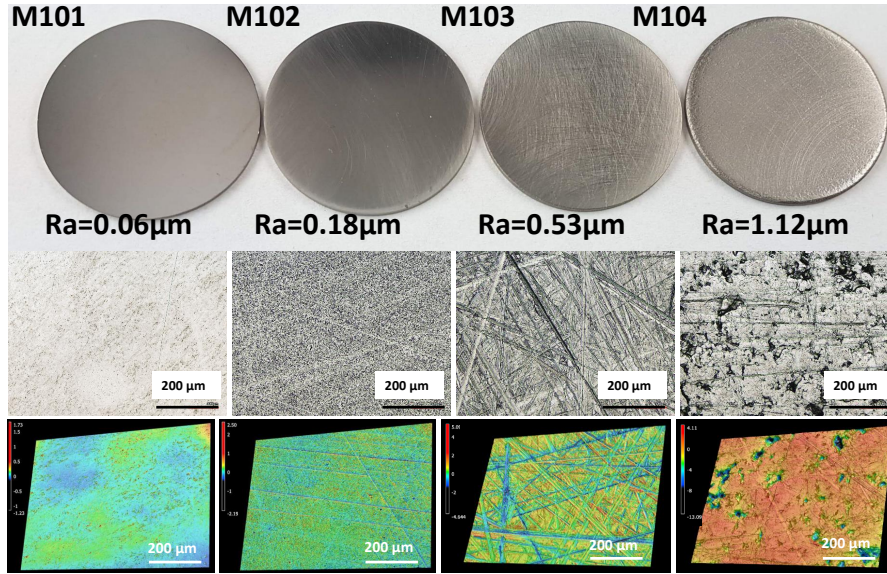
Figure 6.7: *(top) W samples mechanically polished to different roughness and (bottom) their corresponding surface topography measured by Laser Scanning Confocal Microscopy (LSCM)*

of the rms roughness of the surface. At a perfectly smooth surface (RMS=0) the reflectivity equals the square of the Fresnel reflection. Goossens, et.al. [204], described a nearly perfect agreement for smooth samples, for the rougher samples the deviation between experiment and model is larger. Even though the same trend is still visible, the Benett's formula becomes inadequate to predict specular reflectivity as the surfaces become rougher.

This is not matching the measurements below 4.6 μm but for higher wavelength, the measurements follow the Bennett's formula. As seen in Figure 6.7 the scratches on the surface of sample M102 have a width less than 4.6 μm and always contribute to scatter the light below this wavelength. For M103 the surface at high wavelength is affected by large holes (¿50 μm) but for wavelength below 4.6 μm the surface is in comparison to M102 less scratched.

Reflectivity measurements were performed using an ellipsometer at incidence angles of 40°, 60°, 70°, and 75°, for s and p polarized lights on the sample M100. S and p reflectivities are plotted for a wavelength of 0.65 μm in Figure 6.9. The full line in Figure 6.9 represents the s and p components calculated with the theoretical optical constants [205] using the Fresnel equation. The refractive index (n) and extinction coefficient (k) for this film are 2.4 and 2.9, respectively, at 0.65 μm. In Figure 6.9 the value at 0° is the one measured with the spectrophotometer (Cary setup). The measured value with Cary is quite in agreement with ellipsometer measurement. At 90° the value is extracted from the calculated curve. This value is equal to 100% indicating that the material surface is fully specular at grazing angle.

For all tested surfaces, the BRDFs were measured at both the plane of incidence ($\phi_i=\phi_r=0$) and in the orthogonal plane ($\phi_i=0$; $\phi_r=90$) and over the reflection hemisphere (variable θ_i and θ_r). In this way, it is shown that the W samples BRDF is
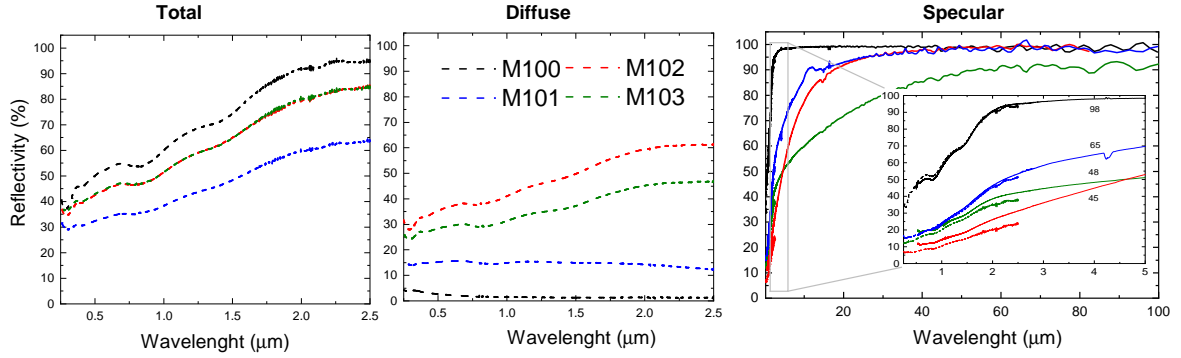
Figure 6.8: *Total, diffuse and specular reflectivities measured for the W samples M100-M103. Reflectivity of W samples measured by the integrating sphere (dashed lines) and FTIR (solid lines). In the inset are plotted both measurement in the range 0.25 to 5 μm. Reflectivity parentage at 4 μm are displayed in the inset.*

isotropic i.e. it stays the same when the sample is rotated by 90° around the normal.
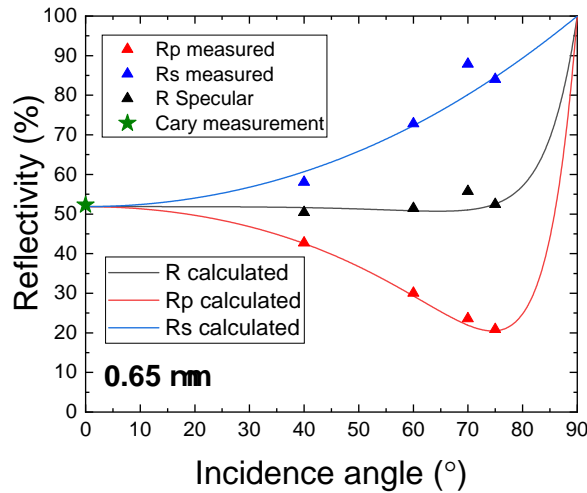
Figure 6.9: *M100 reflectivities at 40°, 60°, 70°, and 80° for s and p polarizations at 0.65 μm (triangle symbol). The solid lines represent the s and p components fitted from n and k.*

BRDF results for the four W surfaces are presented in figure 6.10. The BRDF is plotted versus the detection angle for different incident angles at a fixed wavelength of 0.9 μm. The black line curves represent the measurement results while the red line is for the corrected measurement by subtracting the effect of a non collimated light source. All results were fitted with a Gauss function centred at the specular direction ($\theta_i=\theta_r$) represented in the figure by a dashed line. No constant reflectance component was measured. This indicates that both samples have only a pure Gaussian reflectance around the specular and do not present any Lambertian (or diffuse) component (presented by the offset in Figure 6.2). Besides, for all samples, the BRDF

increases towards grazing angles.
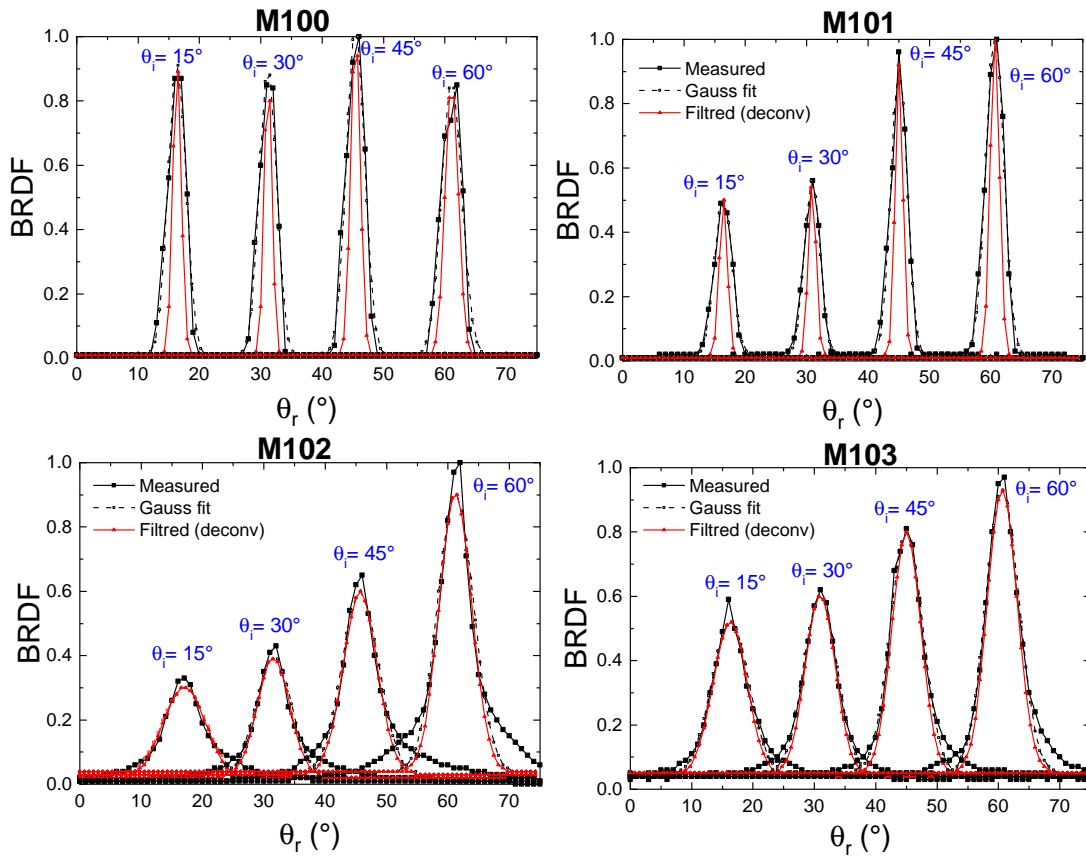
Figure 6.10: *W samples BRDF results for λ=0.9 μm and variable incident angle*
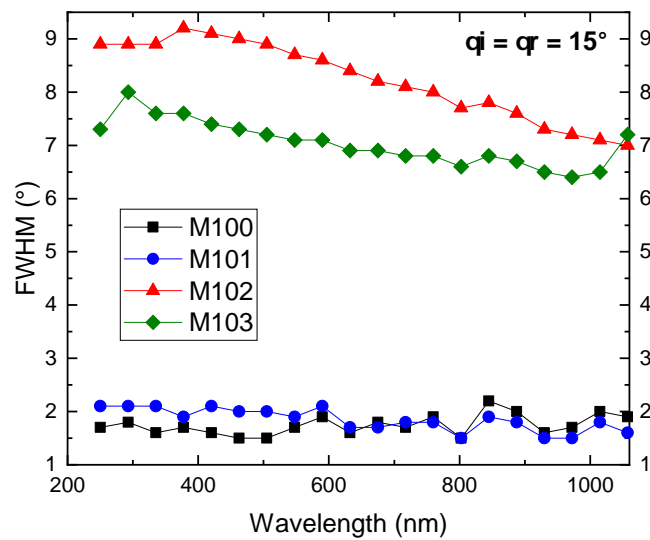
Figure 6.11: *W samples FWHM variation as a function of the wavelength (data extracted from figure 6.10).*

The Gaussian Full Width at Half Maximum (FWHM) at 15° incidence angle is plotted in Figure 6.11 for wavelength values ranging from 0.25 to 1.1 μm. The FWHM stayed almost constant in the entire range and all values are below 10 degree. As explained previously for the diffuse and roughness correlation of the M102 and M103, the FWHM of the latest is lower than M102. For samples M100 and M101, representing the smallest Ra values (0.015 and 0.045 μm respectively) the FWHM is around 2°. This value is around 4-5 times higher for the rough samples M102 and M103.

Su et. Al. [206], adopted in their BRDF model the optical roughness instead of surface roughness. The optical roughness (σ_{opt}) can be expressed as the ratio between surface roughness (σ_0) and wavelength (λ):

$$\sigma_{opt} = \frac{\sigma_0}{\lambda} \tag{6.4}$$

According to both studies [206] and [207], the surface can be classified in 3 regions following to the surface roughness: (i) Specular region when $0 < \sigma_{opt} < 0.2$ for which Bennett Law can be applied to get directional reflectivity (ii) Intermediate region when $0.2 < \sigma_{opt} < 1$ or which approximate models is needed to describe BRDF (iii) Geometric region when $\sigma_{opt} > 1$ for which geometric optics law can be used. Su et. Al. [206] presented a plot of the BRDF for five incidence angles and three optical roughness values: 0.1, 0.2 and 0.3 for a pure specular surface. As seen in figure 7 reported by Su et al. [206], the maximum of the BRDF value is increasing for increasing angle and the FHWM is increasing for higher σ_{opt}. For = 0.9 μm (wavelength at which the BRDF is presented in Figure 6.10), the σ_{opt} values are 0.063, 0.2, 0.59 and 1.24 for M100, M101, M102 and M103, respectively. Only for M100 and M101 σ_{opt} is in the range 0-0.2 which most theoretical models assume the reflection of incident radiation is specular [207].

6.7 Emissivity model

Using Kirchhoff's Law, the spectral normal emissivity of W reference samples is directly calculated from spectral directional hemispherical total reflectance measured by the integrating sphere and FTIR (presented in Figure 6.8). Results are shown is Figure 6.12. As can be seen, the emissivity increases with roughness for the entire wavelength range. The only exception is for the samples M101. That would suggest that, the roughness parameter is not the only parameter that can impact the thermal optical behaviour of a material. Additional effect including the machining process and presence of surface non uniformity can alter the emissivity model. For all samples, the emissivity decreases with increasing wavelength, in particular a drop by a factor 5 from the visible to IR range is measured for the reference samples. The spectral directional emissivity can be also deduced from BDRF measurement using Kirchhoff's law: ϵ'=1-$\rho'^{\cap}$ ($\cap$ for hemispherical). The angular dependence is described with a cosine n power model with n=1 for Lambertian distribution, n>1 for directional emission and n<1 for grazing emission. The n coefficient results are presented in Figure 6.13. For samples M101, M102 and M103, the n coefficient is found lower than 1 in the visible range favouring
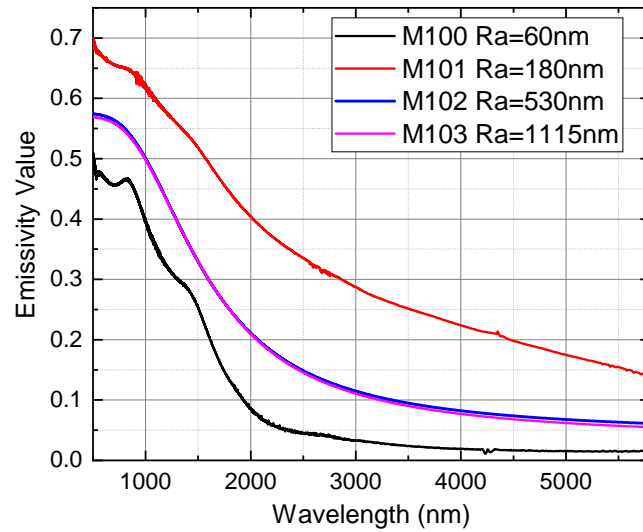
Figure 6.12: *Spectral normal emissivity as a function of wavelength for M100 to M103 samples*
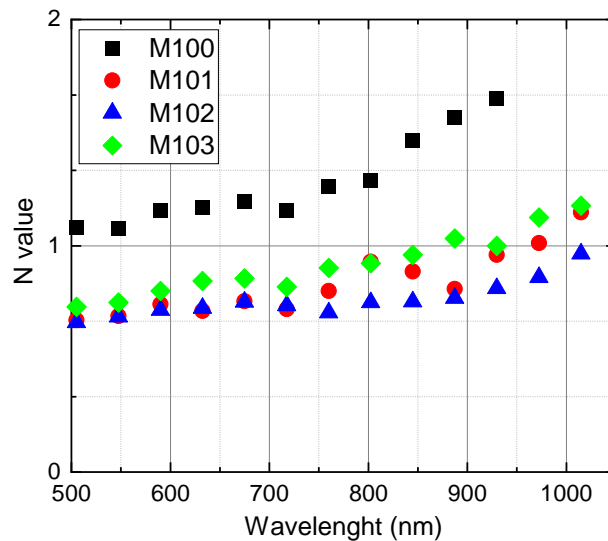
Figure 6.13: *W reference samples n factor fitted from the n cosine power model of the directional emissivity.*

grazing angle.

6.8 Simulation results

The main infrared source in tokamak comes from the heat flux deposited on the plasma facing components and in particular on the lower divertor which is situated at the bottom of the vacuum vessel and receives the maximum heat flux up to 10 MWm² (steady state) and 20 MW/m² (slow transients). The plasma is transparent in IR

WEST components	Materials	MEASUREMENT				Parameters used for simulation		
		Ra (μm)	Emissivity @ 4 μm	N power Emissivity	Reflectance model @ 2 μm	Emissivity	N power emissivity	Reflectance
Lower Divertor	W-coated graphite	1.8 / 1.1 (M103)	0.03 / 0.09 (M103)	N=1.5	Specular but with max R shifted / Highly Specular (8°)	0.1	1	Specular (7°) / Specular (7°)
Baffle	W-coated graphite	-	-		-	0.1	1	Specular (7°)
Inner bumper	W-coated CFC (PVD)	3.2 / 6.2	0.16 / 0.09	–	Specular but with max R shifted	0.15	1	Specular (7°)
Outer bumper (LPA)	W-coated CFC (PVD)	3200 nm	0.16	–		0.15	1	Specular (7°)
Upper divertor	W-coated CuCrZr	-	-	–	-	0.1	1	Specular (7°)
Heating antenna bumper	W-coated CFC (VPS)	-	-	-	-	0.15	1	Specular (7°)

Table 6.1: *Input parameters for the SPEOS simulation.*

range. In the simulation, only the IR source coming from the divertor is considered (turned on) to assess the reflections coming from these components.

Figure 6.14 compares the experimental image of WEST Wide Angle Tangential view with the simulated ones by considering two scenarios of a full diffuse surface for in vessel components (in emission and reflectance) and high specular surface roughly adjusted to W sample measurements (M103). Table 6.1 summarizes the parameters roughly adjusted to laboratory measurement used as input of photonic simulation. Reflections features on upper divertor is well reproduced proving that specular reflectance fits roughly with experimental images in accordance with W sample measurements. Further analysis of the experimental data shows that the emission model is not (spatially) uniform on the same components during the WEST experimental campaign (depending to erosion/deposition phenomenon by plasma). Further simulation should take into account the emissivity variation and check if the associated reflectance model (BRDF) is also affected.
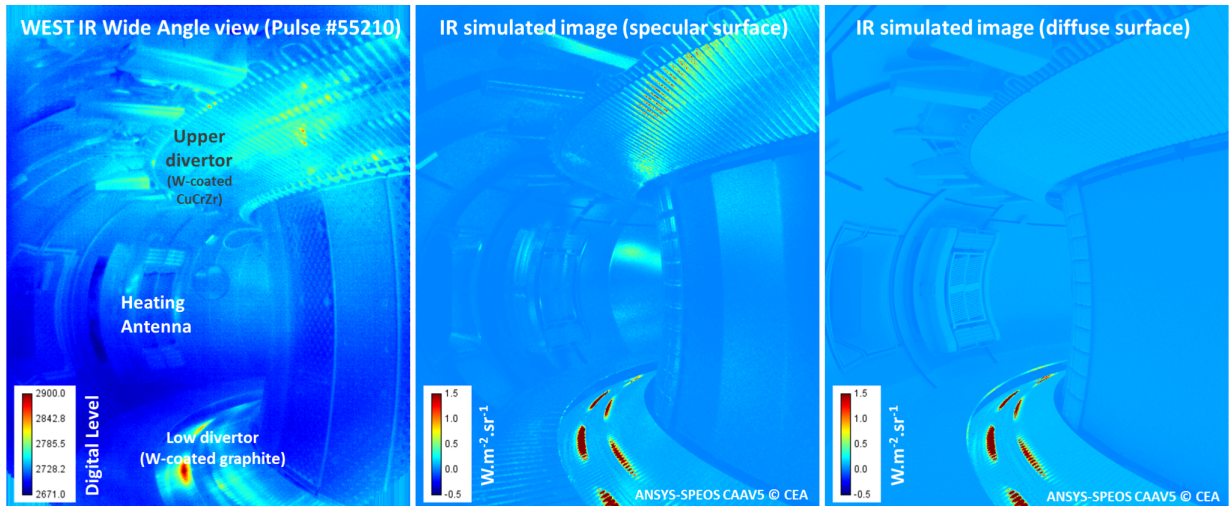
Figure 6.14: *(Left) Infrared experimental image of WEST Wide Angle Tangential View [3300-3400 nm filter band] (Middle) Simulated image assuming high specular surface further to W sample measurement in laboratory and (Right) Simulated image assuming all diffuse surface.*

6.9 Summary

This chapter presented an accurate experimental tool available for the optical properties measurements of PFC materials mainly the bidirectional reflectance distribution function. BULGO was developed for this purpose and showed, after calibration, good accuracy in comparison to another setup. BRDF first results of the W samples with different surface topography show that their reflectance is represented by a pure Gaussian component around the specular direction with small angular width (less than 10°). The reflectance coefficient was correctly fitted with a cosine n power model. On the other hand, the Gaussian FWHM was found almost constant with the wavelength. It is found that roughness has an impact on BDRF of samples but it does not represent the only factor to describe it. If diffuse part of reflectance increases with roughness, others parameters as cracks, machining, oxidation modify the emissivity value.

Experimental data were implemented in the ray-tracing software SPEOS in order to have a better interpretation of the synthetic images of WEST camera and distinguish the patterns caused by the reflection of W divertor. By comparing simulated and experimental images in WEST, the experimental results were confirmed including the Gaussian response and the angular dependence of reflectance of the W divertor material.

Conclusion

THE formation of ammonia from an N_2/H_2 RF plasma both with and without tungsten and stainless steel catalysts for different nitrogen initial fraction was investigated. Results confirmed that the presence of the catalytic surface highly increases the ammonia formed percentage. This indicates that both W divertor low temperature areas and SS shaded areas are efficient towards ammonia synthesis from species already excited and/or dissociated in the plasma. Using a combination of RF low pressure plasma and a W surface as a catalyst, unprecedented ammonia yields up to 32 % at 25/75 % of N_2/H_2 were obtained, surpassing consequently the yields reported in the literature for different plasma discharges and different catalytic surfaces. So far, it is not clear what is the exact factor that drastically enhanced the formation yield in our experiment compared to previous research. It could be associated to the combination of different experimental conditions: low pressure, low temperature, high dissociation rate in the plasma and enhanced photo-dissociation of nitrogen by the Lyman lines of dissociated hydrogen. Although undesirable in the nuclear fusion reactor, these results open the door to an attractive option for an industry adapted ammonia formation process as an alternative for the Haber-Bosch process. However, it is worth mentioning that the energy yield is still very limited compared to Haber-Bosch process and need therefore to be highly improved. The optimization of the plasma parameters as well as the catalytic surface could lead to a better formation and energy yield. Furthermore, by means of X-ray photo-electron spectroscopy, we could demonstrate experimentally the interaction of species from the plasma with the catalyst surface. By investigating both the tungsten and the nitrogen binding energies to identify the formed species, we proposed a formation pathway of ammonia through Eley-Rideal mechanism between adsorbed nitrogen and hydrogen from the gas phase.

The rise of the surface temperature resulted in a decrease in the ammonia formed percentage due to two major factors. For high temperatures (above 650 K and 830 K for SS and W, respectively), thermal decomposition of ammonia is predominant. For lower temperature range, the major factor is the formation of stables nitrides which do not react further with hydrogen to form NH_2 and NH_3. These results imply that in the

tokamak, the high temperature active area of the W divertor and its surrounding will not contribute much to the ammonia production. As the NH_3 formation is favored by low temperature, a high contribution from SS pumping ducts and the plasma shaded areas is expected.

It was also shown that the addition of helium and argon to the nitrogen-hydrogen plasma have opposite effects on the ammonia production. While He effectively decreases the percentage of NH_3 by acting as a barrier for the surface processes, argon impacts more the plasma processes by increasing the active nitrogen species in the plasma and, as a consequence, the percentage of ammonia formed. This suggests that the presence of He as an intrinsic impurity in the fusion plasma might help to decrease the ammonia production and could further be used in a mixture with the nitrogen seeding gas. In contrary, argon has not the expected effect. Ar can, therefore, be added only as a pure gas for the enhancement of core and divertor radiation in the case where elevated main chamber radiation is desired as well.

NH_3 adsorption/desorption cycles performed on bare Au and on W, SS, B and Be coated quartz crystals showed that the adsorption process is pressure and material dependent. This material-dependent sticking in the fusion device would lead to a non-uniform distribution of adsorbed tritiated ammonia in ITER (highest on the W divertor and SS pump ducts).

The amount of NH_3 molecules bound to the surfaces was found to increase with increasing pressures for B, SS and W. Regarding Au and Be surfaces, few ML were measured at high pressures (500 to 800 mbar). No saturation was observed up to 800 mbar for W, B, and SS. Therefore, the adsorption of tritiated ammonia on the fusion device wall divertor and pumping ducts would be cumulative from one operational cycle (issues with tritium limit in the device) especially on the stainless steel surfaces which are not directly exposed to plasma impact.

In order to explain the difference in the adsorption between materials, two types of interactions were presented. A strong adsorption on W, SS and B due to electron sharing between the NH_3 and the surface, leading to a true chemical bond. This strong interaction led also to the formation of multilayers through H bonds. In this case, the desorption of the gas was not complete and a continuous decomposition of the NH_3 on these surfaces was measured by in vacuo XPS performed during several time intervals after the exposure.

On the other hand, a weak NH_3 adsorption is assumed on Au and Be and explained mainly by the H bond with O present on the surface. For those two materials, the desorption was complete according to QMB measurements and confirmed through XPS analysis. The total desorption shown on Au makes it a possible option as a coating material for the low neutron heat load SS pumping ducts to decrease ammonia and therefore tritium retention on these surfaces.

Plasma first mirror cleaning was the main focus of the second topic of this dissertation. Rh and Mo mirrors were contaminated with Be, either deposited in laboratory or from exposure in JET-ILW that resulted in deposits containing up to 1.5 at.% of W. All contaminated mirrors were treated in the Beryllium laboratory at the INFLPR, which allows to work with toxic Be, using RF plasma with D_2 at different ion energies. Two

sputtering regimes were investigated, namely physical and chemically assisted physical sputtering at respectively high (220 eV) and low (60 eV) ion energy. It was possible to remove all the Be contaminated films, which were deposited with magnetron sputtering, with low and high ion energy D_2 cleaning while it was only possible to fully remove deposits from JET-ILW at 220 eV. At lower energy, the fraction of W initially present in the deposit was not sputtered and led to a W-enrichment of the surface, acting as a protective layer against sputtering.

Although the reflectivity of all samples increased (except for JET-ILW cleaned at low ion energy), an additional step with Ar was needed for samples cleaned at 220 eV due to the formation of stable Rh or Mo deuterides. With this additional step, the pristine reflectivities were fully recovered without any noticeable damage to the surface, e.g. no increase of the diffuse reflectivity.

Yet, in order to employ D_2 alone in ITER for cleaning of all kind of deposits, additional points need to be cleared :
- Can the formation of stable deuterides be avoided for Mo and Rh based FMs?
- What is the maximum amount of W that contaminants deposit can contain to avoid the formation of a protective layer and hinder further cleaning?
Only when those questions are addressed can D_2 be considered for an ITER FMs cleaning regime where the entire vessel is filled with D_2 and all mirrors are cleaned simultaneously without damaging their surface.

The last part of this manuscript was devoted to the question of wall reflection in metallic tokamak. An accurate experimental tool available for the optical properties measurements of PFC materials mainly the bidirectional reflectance distribution function was presented. BULGO was developed for this purpose and showed, after calibration, good accuracy in comparison to another setup. BRDF first results of the W samples with different surface topography show that their reflectance is represented by a pure Gaussian component around the specular direction with small angular width (less than 10°). The reflectance coefficient was correctly fitted with a cosine n power model. On the other hand, the Gaussian FWHM was found almost constant with the wavelength. It is found that roughness has an impact on BDRF of samples but it does not represent the only factor to describe it. If diffuse part of reflectance increases with roughness, others parameters as cracks, machining, oxidation modify the emissivity value.

Experimental data were implemented in the ray-tracing software SPEOS in order to have a better interpretation of the synthetic images of WEST camera and distinguish the patterns caused by the reflection of W divertor. By comparing simulated and experimental images in WEST, the experimental results were confirmed including the Gaussian response and the angular dependence of reflectance of the W divertor material.

Overall, the present dissertation has tackled several materials related topics in tokamaks and has made several noteworthy contributions to nuclear fusion research.

Bibliography

[1] De Temmerman, G. & Pitts, R. Joint wpjet 2 and wppfc eurofusion annual meeting (2015). *Culham, UK* .

[2] de Castro, A., Alegre, D. & Tabarés, F. Influence of residence time and helium addition in the ammonia formation on tungsten walls in n2h2 glow discharge plasmas. *Nuclear Materials and Energy* **12**, 399–404 (2017).

[3] Al-Shammeri, K. K. & Saleh, J. M. Adsorption and decomposition of ammonia on metal films of nickel, palladium, tungsten and aluminum. *The Journal of Physical Chemistry* **90**, 2906–2910 (1986).

[4] Jena, P., Khanna, S. & Rao, B. *Physics and chemistry of finite systems: from clusters to crystals*, vol. 374 (Springer Science & Business Media, 2013).

[5] De Temmerman, G. *et al.* Efficiency of thermal outgassing for tritium retention measurement and removal in ITER. *Nuclear Materials and Energy* (2016).

[6] Plotting nuclear fusion cross sections. `https://scipython.com/blog/plotting-nuclear-fusion-cross-sections/`. Accessed: 2018-07-10.

[7] Wright, J. C. Lecture 20: Fusion as a future energy source? URL `https://ocw.mit.edu/courses/nuclear-engineering/22-081j-introduction-to-sustainable-energy-fall-2010/lectures-and-readings/MIT22_081JF10_lec15b.pdf`.

[8] Kikuchi, M., Lackner, K. & Tran, M. Q. Fusion physics (2012).

[9] The iter tokamak. `https://www.iter.org/mach`.

[10] Pitts, R. *et al.* Physics conclusions in support of iter w divertor monoblock shaping. *Nuclear Materials and Energy* **12**, 60–74 (2017).

[11] Matthews, G. Plasma operation with an all metal first-wall: Comparison of an iter-like wall with a carbon wall in jet. *Journal of Nuclear Materials* **438**, S2 – S10 (2013). Proceedings of the 20th International Conference on Plasma-Surface Interactions in Controlled Fusion Devices.

[12] Kallenbach, A. *et al.* Impurity seeding for tokamak power exhaust: from present devices via iter to demo. *Plasma Physics and Controlled Fusion* **55**, 124041 (2013).

[13] Schweinzer, J. *et al.* Confinement of improved H-modes in the all-tungsten ASDEX Upgrade with nitrogen seeding. *Nuclear Fusion* **51**, 113003 (2011).

Bibliography

[14] Giroud, C. *et al.* Impact of nitrogen seeding on confinement and power load control of a high-triangularity JET ELMy H-mode plasma with a metal wall. *Nuclear fusion* **53**, 113025 (2013).

[15] Neuwirth, D., Rohde, V., Schwarz-Selinger, T. & Team, A. U. Formation of ammonia during nitrogen-seeded discharges at ASDEX Upgrade. *Plasma Physics and Controlled Fusion* **54**, 085008 (2012).

[16] Rohde, V., Oberkofler, M. *et al.* Ammonia production in nitrogen seeded plasma discharges in ASDEX Upgrade. *Journal of Nuclear Materials* **463**, 672–675 (2015).

[17] Oberkofler, M. *et al.* Nitrogen retention mechanisms in tokamaks with beryllium and tungsten plasma-facing surfaces. *Physica Scripta* **2016**, 014077 (2016).

[18] Oberkofler, M. *et al.* Plasma–wall interactions with nitrogen seeding in all-metal fusion devices: Formation of nitrides and ammonia. *Fusion engineering and design* **98**, 1371–1374 (2015).

[19] Drenik, A. *et al.* Detection of ammonia by residual gas analysis in aug and jet. *Fusion Engineering and Design* **124**, 239–243 (2017).

[20] Drenik, A. *et al.* Evolution of nitrogen concentration and ammonia production in n 2-seeded h-mode discharges at asdex upgrade. *Nuclear Fusion* (2019).

[21] Tabarés, F. *et al.* Tritium control techniques in iter by ammonia injection. *Journal of Nuclear Materials* **415**, S793–S796 (2011).

[22] Oberkofler, M. *et al.* First nitrogen-seeding experiments in jet with the iter-like wall. *Journal of Nuclear Materials* **438**, S258–S261 (2013).

[23] Romanelli, S. G. *et al.* Gas analyses of the first complete jet cryopump regeneration with iter-like wall. *Physica scripta* **2014**, 014068 (2014).

[24] Laguardia, L. *et al.* Influence of he and ar injection on ammonia production in n2/d2 plasma in the medium flux gym device. *Nuclear Materials and Energy* **12**, 261–266 (2017).

[25] Bohmeyer, W. *et al.* The scavenger effect–does it work? *Journal of Nuclear Materials* **390**, 560–563 (2009).

[26] Tabarés, F. Tritium inventory control during iter operation under carbon plasma-facing components by nitrogen-based plasma chemistry: a review. *Plasma Sources Science and Technology* **22**, 033001 (2013).

[27] Bartholomew, C. H. & Farrauto, R. J. *Fundamentals of industrial catalytic processes* (John Wiley & Sons, 2011).

[28] Chorkendorff, I. & Niemantsverdriet, J. W. *Concepts of modern catalysis and kinetics* (John Wiley & Sons, 2017).

[29] Schlögl, R. & Jennings, J. Catalytic ammonia synthesis. In *Fundamentals and Practice*, 19–108 (Plenum Press New York, 1991).

[30] Smil, V. Detonator of the population explosion. *Nature* **400**, 415 (1999).

[31] Ertl, G. Elementary steps in ammonia synthesis: The surface science approach. *Catalytic ammonia synthesis: fundamentals and practice* 109–132 (1991).

[32] Tas, M. A. *Plasma-induced catalysis: a feasibility study and fundamentals.* Ph.D. thesis (1995).

[33] Feng, X., Liu, H., He, C., Shen, Z. & Wang, T. Synergistic effects and mechanism of a non-thermal plasma catalysis system in volatile organic compound removal: a review. *Catalysis Science & Technology* **8**, 936–954 (2018).

[34] Gicquel, A., Cavadias, S. & Amouroux, J. Heterogeneous catalysis in low-pressure plasmas. *Journal of Physics D: Applied Physics* **19**, 2013 (1986).

[35] Rapakoulias, D., Cavadias, S. & Mataras, D. Heterogeneous catalysis in interaction of plasma excited species with surfaces. *ChemInform* **26**, no–no (1995).

[36] Chen, H. L., Lee, H. M., Chen, S. H., Chao, Y. & Chang, M. B. Review of plasma catalysis on hydrocarbon reforming for hydrogen production—interaction, integration, and prospects. *Applied Catalysis B: Environmental* **85**, 1–9 (2008).

[37] Neyts, E. C. Plasma-surface interactions in plasma catalysis. *Plasma chemistry and plasma processing* **36**, 185–212 (2016).

[38] Rettner, C. & Stein, H. Effect of vibrational energy on the dissociative chemisorption of n2 on fe (111). *The Journal of chemical physics* **87**, 770–771 (1987).

[39] Rettner, C., Pfnür, H., Stein, H. & Auerbach, D. Promotion of dissociative chemisorption with vibrational and translational energy. *Journal of Vacuum Science & Technology A: Vacuum, Surfaces, and Films* **6**, 899–901 (1988).

[40] Por, E., Haase, G., Citri, O., Kosloff, R. & Asscher, M. Effect of molecular energy content on the dissociative chemisorption of n2 on re (0001). *Chemical physics letters* **186**, 553–560 (1991).

[41] Romm, L., Katz, G., Kosloff, R. & Asscher, M. Dissociative chemisorption of n2 on ru (001) enhanced by vibrational and kinetic energy: Molecular beam experiments and quantum mechanical calculations. *The Journal of Physical Chemistry B* **101**, 2213–2217 (1997).

[42] Katz, G. & Kosloff, R. Temperature dependence of nitrogen dissociation on metal surfaces. *The Journal of chemical physics* **103**, 9475–9481 (1995).

[43] Srim - the stopping and range of ions in matter software. `http://www.srim.org/`.

[44] Eckstein, W., Garcia-Rosales, C., Roth, J. & László, J. Threshold energy for sputtering and its dependence on angle of incidence. *Nuclear Instruments and Methods in Physics Research Section B: Beam Interactions with Materials and Atoms* **83**, 95–109 (1993).

[45] Neyts, E. C., Ostrikov, K., Sunkara, M. K. & Bogaerts, A. Plasma catalysis: synergistic effects at the nanoscale. *Chemical reviews* **115**, 13408–13446 (2015).

Bibliography

[46] Poppe, J. *et al.* Electrochemical promotion of catalytic co oxidation on pt/ysz catalysts under low pressure conditions. *Physical Chemistry Chemical Physics* **1**, 5241–5249 (1999).

[47] Shah, J., Wang, W., Bogaerts, A. & Carreon, M. L. Ammonia synthesis by radio frequency plasma catalysis: revealing the underlying mechanisms. *ACS Applied Energy Materials* **1**, 4824–4839 (2018).

[48] Carrasco, E., Jiménez-Redondo, M., Tanarro, I. & Herrero, V. J. Neutral and ion chemistry in low pressure dc plasmas of h 2/n 2 mixtures: routes for the efficient production of nh3 and nh 4+. *Physical Chemistry Chemical Physics* **13**, 19561–19572 (2011).

[49] Body, T. A., Cousens, S., Kirby, J. & Corr, C. S. A volume-averaged model of nitrogen-hydrogen plasma chemistry to investigate ammonia production in a plasma-surface-interaction device. *Plasma Physics and Controlled Fusion* (2018).

[50] Operating manual and programming reference: Models rga100, rga200, and rga300 residual gas analyzer. `https://www.thinksrs.com/downloads/pdfs/manuals/RGAm.pdf`.

[51] Eren, B. *et al.* Hydrogen-induced buckling of gold films. *Journal of Physics D: Applied Physics* **47**, 025302 (2013).

[52] Malyshev, O. & Middleman, K. In situ ultrahigh vacuum residual gas analyzer "calibration". *Journal of Vacuum Science & Technology A: Vacuum, Surfaces, and Films* **26**, 1474–1479 (2008).

[53] Ellefson, R., Morgan, F. & Anderson, B. Central gas analysis laboratory with remote sampling. *Journal of Vacuum Science & Technology A: Vacuum, Surfaces, and Films* **4**, 306–309 (1986).

[54] Basford, J. A. *et al.* American vacuum society recommended practice; recommended practice for the calibration of mass spectrometers for partial pressure analysis. *J. Vac. Sci. Technol. A* **11** (1993).

[55] Ellefson, R. E., Cain, D. & Lindsay, C. N. Calibration of mass spectrometers for quantitative gas mixture analysis. *Journal of Vacuum Science & Technology A: Vacuum, Surfaces, and Films* **5**, 134–139 (1987).

[56] Eren, B. *et al.* The effect of low temperature deuterium plasma on molybdenum reflectivity. *Nuclear Fusion* **51**, 103025 (2011).

[57] Hesse, R., Chassé, T. & Szargan, R. Peak shape analysis of core level photoelectron spectra using UNIFIT for WINDOWS. *Fresenius' journal of analytical chemistry* **365**, 48–54 (1999).

[58] Doniach, S. & Sunjic, M. Many-electron singularity in x-ray photoemission and x-ray line spectra from metals. *Journal of Physics C: Solid State Physics* **3**, 285 (1970).

[59] Shirley, D. A. High-resolution X-ray photoemission spectrum of the valence bands of gold. *Physical Review B* **5**, 4709 (1972).

[60] Scofield, J. Hartree-Slater subshell photoionization cross-sections at 1254 and 1487 eV. *Journal of Electron Spectroscopy and Related Phenomena* **8**, 129–137 (1976).

[61] Hong, J. *et al.* Kinetic modelling of nh3 production in n2–h2 non-equilibrium atmospheric-pressure plasma catalysis. *Journal of Physics D: Applied Physics* **50**, 154005 (2017).

[62] Uyama, H. & Matsumoto, O. Reaction scheme of ammonia formation in microwave-discharge from quenching reactions of nh radicals by hydrogen. *Denki Kagaku* **61**, 925–926 (1993).

[63] Steen, M. L., Kull, K. R. & Fisher, E. R. Comparison of surface interactions for nh and nh 2 on polymer and metal substrates during nh 3 plasma processing. *Journal of applied physics* **92**, 55–63 (2002).

[64] Hong, J., Prawer, S. & Murphy, A. B. Plasma catalysis as an alternative route for ammonia production: Status, mechanisms, and prospects for progress. *ACS Sustainable Chemistry & Engineering* **6**, 15–31 (2017).

[65] Uyama, H. & Matsumoto, O. Synthesis of ammonia in high-frequency discharges. ii. synthesis of ammonia in a microwave discharge under various conditions. *Plasma Chemistry and Plasma Processing* **9**, 421–432 (1989).

[66] Uyama, H. & Matsumoto, O. x. In *Proceedings of the Tenth International Symposium on Plasma Chemistry (ISPC-10), Bochum, Germany*, sect. 2.3–10, 1 (1991).

[67] Patil, B. *Plasma (catalyst)-assisted nitrogen fixation: reactor development for nitric oxide and ammonia production.* Ph.D. thesis (2017).

[68] Schüth, F., Palkovits, R., Schlögl, R. & Su, D. S. Ammonia as a possible element in an energy infrastructure: catalysts for ammonia decomposition. *Energy & Environmental Science* **5**, 6278–6289 (2012).

[69] Ganley, J. C., Thomas, F., Seebauer, E. & Masel, R. I. A priori catalytic activity correlations: the difficult case of hydrogen production from ammonia. *Catalysis Letters* **96**, 117–122 (2004).

[70] Tardio, S., Abel, M.-L., Carr, R. H., Castle, J. E. & Watts, J. F. Comparative study of the native oxide on 316l stainless steel by xps and tof-sims. *Journal of Vacuum Science & Technology A: Vacuum, Surfaces, and Films* **33**, 05E122 (2015).

[71] Mehta, P. *et al.* Overcoming ammonia synthesis scaling relations with plasma-enabled catalysis. *Nature Catalysis* **1**, 269 (2018).

[72] Uyama, H. & Matsumoto, O. Synthesis of ammonia in high-frequency discharges. *Plasma chemistry and plasma processing* **9**, 13–24 (1989).

[73] Amorim, J., Baravian, G. & Sultan, G. Absolute density measurements of ammonia synthetized in n2–h2 mixture discharges. *Applied physics letters* **68**, 1915–1917 (1996).

[74] Mizushima, T., Matsumoto, K., Ohkita, H. & Kakuta, N. Catalytic effects of metal-loaded membrane-like alumina tubes on ammonia synthesis in atmospheric pressure plasma by dielectric barrier discharge. *Plasma Chemistry and Plasma Processing* **27**, 1–11 (2007).

Bibliography

[75] Gómez-Ramírez, A., Cotrino, J., Lambert, R. & González-Elipe, A. Efficient synthesis of ammonia from n2 and h2 alone in a ferroelectric packed-bed dbd reactor. *Plasma Sources Science and Technology* **24**, 065011 (2015).

[76] Kim, H.-H., Teramoto, Y., Ogata, A., Takagi, H. & Nanba, T. Atmospheric-pressure nonthermal plasma synthesis of ammonia over ruthenium catalysts. *Plasma Processes and Polymers* **14**, 1600157 (2017).

[77] Akay, G. & Zhang, K. Process intensification in ammonia synthesis using novel coassembled supported microporous catalysts promoted by nonthermal plasma. *Industrial & Engineering Chemistry Research* **56**, 457–468 (2017).

[78] Gómez-Ramírez, A., Montoro-Damas, A. M., Cotrino, J., Lambert, R. M. & González-Elipe, A. R. About the enhancement of chemical yield during the atmospheric plasma synthesis of ammonia in a ferroelectric packed bed reactor. *Plasma Processes and Polymers* **14**, 1600081 (2017).

[79] Perillo, R. *et al.* Studying the influence of nitrogen seeding in a detached-like hydrogen plasma by means of numerical simulations. *Plasma Physics and Controlled Fusion* **60**, 105004 (2018).

[80] Yaala, M. B. *et al.* Quartz micro-balance and in situ xps study of the adsorption and decomposition of ammonia on gold, tungsten, boron, beryllium and stainless steel surfaces. *Nuclear Fusion* **58**, 106012 (2018).

[81] Bchir, O. J. *et al.* Effect of nh 3 on film properties of mocvd tungsten nitride from cl4 (ch 3 cn) w (n ipr). *Journal of The Electrochemical Society* **151**, G697–G703 (2004).

[82] Wang, D., Chen, J., Zhang, H. & Huang, N. Influence of ionic species on phase formation in ion mixing of carbon films on tungsten. *Nuclear Instruments and Methods in Physics Research Section B: Beam Interactions with Materials and Atoms* **171**, 465–469 (2000).

[83] Yang, Y.-W., Wu, J.-B., Wang, J., Lin, Y.-F. & Chiu, H.-T. Thermal decomposition mechanisms of tungsten nitride cvd precursors on cu (1 1 1). *Surface science* **600**, 743–754 (2006).

[84] Zhang, H., Wang, D. & Huang, N. The effect of nitrogen ion implantation on tungsten surfaces. *Applied surface science* **150**, 34–38 (1999).

[85] Egawa, C., Naito, S. & Tamaru, K. Adsorption and decomposition of ammonia on w (100); xps and ups studies. *Surface science* **131**, 49–60 (1983).

[86] Ertl, G. Surface science and catalysis—studies on the mechanism of ammonia synthesis: the ph emmett award address. *Catalysis Reviews Science and Engineering* **21**, 201–223 (1980).

[87] de Castro, A. & Tabarés, F. Role of nitrogen inventory and ion enhanced nh recombination in the ammonia formation on tungsten walls. a dc glow discharge study. *Vacuum* **151**, 66–72 (2018).

[88] Pitts, R. *et al.* A full tungsten divertor for iter: Physics issues and design status. *Journal of Nuclear Materials* **438**, S48–S56 (2013).

[89] Tougaard, S. Accuracy of the non-destructive surface nanostructure quantification technique based on analysis of the xps or aes peak shape. *Surface and Interface Analysis: An International Journal devoted to the development and application of techniques for the analysis of surfaces, interfaces and thin films* **26**, 249–269 (1998).

[90] Ben Yaala, M. *et al.* Plasma-assisted catalytic formation of ammonia in n2-h2 plasma on tungsten surface. *Submitted to Physical Chemistry Chemical Physics (In peer review)* (2019).

[91] Zhang, X. *et al.* Thermal stability of tungsten sub-nitride thin film prepared by reactive magnetron sputtering. *Journal of Nuclear Materials* **485**, 1–7 (2017).

[92] Hill, A. K. & Torrente-Murciano, L. Low temperature h2 production from ammonia using ruthenium-based catalysts: Synergetic effect of promoter and support. *Applied Catalysis B: Environmental* **172**, 129–135 (2015).

[93] Hansgen, D. A., Vlachos, D. G. & Chen, J. G. Using first principles to predict bimetallic catalysts for the ammonia decomposition reaction. *Nature chemistry* **2**, 484 (2010).

[94] Bell, T. & Torrente-Murciano, L. H2 production via ammonia decomposition using non-noble metal catalysts: a review. *Topics in Catalysis* **59**, 1438–1457 (2016).

[95] Markelj, S., Založnik, A. & Čadež, I. Interaction of ammonia and hydrogen with tungsten at elevated temperature studied by gas flow through a capillary. *Journal of Vacuum Science & Technology A: Vacuum, Surfaces, and Films* **35**, 061602 (2017).

[96] Tamaru, K. A" new" general mechanism of ammonia synthesis and decomposition on transition metals. *Accounts of Chemical Research* **21**, 88–94 (1988).

[97] Mukherjee, S., Devaguptapu, S. V., Sviripa, A., Lund, C. R. & Wu, G. Low-temperature ammonia decomposition catalysts for hydrogen generation. *Applied Catalysis B: Environmental* **226**, 162–181 (2018).

[98] Marot, L., Pichon, L., Drouet, M. & Straboni, A. Improved nitrogen transport in fe–c alloys during nh3 plasma nitridation. *Materials Letters* **44**, 35–38 (2000).

[99] Marot, L., Le Bourhis, E. & Straboni, A. Improved nitridation efficiency and mechanical property of stainless steel surface after n2–h2 plasma nitridation at low temperature. *Materials letters* **56**, 76–79 (2002).

[100] Boisen, A., Dahl, S., Nørskov, J. K. & Christensen, C. H. Why the optimal ammonia synthesis catalyst is not the optimal ammonia decomposition catalyst. *Journal of Catalysis* **230**, 309–312 (2005).

[101] Hong, J., Prawer, S. & Murphy, A. B. Production of ammonia by heterogeneous catalysis in a packed-bed dielectric-barrier discharge: influence of argon addition and voltage. *IEEE Transactions on Plasma Science* **42**, 2338–2339 (2014).

[102] Nakajima, J. & Sekiguchi, H. Synthesis of ammonia using microwave discharge at atmospheric pressure. *Thin Solid Films* **516**, 4446–4451 (2008).

Bibliography

[103] Mansour, M., El-Sayed, N., Farag, O. & Elghazaly, M. Effect of he and ar addition on n2 glow discharge characteristics and plasma diagnostics. *Arab J. of Nuclear Sci. and Applications* **46**, 116–125 (2013).

[104] Pu, Y.-K. *et al.* Comparative characterization of high-density plasma reactors using emission spectroscopy from vuv to nir. *Pure and applied chemistry* **74**, 459–464 (2002).

[105] Sode, M., Schwarz-Selinger, T. & Jacob, W. Ion chemistry in h2-ar low temperature plasmas. *Journal of Applied Physics* **114**, 063302 (2013).

[106] Elsayed, N. & farag, o. The influence of the gas mixing ratio on some characteristics and reaction rate coefficients of ar/n2 and he/n2 dc plasma. *Arab Journal of Nuclear Sciences and Applications* **52**, 181–186 (2019).

[107] Inficon research crystals. `https://products.inficon.com/getattachment.axd/?attaName=9e8fae67-ba67-4743-b516-aafc332166e1`.

[108] Seo, Y., Lee, J. & Yu, I. Amplitude change of a quartz crystal microbalance. *Journal of the Korean Physical Society* **51**, 1948–1952 (2007).

[109] Borovsky, B., Mason, B. & Krim, J. Scanning tunneling microscope measurements of the amplitude of vibration of a quartz crystal oscillator. *Journal of Applied Physics* **88**, 4017–4021 (2000).

[110] Sauerbrey, G. Use of quartz crystal units for weighing thin films and microweighing. *Magzine for Physics* **155**, 206–222 (1959).

[111] Stockbridge, C. Effects of gas pressure on quartz crystal microbalances. *Vacuum Microbalance Techniques* **5**, 147–178 (1966).

[112] Kanazawa, K. K. & Gordon, J. G. The oscillation frequency of a quartz resonator in contact with liquid. *Analytica Chimica Acta* **175**, 99–105 (1985).

[113] Tsionsky, V., Daikhin, L., Urbakh, M. & Gileadi, E. Behavior of quartz crystal microbalance in nonadsorbed gases at high pressures. *Langmuir* **11**, 674–678 (1995).

[114] Wu, Y.-T. *et al.* Quartz crystal microbalance (QCM) in high-pressure carbon dioxide (CO$_2$): Experimental aspects of QCM theory and CO$_2$ adsorption. *Langmuir* **20**, 3665–3673 (2004).

[115] Kulchytskyy, I., Kocanda, M. G. & Xu, T. Direct mass determination of hydrogen uptake using a quartz crystal microbalance. *Applied Physics Letters* **91**, 113507 (2007).

[116] Anghel, A., Mustata, I., Porosnicu, C. & Lungu, C. Influence of the bias voltage on the formation of beryllium films by a thermionic vacuum arc method. *Journal of Nuclear Materials* **385**, 242–245 (2009).

[117] Daikhin, L. & Urbakh, M. Effect of surface film structure on the quartz crystal microbalance response in liquids. *Langmuir* **12**, 6354–6360 (1996).

[118] Urbakh, M. & Daikhin, L. Influence of the surface morphology on the quartz crystal microbalance response in a fluid. *Langmuir* **10**, 2836–2841 (1994).

[119] Urbakh, M. & Daikhin, L. Roughness effect on the frequency of a quartz-crystal resonator in contact with a liquid. *Physical Review B* **49**, 4866 (1994).

[120] Plazinski, W., Rudzinski, W. & Plazinska, A. Theoretical models of sorption kinetics including a surface reaction mechanism: A review. *Advances in Colloid and Interface Science* **152**, 2 – 13 (2009).

[121] Gundry, P. M. & Tompkins, F. C. Chemisorption of gases on metals. *Q. Rev. Chem. Soc.* **14**, 257–291 (1960).

[122] Surplice, N. & Brearley, W. The adsorption of carbon monoxide, ammonia, and wet air on gold. *Surface Science* **52**, 62–74 (1975).

[123] Coltrin, M. E. & Kay, B. D. Quasiclassical trajectory study of rotational energy transfer in the scattering of NH_3 from a flat, rigid gold surface. *The Journal of chemical physics* **89**, 551–561 (1988).

[124] Richton, R. & Farrow, L. Adsorption kinetics of ammonia on an inhomogeneous gold surface. *The Journal of Physical Chemistry* **85**, 3577–3581 (1981).

[125] Kay, B. D., Lykke, K. R., Creighton, J. R. & Ward, S. J. The influence of adsorbate–absorbate hydrogen bonding in molecular chemisorption: NH_3, HF, and H_2O on Au (111). *The Journal of chemical physics* **91**, 5120–5121 (1989).

[126] Bilić, A., Reimers, J. R., Hush, N. S. & Hafner, J. Adsorption of ammonia on the gold (111) surface. *The Journal of chemical physics* **116**, 8981–8987 (2002).

[127] Tsyganenko, A., Pozdnyakov, D. & Filimonov, V. Infrared study of surface species arising from ammonia adsorption on oxide surfaces. *Journal of Molecular Structure* **29**, 299–318 (1975).

[128] de Castro, A., Alegre, D. & Tabarés, F. Physisorption of ammonia on AISI 304L stainless steel at different surface temperature under high vacuum conditions. *Nuclear Materials and Energy* **9**, 1–5 (2016).

[129] Allouche, A. Nitrogen reactivity toward beryllium: surface reactions. *Journal of Physics: Condensed Matter* **25**, 225002 (2013).

[130] Jennison, D., Schultz, P. & Sears, M. Ab initio calculations of adsorbate hydrogen-bond strength: ammonia on Pt (111). *Surface science* **368**, 253–257 (1996).

[131] Grunze, M., Brundle, C. & Tomanek, D. Adsorption and decomposition of ammonia on a W(110) surface: photoemission fingerprinting and interpretation of the core level binding energies using the equivalent core approximation. *Surface Science* **119**, 133–149 (1982).

[132] Jacobi, K., Wang, Y., Fan, C. Y. & Dietrich, H. Adsorption and thermal dehydrogenation of ammonia on Ru (1121). *The Journal of Chemical Physics* **115**, 4306–4313 (2001).

[133] Parmeter, J., Wang, Y., Mullins, C. & Weinberg, W. Electron energy loss spectroscopy of ammonia on Ru (001). *The Journal of chemical physics* **88**, 5225–5236 (1988).

[134] Manandhar, K. *et al.* Structure and Reactivity of Molecularly Adsorbed Ammonia on the ZrB_2(0001) Surface. *The Journal of Physical Chemistry C* **118**, 29260–29269 (2014).

[135] Diawara, B., Joubert, L., Costa, D., Marcus, P. & Adamo, C. Ammonia on Ni (111) surface studied by first principles: Bonding, multilayers structure and comparison with experimental IR and XPS data. *Surface Science* **603**, 3025–3034 (2009).

[136] Wu, M. C., Truong, C. M. & Goodman, D. W. Interactions of ammonia with a nickel oxide (100) surface studied by high-resolution electron energy loss spectroscopy and temperature programmed desorption spectroscopy. *The Journal of Physical Chemistry* **97**, 4182–4186 (1993).

[137] Il'inchik, E. & Merenkov, I. X-ray photoelectron study of the effect of the composition of the initial gas phase on changes in the electronic structure of hexagonal boron nitride films obtained by PECVD from borazine. *Journal of Structural Chemistry* **57**, 670–678 (2016).

[138] Caretti, I. & Jiménez, I. Influence of carbon content and nitrogen vacancies on the bonding structure and mechanical performance of graphite-like BC $_x$n thin films. *Journal of Applied Physics* **112**, 063525 (2012).

[139] Lippitz, A. & Hübert, T. XPS investigations of chromium nitride thin films. *Surface and Coatings Technology* **200**, 250–253 (2005).

[140] Romand, M. & Roubin, M. Esca (Electron Spectroscopy for Chemical Analysis) Studies of Chromium and Vanadium Nitrides. *Analusis* **4**, 308–312 (1976).

[141] Haasch, R., Lee, T.-Y., Gall, D., Greene, J. & Petrov, I. Epitaxial CrN (001) Grown and Analyzed In situ by XPS and UPS. i. Analysis of As-deposited Layers. *Surface Science Spectra* **7**, 250–261 (2000).

[142] Nandi, D. K. *et al.* Atomic layer deposited tungsten nitride thin films as a new lithium-ion battery anode. *Physical Chemistry Chemical Physics* **17**, 17445–17453 (2015).

[143] Schmid, K. *et al.* Interaction of nitrogen plasmas with tungsten. *Nuclear Fusion* **50**, 025006 (2010).

[144] Eren, B. *et al.* Roughening and reflection performance of molybdenum coatings exposed to a high-flux deuterium plasma. *Nuclear fusion* **53**, 113013 (2013).

[145] Zhao, Y. *et al.* Preparation and characterization of tungsten oxynitride nanowires. *Journal of materials chemistry* **17**, 4436–4440 (2007).

[146] Dawson, P. & Hansen, R. S. Field-Emission Study of the Adsorption and Decomposition of Ammonia on Tungsten. *The Journal of Chemical Physics* **48**, 623–636 (1968).

[147] Masson, D., Merrill, R. & Houston, P. The sticking and dissociation of NH_3 on W (110): a three-state model. *Surface science* **330**, 239–254 (1995).

[148] Rodriguez, J. A., Truong, C. M. & Goodman, D. W. Synthesis of boron nitride ultra-thin films: The bonding and chemistry of ammonia and hydrazine on Ru (0001) and B/Ru (0001) surfaces. *Journal of Vacuum Science & Technology A: Vacuum, Surfaces, and Films* **10**, 955–959 (1992).

[149] Cheng, H., Reiser, D. B., Mathias, P. M., Baumert, K. & Dean Jr, S. W. Investigation of nitriding mechanism at transition metal surfaces: NH$_3$ Adsorption and Decomposition on Fe (100), Ni (100), and Cr (100). *The Journal of Physical Chemistry* **99**, 3715–3722 (1995).

[150] Ma, H., Berthier, Y. & Marcus, P. AES, XPS, and TDS study of the adsorption and desorption of NH$_3$ on ultra-thin chromium oxide films formed on chromium single crystal surfaces. *Applied surface science* **153**, 40–46 (1999).

[151] Alcala, M., Sanchez-Lopez, J., Real, C., Fernandez, A. & Matteazzi, P. Mechanosynthesis of carbon nitride compounds. *Diamond and related materials* **10**, 1995–2001 (2001).

[152] Gouin, X., Grange, P., Bois, L., L'Haridon, P. & Laurent, Y. Characterization of the nitridation process of boric acid. *Journal of alloys and compounds* **224**, 22–28 (1995).

[153] Mukhin, E. *et al.* First mirrors in ITER: material choice and deposition prevention/cleaning techniques. *Nuclear Fusion* **52**, 013017 (2011).

[154] Walsh, M. *et al.* Integration of diagnostics on ITER. In *Fusion Engineering (SOFE), 2015 IEEE 26th Symposium on*, 1–8 (IEEE, 2015).

[155] Ushakov, A. *et al.* UWAVS first mirror plasma cleaning technology using 30–60 MHz RF discharges. *Fusion Engineering and Design* **131**, 54–60 (2018).

[156] Yan, R. *et al.* Plasma cleaning of ITER edge Thomson scattering mock-up mirror in the EAST tokamak. *Nuclear Fusion* **58**, 026008 (2017).

[157] Dmitriev, A. *et al.* In situ plasma cleaning of ITER diagnostic mirrors in noble-gas RF discharge. *Physica Scripta* **2017**, 014072 (2017).

[158] Kobelev, A. *et al.* Collisional RF sheath in capacitive discharge in strong oblique magnetic field. *Physics of Plasmas* **26**, 013504 (2019).

[159] Moser, L. *et al.* Plasma cleaning of ITER first mirrors. *Physica Scripta* **2017** (2017).

[160] Bassan, M. *et al.* Thomson scattering diagnostic systems in ITER. *Journal of Instrumentation* **11**, C01052 (2016).

[161] De Bock, M. *et al.* ITER perspective on fusion reactor diagnostics–A spectroscopic view. *Journal of Instrumentation* **11**, P08010 (2016).

[162] Mertens, P. The Core-Plasma CXRS Diagnostic for ITER: An Introduction to the Current Design. *Journal of Fusion Energy* 1–19 (2018).

[163] Marot, L. *et al.* Can aluminium or magnesium be a surrogate for beryllium: A critical investigation of their chemistry. *Fusion engineering and design* **88**, 1718–1721 (2013).

[164] Moser, L. *et al.* Plasma cleaning of beryllium coated mirrors. *Physica Scripta* **2016**, 014069 (2016).

[165] Moser, L. *et al.* Investigation and plasma cleaning of first mirrors coated with relevant ITER contaminants: beryllium and tungsten. *Nuclear Fusion* (2017). URL http://iopscience.iop.org/10.1088/1741-4326/aa73e2.

[166] Björkas, C., Vörtler, K., Nordlund, K., Nishijima, D. & Doerner, R. Chemical sputtering of Be due to D bombardment. *New Journal of Physics* **11**, 123017 (2009).

[167] Grisham, L. *et al.* Recent improvements to the ITER neutral beam system design. *Fusion engineering and design* **87**, 1805–1815 (2012).

[168] Toigo, V. *et al.* Progress in the realization of the PRIMA neutral beam test facility. *Nuclear Fusion* **55**, 083025 (2015).

[169] Yamamura, Y. & Tawara, H. Energy dependence of ion-induced sputtering yields from monatomic solids at normal incidence. *Atomic data and nuclear data tables* **62**, 149–253 (1996).

[170] Eckstein, W. Calculated sputtering, reflection and range values (2002).

[171] Marot, L., De Temmerman, G., Oelhafen, P., Covarel, G. & Litnovsky, A. Rhodium coated mirrors deposited by magnetron sputtering for fusion applications. *Review of scientific instruments* **78**, 103507 (2007).

[172] Rubel, M. J. *et al.* Mirror test for International Thermonuclear Experimental Reactor at the JET tokamak: An overview of the program. *Review of scientific instruments* **77**, 063501 (2006).

[173] Ivanova, D. *et al.* An overview of the comprehensive First Mirror Test in JET with ITER-like wall. *Physica Scripta* **2014**, 014011 (2014).

[174] Baloniak, T., Reuter, R. & Von Keudell, A. Fundamental aspects of substrate biasing: ion velocity distributions and nonlinear effects. *Journal of Physics D: Applied Physics* **43**, 335201 (2010).

[175] Wisse, M., Eren, B., Marot, L., Steiner, R. & Meyer, E. Spectroscopic reflectometry of mirror surfaces during plasma exposure. *Review of scientific instruments* **83**, 013509 (2012).

[176] Ström, P., Petersson, P., Rubel, M. & Possnert, G. A combined segmented anode gas ionization chamber and time-of-flight detector for heavy ion elastic recoil detection analysis. *Review of Scientific Instruments* **87**, 103303 (2016).

[177] Burducea, I. *et al.* A new ion beam facility based on a 3 MV Tandetron™ at IFIN-HH, Romania. *Nuclear Instruments and Methods in Physics Research Section B: Beam Interactions with Materials and Atoms* **359**, 12–19 (2015).

[178] Stratagem version 2.6, samx, 4, rue galilée, 78280 guyancourt, france.

[179] Galbert, F. Measurement of carbon layer thickness with EPMA and the thin film analysis software STRATAGem. *Microscopy and Microanalysis* **13**, 96–97 (2007).

[180] Galbert, F. & Berger, D. Thickness and composition measurement of thin TEM samples with EPMA and the thin film analysis software STRATAGem. In *EMC 2008 14th European Microscopy Congress 1–5 September 2008, Aachen, Germany*, 545–546 (Springer, 2008).

[181] Ortel, E., Kraehnert, R., Galbert, F. & Hodoroaba, V.-D. Thin film porosity determined by X-rays at SEM. *Microscopy and Microanalysis* **21**, 1707–1708 (2015).

[182] Pouchou, J. & Pichoir, F. Electron probe X-ray microanalysis applied to thin surface films and stratified specimens. *Scanning Microscopy International(USA)* 167–190 (1992).

[183] Moser, L. *Plasma cleaning of diagnostic first mirrors for the nuclear fusion machine ITER.* Ph.D. thesis, University of Basel, doi: 10.5451/unibas-006748412 (2017).

[184] Abe, Y., Kato, K., Kawamura, M. & Sasaki, K. Rhodium and rhodium oxide thin films characterized by XPS. *Surface Science Spectra* **8**, 117–125 (2001).

[185] Marot, L., De Temmerman, G., Thommen, V., Mathys, D. & Oelhafen, P. Characterization of magnetron sputtered rhodium films for reflective coatings. *Surface and Coatings Technology* **202**, 2837–2843 (2008).

[186] Eren, B., Wisse, M., Marot, L., Steiner, R. & Meyer, E. Deuterium plasma exposure on rhodium: Reflectivity monitoring and evidence of subsurface deuteride formation. *Applied surface science* **273**, 94–100 (2013).

[187] Garcia-Carrasco, A. *et al.* Plasma impact on diagnostic mirrors in JET. *Nuclear Materials and Energy* **12**, 506–512 (2017).

[188] Choi, J.-G. & Thompson, L. XPS study of as-prepared and reduced molybdenum oxides. *Applied Surface Science* **93**, 143–149 (1996).

[189] Voitsenya, V., Bardamid, A. & Donné, A. Experimental simulation of the behaviour of diagnostic first mirrors fabricated of different metals for ITER conditions. *Open Physics Journal* **3** (2016).

[190] Alov, N. Determination of the states of oxidation of metals in thin oxide films by X-ray photoelectron spectroscopy. *Journal of Analytical Chemistry* **60**, 431–435 (2005).

[191] Roth, J. *et al.* Eurofer as wall material: reduced sputtering yields due to w surface enrichment. *J. Nucl. Mater.* **454**, 1–6 (2014).

[192] Aumeunier, M.-H. *et al.* Modeling of the iter-like wide-angle infrared thermography view of jet. *Review of Scientific Instruments* **83**, 10D522 (2012).

[193] Aumeunier, M. *et al.* Multi parametric sensitivity study applied to temperature measurement of metallic plasma facing components in fusion devices. In *2013 3rd International Conference on Advancements in Nuclear Instrumentation, Measurement Methods and their Applications (ANIMMA)*, 1–6 (IEEE, 2013).

[194] Loarer, T. Surface temperature measurement of plasma facing components in metallic environment. *Contributions to Plasma Physics* **51**, 201–206 (2011).

[195] Amiel, S. *et al.* Surface temperature measurement of plasma facing components with active pyrometry. In *Journal of Physics: Conference Series*, vol. 395, 012074 (IOP Publishing, 2012).

Bibliography

[196] Kočan, M. *et al.* First results on modeling of iter infrared images. *Physica Scripta* **2016**, 014047 (2016).

[197] Aumeunier, M.-H., Kočan, M., Reichle, R. & Gauthier, E. Impact of reflections on the divertor and first wall temperature measurements from the iter infrared imaging system. *Nuclear Materials and Energy* **12**, 1265–1269 (2017).

[198] Kajita, S. *et al.* Effect of wall light reflection in iter diagnostics. *Nuclear Fusion* **57**, 116061 (2017).

[199] Matsapey, N., Faucheu, J., Flury, M. & Delafosse, D. Design of a gonio-spectro-photometer for optical characterization of gonio-apparent materials. *Measurement Science and Technology* **24**, 065901 (2013).

[200] Zastrow, K.-D. *et al.* Modeling the effect of reflection from metallic walls on spectroscopic measurements. *Review of Scientific Instruments* **79**, 10F701 (2008).

[201] Schopfer, J., Dangel, S., Kneubühler, M. & Itten, K. The improved dual-view field goniometer system figos. *Sensors* **8**, 5120–5140 (2008).

[202] Phd dissertation, baran eren, effects of hydrogen plasma treatment on the electronic, optical, mechanical and chemical properties of mo, rh, au, hopg and graphene. `https://edoc.unibas.ch/29891/1/main_thesis.pdf`.

[203] Bennett, H. E., Silver, M. & Ashley, E. J. Infrared reflectance of aluminum evaporated in ultra-high vacuum. *JOSA* **53**, 1089–1095 (1963).

[204] Goossens, V. *et al.* Predicting reflections of thin coatings. *Surface and Coatings technology* **204**, 551–557 (2009).

[205] Palik, E. D. *Handbook of optical constants of solids*, vol. 3 (Academic press, 1998).

[206] Su, P., Eri, Q. & Wang, Q. optical roughness brdf model for reverse monte carlo simulation of real material thermal radiation transfer. *Applied optics* **53**, 2324–2330 (2014).

[207] Wen, C.-D. & Mudawar, I. Modeling the effects of surface roughness on the emissivity of aluminum alloys. *International journal of heat and mass transfer* **49**, 4279–4289 (2006).

List of Figures

List of Figures

127

List of Tables

Nomenclature

Symbols

BE, E_B	Binding energy
c	velocity
C_f	Spectralon correction factor
C_m	QMB mass sensitivity
C_P	QMB pressure sensitivity
C_r	QMB roughness factor
e	Elementary charge
E	Energy
E_a	Activation energy
E_{chem}	Chemisorption energy
E_{des}	Desorption energy
E_{diss}	Dissociation energy
E_f	Fermi level
E_i	Incident irradiance
E_{kin}	Kinetic energy
E_{phys}	Physisorption energy
E_T	Threshold Energy for the formation of vibrational excited atom
E_v	Vacuum level
f_0	Fundamental frequency
$h\nu$	Photon energy
I	Light intensity
L_r	Reflected radiance
L_z	Radiance loss parameter
m	Mass
n	Neutron
n_e	Electron density
P	Pressure
p	Proton
Q	Gain factor
q	Charge particle
r	Molecule distance from the surface
R	Ground state
R	Vibrational state
R_a	Average roughness
T	Temperature
T_e	Electron temperature
V_F	Floating potential
V_P	Plasma potential
Z	atomic number

Δf	Frequency shift
Δf_m	Frequency shift related to the mass loading
Δf_ν	Frequency shift related to the density/viscosity of the surrounding fluid
Δf_P	Frequency shift related to the pressure change
Δf_r	Frequency shift related to the roughness of the QMB surface
Δf_T	Frequency shift related to the temperature change
Δm	Mass change per area unit
η_f	Viscosity of the fluid
Φ	work function
λ	Wavelength
μ_q	Shear modulus of quartz
ϕ_i	Azimuth angle of the incident light
ϕ_r	Azimuth angle of the reflected light
ρ_q	Density of the quartz
ρ_f	Density of the fluid
θ_i	Zenith angle of the incident light
θ_r	Zenith angle of the reflected light

Elements and other materials

Al	Aluminum
Ar	Argon
Au	Gold
B	Boron
Be	Beryllium
C	Carbon
Cr	Chromium
Cu	Copper
Fe	Iron
D	Deuterium
H	Hydrogen
He	Helium
Li	Lithium
Mg	Magnesium
Mo	Molybdenum
N	Nitrogen
Ne	Neon
Ni	Nickel
O	Oxygen
PEEK	PolyEther Ether ketone
Rh	Rhodium
SS	Stainless steel

T	Tritium
W	Tungsten
Zr	Zirconium

Methods and devices

AFM	Atomic force microscopy
BULGO	Basel University Laboratory Gonioreflectometer
EDX	energy dispersive X-ray analysis
FIGOS	Field Goniometer System
GyM	Gyrotron Machine linear plasma device
HIERDA	Heavy Ion Elastic Recoil Detection Analysis
IBA	Ion beam analysis
QMB	Quartz Microbalance
RGA	Residual gas analyser
SEM	Scanning electron microscopy
TVA	Thermionic Vacuum Arc
XPS	X-ray photoelectron spectroscopy

Units

amu	Atomic mass unit
Amps	Ampere
$^\circ$ C	Degrees Celcius
eV	Electron volts
Hz	Hertz
J	Joule
K	Kelvin
g	Grams
h	Hours
m	Meters
min	Minutes
mol	Mole
rad	Radian
s	Seconds
V	Volts
W	Watts

Fusion reactors

AUG, ASDEX Upgrade	Axially Symmetric Divertor Experiment in Garching, Germany
EAST	Experimental Advanced Superconducting Tokamak
JET	Joint European Torus in Culham, England
JET-ILW	JET ITER-Like Wall
ITER	World's largest tokamak project in Cadarache, France
WEST	Tungsten (W) Environment in Steady-state Tokamak, Cadarache, France

Others

AC	Alternative Current
at.%	Atomic per cent concentration
BRDF	Bidirectional Reflectance Distribution Function
CF	Calibration Factor
CP	Cracking Pattern
DBDs	Dielectric Barrier Discharges
DC	Direct Current
DFT	Density Functional Theory
ELMs	Edge Localized Modes
E-R	Eley Rideal
FMs	First Mirrors
FWHM	Full Width at Half Maximum
H-bond	Hydrogen bond
INFLPR	National Institute for Laser, Plasma & Radiation Physics
IR	Infra-Red
IPC	In Plasma catalyst
IT	Integration time
L-H	Langmuir-Hinshelwood
LN	Liquid Nitrogen
LTPs	Low Temperature Plasmas
ML	Monolayers
NBI	Neutral Beam Injection
NIR	Near Infra Red
PFCs	Plasma Facing Components
PFU	Plasma Facing Unit
PPC	Post Plasma Catalyst

Nomenclature

Ra	Average Roughness
RF	Radio Frequency
RT	Room Temperature
SRIM	Stopping and Range of Ions in Matter
UHV	Ultra-high vacuum
UV	Ultra Violet
Vis	Visible

Acknowledgements

COMING to the end of my PhD journey, I would like to take the opportunity to thank all those people with whom I have had interaction in the last four years and their contribution in many ways in the final form of this work.

I would like first to express my sincere gratitude Prof. Dr. Ernst Meyer for giving me the opportunity to join his group and to work in a good motivating environment as well as for his continuous support and guidance.

I would like to convey my sincere thanks to my supervisor, Dr. Laurent Marot, without whom, my PhD would not have been possible. I am particularly indebted to Laurent for his guidance and support, for the skills and knowledge, for his patience is correcting my papers and thesis and for giving me the opportunity to work in collaboration and have fruitful discussions with experienced scientists in top leading institutions. I have been really lucky to have a supervisor who cared so much about my PhD, and who responded to my questions and queries so promptly.

I am also grateful to Roland Steiner for his invaluable contribution to my work. His extensive knowledge, scientific acumen, engineering skills and invaluable constructive criticism helped me a lot to carry out my PhD projects efficiently.

My sincere thanks also go to Dr. Lucas Moser for his insightful comments, for the stimulating long discussion about small details in the different projects and for his support to achieve a successful experimental campaign in INFLPR, Romania.

Part of this thesis is the result of a fruitful collaboration with CEA Cadarache. For that, I would like to thank the group of Dr. Michaël Houry, especially my office mates Jonathan and Charlie, for the good time I spent working with them. In particular, I am grateful to Dr. Marie Helene Aumeunier for her active support and guidance and for sharing her immense knowledge in optics.

I had also the chance to perform part of the experiments in IFLPR Beryllium facility in Romania. I would like to acknowledge Prof. Cristian Lungu and Dr. Corneliu Porosnicu for the friendly working environment and for giving me access to their research facilities.

I would also like to thank Dr. Martin Oberkofler from Max Plank Institute for

Acknowledgements

List of publications & communications

Peer-reviewed journal publications

1. **Ben Yaala, M.**, Saeedi, A., Scherrer, D-F., Moser, L., Steiner, R., Zutter, M., Oberkofler, M., De Temmerman, G., Marot, L. and Meyer E., **2019**. Plasma-assisted catalytic formation of ammonia in N_2-H_2 plasma on tungsten surface. ***Physical Chemistry Chemical Physics***, 21(30), p. 16623. `https://pubs.rsc.org/en/content/articlehtml/2019/cp/c9cp01139k`

2. **Ben Yaala, M.**, Moser, L., Steiner, R., Butoi, B., Dinca, P., Petersson, P., Marot, L. and Meyer, E.,**2019**. Deuterium as a cleaning gas for ITER first mirrors: experimental study on beryllium deposits from laboratory and JET-ILW. ***Nuclear Fusion***, 59(9), p.096027. `https://iopscience.iop.org/article/10.1088/1741-4326/ab2d31/meta`

3. **Ben Yaala, M.**, Scherrer, D-F., Saeedi, A., Moser, L., Steiner, R., De Temmerman, G., Oberkofler, M., Marot, L. and Meyer E., **2019**. Plasma-activated catalytic formation of ammonia from N_2-H_2: Influence of temperature and noble gases addition. ***Nuclear Fusion***, 60(1), p.016026. `https://iopscience.iop.org/article/10.1088/1741-4326/ab519c/meta`

4. **Ben Yaala, M.**, Marot, L., Steiner, R., Moser, L., De Temmerman, G., Porosnicu, C., Lungu, C.P., Oberkofler, M. and Meyer, E., **2018**. Quartz microbalance and in situ XPS study of the adsorption and decomposition of ammonia on gold, tungsten, boron, beryllium and stainless steel surfaces. ***Nuclear Fusion***, 58(10), p.106012. `https://iopscience.iop.org/article/10.1088/1741-4326/aad483`

5. **Ben Yaala, M.**, Aumeunier, M-H., Steiner, R., Schönenberger, M., Martin, C., Talatizi, C., Marot, L., Meyer, E. Bidirectional reflectance measurement of tungsten samples to assess reflection model in WEST tokamak. ***Review of Scientific Instruments***, Submitted.

6. Moser, L., Marot, L., Steiner, R., Reichle, R., Leipold, F., Vorpahl, C., Le Guern, F., Walach, U., Alberti, S., Furno, I., Yan, R., Peng, J., **Ben Yaala, M.** and Meyer, E., **2017**. Plasma cleaning of ITER first mirrors. ***Physica Scripta***, 2017(T170), p.014047. `https://iopscience.iop.org/article/10.1088/1402-4896/aa8f30/meta`

7. Brezinsek, S., [et al including **Ben Yaala, M.**], **2017**. Plasma–wall interaction studies within the EUROfusion consortium: progress on plasma-facing components development and qualification. ***Nuclear Fusion***, 57(11), p.116041. `https://iopscience.iop.org/article/10.1088/1741-4326/aa796e`

8. Aumeunier, M-H., Gerardin, J., Talatizi, C., Le Bohec, M., **Ben Yaala, M**., Marot, L., Loarer, T., Mitteau, R., Gaspar, J., Rigollet, F., Courtois, X. Houry, M., Herrmannd, A., Faitschd, M., the WEST team and ASDEX Upgrade team, **2021**. Infrared Thermography in Metallic Environments of WEST and ASDEX Upgrade. ***Nuclear materials and energy***, 26, p.100879.`https://doi.org/10.1016/j.nme.2020.100879`

Peer-reviewed conference proceedings

1. Voroshazi, E., **Ben Yaala, M.**, Uytterhoeven, G., Tait, J.G., Andriessen, R.H., Galagan, Y. and Cheyns, D., 2015, June. Light stability of ITO-free semi-transparent and opaque organic photovoltaic devices. In Photovoltaic Specialist Conference (PVSC), (pp. 1-4) `https://ieeexplore.ieee.org/document/7356181`

2. Saager, S., **Ben Yaala, M.**, Heinß, J-P., Temmler,D., Pfefferling, B. and Metzner, C., 2014, September, High-rate deposition of Si absorber layers by electron beam evaporation and first electron beam crystallization tests. In European Photovoltaic Solar Energy Conference and Exhibition, (p. 1900 - 1903) `https://www.eupvsec-proceedings.com/proceedings?paper=27837`

Presentations

1. Bidirectional Reflectance measurements and modelling of tungsten samples with different roughness, CEA, WEST Task Force Meeting , 28 March 2019, Cadarache, France

2. Influence of W surface roughness on the BRDF measurements, 35th ITPA Topical Group on Diagnostics, ITER, 8-12 October 2018, Cadarache, France

3. Wall Reflection Measurements, 31st ITPA Topical Group on Diagnostics, ITER, 7-11 November 2016, Cadarache, France

4. BRDF measurements for PFCs reflectance contribution modelling, 29th ITPA Topical Group on Diagnostics, ITER, 2-6 November 2015, Cadarache, France

Posters

1. **Ben Yaala, M.**, Steiner, R., Moser, L., Oberkofler, M., De Temmerman, G., Marot, L. and Meyer, E., Ammonia production from H_2/N_2 plasma on tungsten surface. International Conference on Plasma Surface Interaction in Controlled Fusion Devices (PSI), 17-22 June 2018, Princeton, NJ, USA

2. **Ben Yaala, M.**, Marot, L., Steiner, R., Moser, L., De Temmerman, G. Porosnicu, C., Lungu, C., Oberkofler ,M. and Meyer E., Quartz micro-balance and in situ XPS study of the adsorption and decomposition of ammonia on gold, tungsten, boron, beryllium and stainless steel surfaces. Nanotech Middle East international Conference and Exhibition, 4 - 6 December 2017, Dubai, United Arab Emirates

3. **Ben Yaala, M.**, Marot, L., Steiner, R., Moser, L., De Temmerman, G., Porosnicu, C., Lungu, C., Oberkofler, M. and Meyer E., Ammonia sticking on surfaces. International Conference on Plasma-Facing Materials and Components for Fusion Applications, 16 - 19 May 2017, Neuss/Düsseldorf, Germany

4. **Ben Yaala, M.**, Marot, L., Steiner, R., Oberkofler, M., De Temmerman, G. and Meyer E., Ammonia sticking on surfaces. International Conference on Plasma Surface Interaction in Controlled Fusion Devices (PSI), 30 May- 3 June 2016, Rome, Italy.

5. Aumeunier, M.H, Gerardin, J., Talatizi, C., **Ben Yaala, M.**, Marot, L. Firdaouss, M. and the WEST Team International Conference on Advancements in Nuclear Instrumentation Measurement Methods and their Applications (ANIMMA), 19-23 June 2017, Liege, Belgium

6. Saager, S., **Ben Yaala, M.**, Heinß, J-P., Metzner, C. , Pfefferling, B. and Temmler, D., September, High-rate deposition of Si absorber layers by electron beam evaporation and first electron beam crystallization tests. European Photovoltaic Solar Energy Conference and Exhibition, 22 - 26 September 2014, Amsterdam, The Netherlands

7. Trompoukis, C., El Daif, O., Verdonck, P., Niesen, B., **Ben Yaala, M.**, Depauw, V., Gordon, I. and Poortmans, J. Crystal orientation dependent anisotropic dry silicon etching. Plasma Etch and Strip Processes in Microtechnology (PESM), 14 - 15 March 2013, Leuven, Belgium